ADVANCED MOBILITY MODELS FOR DESIGN AND SIMULATION OF DEEP SUBMICROMETER MOSFETS

A DISSERTATION

SUBMITTED TO THE DEPARTMENT OF ELECTRICAL ENGINEERING

AND THE COMMITTEE ON GRADUATE STUDIES

OF STANFORD UNIVERSITY

IN PARTIAL FULFILLMENT OF THE REQUIREMENTS

FOR THE DEGREE OF

DOCTOR OF PHILOSOPHY

By

Syed Aon Mujtaba

December 1995

© Copyright by Syed Aon Mujtaba 1995

All Rights Reserved

I certify that I have read this dissertation and that in my opinion it is fully adequate, in scope and quality, as a dissertation for the degree of the Doctor of Philosophy.

Robert W. Dutton (Principal Advisor)

I certify that I have read this dissertation and that in my opinion it is fully adequate, in scope and quality, as a dissertation for the degree of the Doctor of Philosophy.

James D. Plummer (Associate Advisor)

I certify that I have read this dissertation and that in my opinion it is fully adequate, in scope and quality, as a dissertation for the degree of the Doctor of Philosophy.

Teresa H.-Y. Meng

Approved for the University Committee on Graduate Studies:

Abstract

Carrier mobility is one of the most important parameters affecting the I-V characteristics of MOSFETs. Hence, accurate mobility models that account for all the important scattering mechanisms are an essential requirement for predictive MOS device simulation. This dissertation focuses on issues related to mobility modeling in MOSFETs as they scale to deep submicron dimensions. A new physically-based mobility model for two dimensional (2D) device simulation is presented that accurately models MOSFETs for all channel lengths down to 0.25μm. Enhanced physical features of the new model include terms for 2D Coulombic scattering and 2D accumulation-layer mobility.

As MOSFETs scale to shorter channel lengths, channel doping levels increase in order to suppress undesirable short-channel effects such as punchthrough and drain-induced barrier lowering (DIBL). One direct consequence of increased doping is enhanced impurity scattering, the importance of which in scaled MOSFETs is established by demonstrating its impact on critical design parameters such as threshold voltage and off-state leakage current. An accurate model for impurity scattering has been developed that, for the first time, properly accounts for 2D confinement and quantum mechanical effects in the inversion layer. A systematic methodology for extracting Coulombic mobility from I-V data is also presented. Based on this scheme, it is shown that in regimes where three dimensional (3D) models grossly over-predict mobility, the new 2D model demonstrates its broad applicability by accurately reproducing experimental results over a wide range of channel dopings, substrate biases, and electron concentrations.

Traditionally, channel resistance has been the dominant factor limiting current transport in MOSFETs. However, in deep submicron MOSFETs with lightly-doped drain (LDD) structures, channel resistance has become comparable to the parasitic series resistance, a major component of which comes from the accumulation layer in the LDD region. A unified mobility model is presented that is applicable in both inversion and accumulation layers. A systematic methodology is presented for the calibration and

validation of the new model with experimental data. Broad applicability of the new model is established with excellent agreement over a wide range of operating conditions (subthreshold, linear, and saturation) for gate lengths ranging from 20.0μm down to 0.25μm.

Acknowledgments

A great number of wonderful people have made my Stanford career a very rewarding and memorable experience.

First and foremost, I would like to express my sincerest gratitude to my advisor and mentor, Professor Robert W. Dutton for his guidance and support throughout my years at Stanford. In ways more than one, he has made me realize my fullest potential, and encouraged me to attain the highest level of professionalism. I would especially like to thank him for giving me the freedom to pursue my research interests.

I would like to thank Professors James D. Plummer and Teresa H.-Y. Meng for their expeditious reading of my thesis and for serving on my oral examination committee. I would also like to thank Professor Bruce A. Wooley for serving on my oral examinations committee.

I have greatly benefited from the interaction with people in the industry. I am grateful to Dr. Don Scharfetter of Intel Corporation for mentoring me in my early years of graduate study. I would like to thank Dr. Shin-ichi Takagi and Mr. Junji Koga of Toshiba Corporation for their collaboration on the work on Coulombic scattering. I would like to thank Dr. Yuan Taur of IBM Research for his fruitful and insightful discussions on mobility modeling. I would like to thank Dr. John Faricelli of DEC for implementing my mobility model in MINIMOS.

The financial support of Semiconductor Research Corporation is gratefully acknowledged.

My most rewarding experience was the summer I spent at AT&T Bell Laboratories in Murray Hill, NJ. I would especially like to thank Drs. Ran Yan, Mark Pinto and Don Monroe of AT&T Bell Labs for giving me the opportunity to work with them on a variety of interesting and stimulating topics. I would like to thank Dr. Mark Pinto for implementing my mobility model in PADRE. My work on the characterization of AT&T's exploratory 0.25µm CMOS technology would not have been possible without the use of

PADRE and PROPHET, Bell Lab's in-house device and process simulators. Hence, I would like to thank the respective authors Dr. Mark Pinto and Dr. Conor Rafferty. I would like to thank Mr. David M. Boulin and Mr. Stephen V. Moccio of Bell Labs for their help in obtaining the experimental data for AT&T's 0.25μm process. I would like to thank Dr. Kathy Krisch for providing the C-V data. I would like to thank the following people of Bell Labs for their support and encouragement during my stay there: Dr. Syed Ali Eshraghi, Dr. Len C. Feldman, Dr. Abbas Ourmazd, Dr. Steve J. Hillenius, Dr. Lalita Manchanda, and Dr. Jeff Bude. I would especially like to thank Conor for introducing me to the wonderful sport of rock climbing while I was at Bell Labs. I would like to thank my officemates in Room 1E-306: Dr. Yih-Guei Wey, Dr. Kathy Krisch, and Dr. Masato Kawata. I acknowledge the help of Tracy Craddock and Cindy Stiles-Canter in taking care of administrative issues while I was at Bell Labs.

I have greatly benefited from the interaction with our devices group. I would like to thank Dr. Datong Chen and Greg Anderson for their help in familiarizing me with PISCES code. I would like to thank Dr. Ke-Chih Wu, Dr. Edwin Kan, Dr. Chiang-Sheng Yao, Mr. Richard Williams, and Dr. Zhiping Yu for stimulating and enlightening discussions on various issues relating to device simulation and modeling. Special thanks go to Edwin for his advice and encouragement on matters relating to academic and non-academic issues.

It would like to thanks all members of Dutton's TCADre for the fun time we've had together both on and off the softball field. I would especially like to thank Goodwin Chin, Robert Huang, Dan Yergeau, Narayana Aluru, and Francis Rotella.

Life in Applied Electronics Labs would have been very boring had it not been for the lively afternoon chats with Fely (actually Felicisima) and Maria. Many thanks go to Fely Barrera, Maria Perea, and Lynn Domagas for all their help with administrative issues.

I would like to thank the members of EECNS (previously EECF) staff, especially Chris Quinn, for providing an exceptional computing environment.

The time I have spent at Stanford has been even more enjoyable due to the all the friendships that I have made. In particular, I would like to thank Zartash Afzal Uzmi, Ahrar Naqvi, Bilal Ahmad, Jalil Kamali, Mehrdad Heshami, and Steve Jurichich.

Finally, special thanks go to my parents, grandparents, my brother, and my sisters for their endless support, love, and understanding throughout my educational career in the United States. I thank my parents for the sacrifices they have made over the years to provide us with opportunities to further our education. This thesis is dedicated to them.

To my parents

Table of Contents

List of Tables

List of Figures

Chapter 1

Introduction

1.1 Motivation

As a result of MOS technology scaling over the last three decades, the complexity of integrated circuits has increased tremendously from small-scale integration of a few transistors on a silicon substrate to the ultra-large-scale integration (ULSI) of tens of millions of transistors in today's chips. The complexity associated with a ULSI circuit has mandated the use of sophisticated computer-aided design (CAD) tools at all levels in the design hierarchy — process, device, circuit, and system design respectively. It has been recognized in recent years that the design of "integrated systems" (i.e. ULSI chips) would entail a concurrent optimization of circuit architecture and device technology, which is going to present new challenges for the CAD development community.

In previous chip generations, the circuit architecture was optimized independently of technology. As a result, CAD tools were broadly divided into two categories: electronic-design-automation (EDA) tools that included circuit and logic simulators, layout editors, and logic synthesis tools primarily served the needs of the circuit and system design community, whereas technology-CAD (TCAD) tools that included process and device simulators were largely used by technologists. Regarding the use of tools, an interesting distinction exists between the two communities. The circuit and system designers rely heavily on the EDA tools for the design work since a system typically involves a very large number of transistors. On the other hand, the use of TCAD tools by the technologists has been limited, primarily because of its lack of predictivity, which compels them to perform costly and time-consuming experiments to evaluate various technology options. For the most part, TCAD tools serve the purpose of providing insight into complex process and device physics phenomena that is not possible through experimentation alone.

However, the scenario changes in the design of integrated systems. Since, a simultaneous optimization of circuit and technology is desired, coupled device and circuit simulations would need to be performed, thus making the device simulators an integral part of the optimization and design loop. Hence, it has become important more than ever that the TCAD tools be as predictive as possible, since circuits and systems would have to be designed based on the data supplied by process and device simulators.

Predicitivity of TCAD tools hinges on the accuracy of models involved. The challenge facing TCAD tool developers is the formulation and efficient numerical implementation of physically-based models that exhibit a high degree of predictivity. To this end, this thesis attempts to improve the accuracy of MOSFET simulations by considering the modeling of one of the most important parameters affecting its I-V characteristics — mobility of electrons in MOS inversion and accumulation layers.

This thesis focuses on issues related to mobility modeling in MOSFETs as they scale to deep submicron dimensions. The aim is to extend the applicability of existing mobility models by incorporating new physical effects that arise due to the scaling of MOS devices. In this regard, two particular issues — Coulombic scattering and LDD resistance — have been identified that require further modeling work, and are briefly discussed below.

Scaling of MOSFETs to deep submicron dimensions mandates an increase in channel doping levels to suppress undesirable short-channel effects. One direct consequence of increased doping is enhanced impurity scattering, fundamental treatment of which is currently lacking in MOS inversion layers. The first half of the thesis is devoted to a thorough examination of 2D Coulombic scattering and how it needs to be modeled in the context of moment-based device simulators.

Traditionally, channel resistance has been the dominant factor limiting current transport in MOSFETs. As a consequence, mobility models existing in literature only addressed scattering in MOS inversion layers. However, in deep submicron MOSFETs with LDD structures, parasitic series resistance has become comparable to channel resistance, because of which it has become imperative to accurately model the extrinsic region of the device. Thus, the mobility model developed in the first half of the thesis for inversion layer electrons is extended to accurately model the accumulation layer occurring in the extrinsic (parasitic) region of LDD MOSFETs.

1.2 Scope and Organization

Mobility models fall into one three broad categories: physically-based, semi-empirical, and empirical. Physically-based models are those that are obtained from a first-principles calculation, i.e. both the coefficients and the power dependencies appearing in the model are obtained from a fundamental calculation. In practice, physically-based models rarely agree with experimental data since considerable simplifying assumptions are made in order to arrive at a closed form solution. Therefore, to reconcile the model with experimental data, the coefficients appearing in the physically-based model are allowed to vary from their original values. In this process the power-law dependencies resulting from the first-principles calculation are preserved, and the resulting model is termed as semi-empirical.

At the other end of the spectrum are empirically-based models in which the power-law dependencies are also allowed to vary. Empirical models have less physical content compared to the other two models, and also exhibit a narrower range of validity. Empirical models are usually resorted to when the dependencies predicted by the first-principles calculation do not allow a good fit between the experimental data and the corresponding semi-empirical model.

The organization of this thesis is based on the following systematic methodology for mobility modeling. The first step involves consideration of first principles calculation for mobility. Then the coefficients appearing in the physically-based model are allowed to vary in order to get a good fit between the model and experimental data. If this step is successful, then the calibration procedure is complete, and the model is ready for implementation in a device simulator. Otherwise, the power-law dependencies are also allowed to vary until a good fit is obtained. In this case, the empirical model is then implemented in the device simulator.

The objective of this thesis is to develop a semi-empirical model obtained from a first-principles calculation. Since a first principles calculation is lacking for 2D Coulombic scattering, it is discussed first. Chapter 2 provides the background material on the calculation of mobility starting from the Boltzmann transport equation (BTE). The machinery developed in Chapter 2 is then employed in Chapter 3 to calculate the two-dimensional Coulombic mobility in MOS inversion layers due to scattering with channel impurities. Separate calculations are performed for screened and unscreened Coulombic scattering. A systematic extraction technique is also proposed for the extraction of unscreened Coulombic mobility from experimental data, which in the case of screened Coulombic mobility is taken from the literature. On comparison with experimental data, it is shown that the new 2D model exhibits better agreement than existing models for 3D Coulombic scattering.

Chapter 4 is concerned with the semi-empirical modeling of the inversion layer. Extraction of semi-empirical models for phonon and surface roughness scattering from first principles calculations is outlined. Based on the first principles model for Coulombic scattering presented in Chapter 3, an empirical model for 2D Coulombic scattering is extracted. The resulting model containing terms for phonon, surface roughness, and Coulombic scattering is shown to accurately model experimental data over a wide range of technology and bias conditions expressed in the form of a *generalized mobility curve*.

Finally, in Chapter 5, the importance of modeling mobility in the accumulation layer is presented in the context of trying to accurately simulate deep submicron LDD MOSFETs. To this end, the semi-empirical model for inversion-layer electrons is extended to model the accumulation layer, and a systematic technique is presented for the validation and calibration of the new model. A striking feature of the new model is that it exhibits excellent agreement over a wide range of bias conditions in MOSFETs whose channel length ranges from 20μm to 0.25μm. Very high confidence is placed in the predictive nature of the new model since the *same* parameter set matches experimental data over such a broad range.

Chapter 6 summarizes the conclusions of this research and offers suggestions for future work.

Chapter 2

The Boltzmann Transport Equation

2.1 Introduction

A “first principles” calculation of macroscopic transport parameters such as mobility starts with a description of the state of the electron gas in microscopic terms, and then proceeds through a set of simplifying assumptions to arrive at the macroscopic parameter that describes the state of the gas as a whole. Quantum-mechanically, the microscopic state of the electron gas is described in terms of a many-body wavefunction, whereas classically, it is described by specifying the position and momentum of each particle. To characterize the operation of a MOSFET, we are not so much interested in the behavior of each and every electron, rather we are interested in their collective motion. Thus, the objective of performing the first-principles calculation is to *filter* out the essential piece of information from the detailed microscopic description of the electron gas.

If we consider the inversion layer to be a classical ensemble, then its microscopic state can be deterministically described by specifying the position and momentum of each electron. Due to our lack of knowledge concerning the initial conditions, we have to resort to a probabilistic description of the electron gas, which involves an N-particle distribution function that gives the joint probability of finding the N particles at their respective locations $\boldsymbol{r}$ with their respective momenta $\boldsymbol{p}$. This description is still very detailed, and if we assume the interactions among the electrons to be weak, and the time scales under consideration to be much larger than the interaction time between electrons, then the

N-particle distribution function can be reduced to a single particle distribution function. Thus, we postulate that under these simplifying assumptions, the single particle distribution function $f(\boldsymbol{r},\boldsymbol{p},t)$ describes the collective state of the electron gas. The evolution of $f(\boldsymbol{r},\boldsymbol{p},t)$ with time is governed by the Boltzmann transport equation (BTE) which forms the cornerstone of semiclassical electron dynamics.

In this chapter, we present a methodology for calculating mobility μ from the Boltzmann transport equation. The BTE is a complex integro-differential equation that is based on both quantum-mechanical and classical laws of dynamics. As such, the BTE in its original form does not yield a closed form solution for mobility, and simplifying assumptions are necessary to make the solution tractable. A detailed discussion of the assumptions made is presented in this chapter, which is organized into three main sections.

The first part, Section 2.2, deals with the derivation and simplification of the BTE. Derivation of the classical part is discussed earlier on in Section 2.2, while Section 2.2.1 is devoted to setting up the collision integral based on quantum mechanical principles. Section 2.2.2 presents a very important simplification to the collision integral, known as the relaxation time approximation (RTA). RTA permits us to calculate a closed form expression for mobility. Because of its significance, it is important to know the conditions under which the RTA is applicable. This forms the subject of discussion in Section 2.2.3. Thus, by the end of Section 2.2, we have a simplified form of the BTE that permits us to arrive at a closed form solution for mobility.

In Section 2.3, we discuss the approximations and outline the method for calculating mobility from the BTE using the RTA. This section concludes with an expression for mobility that has the relaxation time as a parameter.

Finally Section 2.4 discusses the quantum mechanical calculation of the relaxation time from the scattering potential. This calculation is based on the Fermi's golden rule that is derived from first-order time-dependent perturbation theory.

Thus the methodology that is presented in this chapter allows one to calculate mobility from a knowledge of the scattering potential. Calculation of the scattering potential forms the subject of the next chapter in which we first calculate the scattering potential for a screened two-dimensional Coulombic center, and then employ the machinery developed in this chapter to calculate the Coulombic mobility from the scattering potential.

2.2 Boltzmann Transport Equation

The classical theory of transport processes is based on the Boltzmann transport equation, which specifies the temporal evolution of the single-particle distribution function $f(\boldsymbol{r},\boldsymbol{p},t)$ in the six-dimensional phase space of Cartesian coordinates $\boldsymbol{r}$ and momentum $\boldsymbol{p}$, and it is defined by the relation

$$f(r, p)\, drdp \;=\; \text{probability of finding a particle in } drdp \tag{2.1}$$

Since trajectories in phase space do not intersect, Liouville's theorem states that the probability density of points in phase space remains constant in time, provided there is no scattering. Thus, in the 6 dimensional phase space [83]:

$$\frac{df(r, p, t)}{dt} \;=\; 0 \tag{2.2}$$

In the presence of scattering, the total rate of change of $f(\boldsymbol{r},\boldsymbol{p},t)$ with time equals the rate of scattering. Equation (2.2) thus transforms into:

$$\frac{df(r, p, t)}{dt} \;=\; \left(\frac{\partial f}{\partial t}\right)_{coll} \tag{2.3}$$

Expanding the total derivative in equation (2.3) yields:

$$\frac{\partial f}{\partial t} + \dot{r} \cdot \nabla_r f + \dot{p} \cdot \nabla_p f \;=\; \left(\frac{\partial f}{\partial t}\right)_{coll} \tag{2.4}$$

Equation (2.4) is the celebrated Boltzmann's transport equation (BTE) [16], which finds applications in diverse areas such as neutron transport in reactors, propagation of light through stellar matter, plasma dynamics, rarified gas dynamics, and electron transport in metals and semiconductors [17]. The rate of change of momentum $\dot{p}$ is equal to the applied force $\boldsymbol{F}$, and in the absence of a magnetic field, it is simply given by Lorentz's law:

$$\dot{\boldsymbol{p}} \;=\; \boldsymbol{F} \;=\; q\boldsymbol{E}(\boldsymbol{r}, t) \tag{2.5}$$

The rate of change of distance with time $\dot{r}$ is equal to the group velocity of Bloch[1] electrons [14]. Thus, the BTE for the Bloch electrons can be written as:

$$\frac{\partial f}{\partial t} + v_g \cdot \nabla_r f + qE \cdot \nabla_p f = \left(\frac{\partial f}{\partial t}\right)_{coll} \tag{2.6}$$

While the left hand side of equation (2.6) is a classical description of electron motion, the collision term on the right side requires a quantum treatment, which we discuss next.

2.2.1 Treatment of the Scattering Term

Electrons in solids are commonly represented by wave packets, and according to Heisenberg's uncertainty principle, they have a certain amount of spread in both real and momentum space. Typically, the extent of spread in real space is of the order of a few lattice constants. Usually, the externally applied potentials vary over hundreds of lattice constants, and to a very good approximation these potentials can be considered as constant over the dimensions of a wave packet. In such a scenario, the interaction between the electron and the external potential can be treated according to the classical laws of dynamics. On the other hand, if the variation in potential is of the order of the spread of a wavepacket, then this interaction needs to be treated quantum mechanically via the single-electron Schrodinger's equation.

Clearly, the periodic potential due to the atomic cores, i.e. the nuclei, varies on the order of a lattice constant, and hence this interaction needs to be treated quantum mechanically. When Schrodinger's equation is solved with this periodic potential, one finds that the electrons can be treated as "free" particles travelling with an effective mass that is different from the free electron[2] mass. The effective mass approximation fails if the externally applied field varies very rapidly, since that field can no longer be treated in the classical framework, and instead needs to be included in Schrodinger's equation. Thus, for the left hand side in equation (2.6) to be valid, the externally applied electric fields have to vary slowly compared to the dimensions of a wavepacket, as illustrated in Figure 2.1 [14].

---

1. Electrons moving in a periodic potential and satisfying the single-electron Schrodinger's equation are known as Bloch electrons [14].
2. A free electron, by definition, is one that moves in a zero potential field.

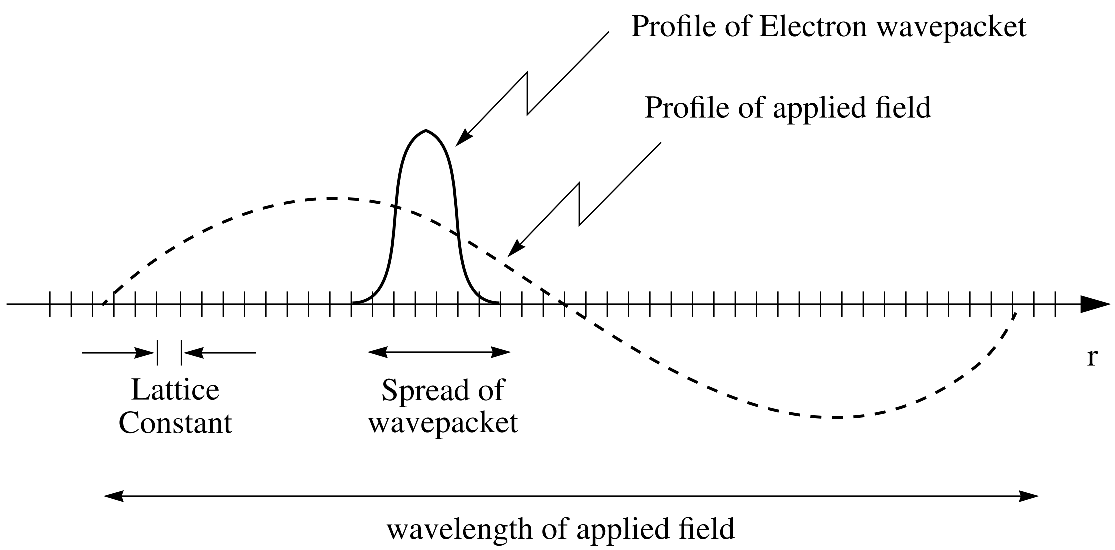

Figure 2.1 Schematic view of the dimensions involved in semiclassical transport [14].

However, when electrons scatter off an imperfection in a semiconductor, the spatial extent of the interaction potential is of the same order of magnitude as the dimensions of a wavepacket. *That is why all collision events need to be considered quantum mechanically.* While the "free" flight of electrons between two collision events is treated classically, the collision event itself is treated quantum mechanically.

In an effort to model the collision term, we examine in greater detail its role in the BTE. The left hand side of equation (2.6) governs the evolution of the distribution function $f(\boldsymbol{r},\boldsymbol{p},t)$ with time at a point $(\boldsymbol{r},\boldsymbol{p})$ in phase space due to externally applied forces, whereas its right hand side accounts for the effect of random scattering events on $f(\boldsymbol{r},\boldsymbol{p},t)$. The various contributions are seen more clearly if equation (2.6) is rewritten as follows:

$$\frac{\partial f}{\partial t} = -(v_g \cdot \nabla_r f) - (qE \cdot \nabla_p f) + \left(\frac{\partial f}{\partial t}\right)_{coll} \tag{2.7}$$

Then, the *local* rate of change of $f(\boldsymbol{r},\boldsymbol{p},t)$ with time at a point $(\boldsymbol{r},\boldsymbol{p})$ in phase space is given by the sum of the three terms: the first term represents the effect of diffusion due to spatial gradients in $f(\boldsymbol{r},\boldsymbol{p},t)$; the second term represents the effect of drift due to the externally applied field E, and the last term represents the effect of scattering events on $f(\boldsymbol{r},\boldsymbol{p},t)$. These various processes are depicted graphically in Figure 2.2.

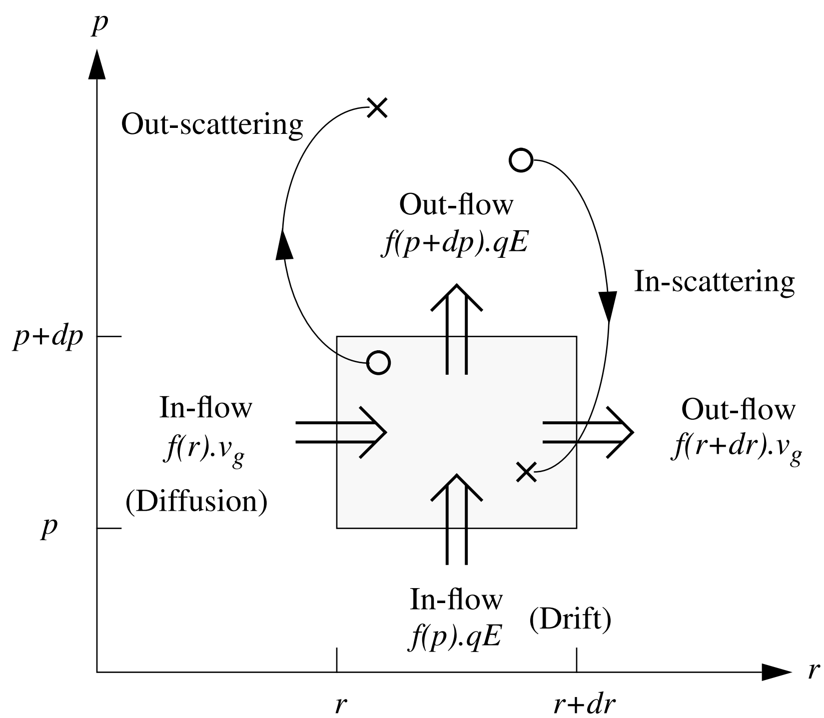

Figure 2.2 A cell in two-dimensional phase space. The three processes, namely drift, diffusion, and scattering, that affect the evolution of $f(\mathbf{r},\mathbf{p},t)$ with time in phase space are shown [15].

If we consider a small volume in phase space centered around the point $(\mathbf{r},\mathbf{p})$ (see Figure 2.2), then some particles would be leaving this volume due to *out-scattering*, while others would be entering it due to *in-scattering*. It should be noted that a scattering event *abruptly* changes the momentum of the particle without changing its position. The net effect of scattering on the number of particles in the volume element is simply the difference between the number of in-scattered and out-scattered particles:

$$\begin{aligned}\left(\frac{\partial f}{\partial t}\right)_{coll} &= (\text{In scattering rate}) - (\text{Out scattering rate}) \\ &= \left(\frac{\partial f}{\partial t}\right)^{in}_{coll} - \left(\frac{\partial f}{\partial t}\right)^{out}_{coll}\end{aligned} \tag{2.8}$$

Since the details of the scattering event need to be treated quantum mechanically, the electron is specified in terms of its Bloch wavefunction which is characterized by quasi-continuous momentum eigenvalues $\boldsymbol{p}$, or equivalently the wavevector $\boldsymbol{k}$ in momentum space, where $k = p/\hbar$. In addition to the $\boldsymbol{k}$ vector, the Bloch wavefunction is also characterized by a band index; however, this parameter would be ignored since it will be assumed that scattering events are strictly intraband. Thus, Bloch wavefunctions take on the following form [14]:

$$\psi_k(r) = u(r)\, e^{i(k \cdot r)} \tag{2.9}$$

where $u(r)$ is a periodic function such that $u(r+R)=u(r)$, where R is the periodicity of the lattice. An electron incident on a scattering center with wavevector k_i would emerge with wavevector k_f , and if k_f is different from k_i , the electron is said to have been *scattered*, while $k_f = k_i$ implies that the electron emerges unscattered. Scattering centers typically result from perturbations in the background electrostatic potential, and are characterized by a scattering potential $V_s(r,t)$. Scattering potential may be well localized in space, as in Coulombic scattering, or it may extend throughout the crystal, as in phonon scattering. A scattering event by a localized scattering potential is illustrated graphically in Figure 2.3.

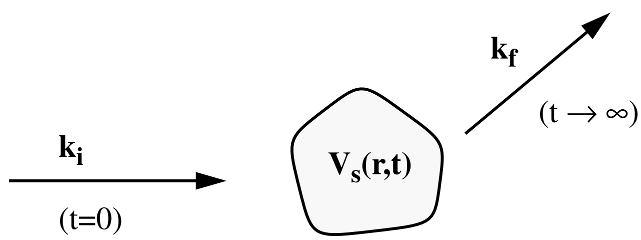

Figure 2.3 Scattering of an electron from initial wavevector $\mathbf{k_i}$ to final wavevector $\mathbf{k_f}$ by scattering potential $V_s(r,t)$.

Strictly speaking, we need to represent electrons by wavepackets instead of by Eigen-wavefunctions as in equation (2.9), where the wavepackets are typically constructed by combining Bloch wavefunctions whose $\boldsymbol{k}$ values span a certain range. For instance, a wavepacket can be represented as:

$$\Psi(r,t) = \int_{-\infty}^{\infty} c(k,k_o)\,\psi_k(r)\,e^{-\frac{i}{\hbar}\varepsilon(k)t}\,dk \tag{2.10}$$

where $c(k,k_o)$ is a function centered around k_o, and goes to zero if k is far from k_o. A candidate function for instance could be a Gaussian distribution centered around k_o.

The property of the wavepacket in equation (2.10) is that it is localized in space at the expense of a spread in momentum space (i.e. this wavepacket does not have a well-defined momentum). On the other hand, the Eigen-wavefunction in equation (2.9) exhibits a definite momentum but is not localized in space, and thus not really representative of an electron travelling in a solid. Nevertheless, we shall work with Eigenfunctions as in equation (2.9) since it is too cumbersome to work with wavepackets.

In order to find the rate at which electrons scatter into or scatter out of an element in phase space, we first need to know the probability per unit time, also known as the transition rate $S(k,k')$, with which an electron in state k_i would scatter to a state k_f in unit time. The probability that a scattering event does take place *also* depends upon the number of electron present in the initial state and the availability of the final states. Pauli's exclusion principle for fermions (which includes electrons) prohibits more than two of them from occupying the same eigenstate. Thus, an arbitrary number of electrons can *not* occupy a given state even if one exists. Hence, the probability of scattering per unit time from k to k', also known as the scattering rate, is given by:

$$P(k \rightarrow k') = S(k,k')f(k)\,[1 - f(k')] \tag{2.11}$$

The probability per unit time that an electron initially in state k would scatter *out* to any possible k state is known as the total scattering rate, and is obtained from equation (2.11) by summing over all the possible final k' vectors:

$$P(k) = \sum_{k'} S(k,k')f(k)\,[1 - f(k')] \tag{2.12}$$

The summation over k space can be converted to integration in k space by introducing the density of states in k space $D(k)=V/(2\pi)^3$, where the number of k states in dk is $D(k)dk$, and V is the volume of the crystal. Assuming that scattering does not flip spin, we get:

$$P_{out}(k) = \frac{V}{(2\pi)^3}\int S(k, k')f(k)\,[1-f(k')]\,dk' \tag{2.13}$$

$P_{out}(k)$ thus corresponds to the probability of scattering *out* of state k in unit time, i.e. $P_{out}(k) = \left(\frac{\partial f}{\partial f}\right)^{out}_{coll}$. Conversely, the scattering rate from k' to k is given by:

$$P(k' \rightarrow k) = S(k', k)f(k')\,[1-f(k)] \tag{2.14}$$

and the total scattering rate into state k is given by:

$$P_{in}(k) = \frac{V}{(2\pi)^3}\int S(k', k)f(k')\,[1-f(k)]\,dk' \tag{2.15}$$

$P_{in}(k)$ thus corresponds to the probability of scattering into state k in unit time, i.e. $P_{in}(k) = \left(\frac{\partial f}{\partial f}\right)^{in}_{coll}$. Therefore, the net change in the distribution function due to scattering is given by the difference $P_{in}(k)$-$P_{out}(k)$:

$$\left(\frac{\partial f}{\partial t}\right)_{coll} = \frac{V}{8\pi^3}\int \{S(k', k)f(k')\,[1-f(k)] - S(k, k')f(k)\,[1-f(k')]\}\,dk' \tag{2.16}$$

Equation (2.16) is commonly known as the collision integral. $S(k,k')$ appearing in the collision integral is obtained from the scattering potential $V_s(r,t)$ via a quantum-mechanical calculation which is outlined in greater detail in Section 2.4. Replacing the right-hand side of the BTE in equation (2.6) with the collision integral, it now reads:

$$\begin{aligned}&\frac{\partial f}{\partial t} + v_g \cdot \nabla_r f + qE \cdot \nabla_p f \\ &= \frac{V}{8\pi^3}\int \{S(k', k)f(k')\,[1-f(k)] - S(k, k')f(k)\,[1-f(k')]\}\,dk'\end{aligned} \tag{2.17}$$

Equation (2.17) is an integro-differential equation in $f(r,p,t)$, and clearly simplifications are required in order to make the solution tractable. In the next section, we discuss one such simplification to the collision integral, known as the relaxation time approximation.

2.2.2 The Collision Integral in the Relaxation Time Approximation

The collision integral as it stands in equation (2.16) makes equation (2.17) a complex integro-differential equation whose solution under the most general conditions is not possible. In the relaxation time approximation (RTA), the collision integral is replaced by an algebraic equation that involves a parameter known as the relaxation time τ :

$$\left(\frac{\partial f}{\partial t}\right)_{coll} = -\frac{f-f_o}{\tau} \qquad (2.18)$$

where f is the distribution function that needs to be determined and f_o is the equilibrium distribution function (Maxwell-Boltzmann for non-degenerate gases and Fermi-Dirac for degenerate gases). The physical interpretation of equation (2.18) is that the scattering rate is proportional to the deviation from equilibrium f-f_o, and inversely proportional to the relaxation time (i.e. if τ is short, scattering rate would be high). Since scattering tends to return a system to equilibrium, τ represents the characteristic time over which a system relaxes back to equilibrium after an excitation has been removed. Since the RTA is a useful approximation to the BTE, the next section critically examines the conditions under which equation (2.18) is a valid approximation to the collision integral in equation (2.16).

2.2.3 Validity of the Relaxation Time Approximation

In Section 2.2.1, a formulation for $[\partial f/\partial t]_{coll}$ was presented (see equation (2.16)) that involved the quantum-mechanical entity $S(k,k')$. In Section 2.2.2, a relaxation time approximation to the collision integral was postulated that would considerably simplify solving the BTE. In this section, we discuss the conditions under which the RTA is valid and also show how the relaxation time τ is calculated from the transition rate $S(k,k')$. In Section 2.3 we will show how the calculation of mobility μ proceeds from the BTE once τ is known. Finally, in Section 2.4, we outline the quantum-mechanical calculation of $S(k,k')$ from first-order time-dependent perturbation theory.

We start by expressing the non-equilibrium distribution function f as the sum of a symmetric and an asymmetric part:

$$f = f_s + f_a \tag{2.19}$$

where f_s is symmetric and f_a is asymmetric in momentum. The benefit of splitting up f in this way is that f_s cannot cause any current flow due to its symmetrical nature, since there are equal number of carriers moving in opposite directions. Hence, any contribution to current would come from a non-zero f_a. The collision integral can also be split up as:

$$\left(\frac{\partial f}{\partial t}\right)_{coll} = \left(\frac{\partial f_s}{\partial t}\right)_{coll} + \left(\frac{\partial f_a}{\partial t}\right)_{coll} \tag{2.20}$$

The first simplification is to assume a non-degenerate semiconductor, i.e $f << 1$. Then all the [1-f] terms appearing in the collision integral in equation (2.16) reduce to unity. Hence, we get:

$$\left(\frac{\partial f_s}{\partial t}\right)_{coll} = \frac{V}{8\pi^3}\int \{S(k', k) f_s(k') - S(k, k') f_s(k)\}\, dk' \tag{2.21}$$

and

$$\left(\frac{\partial f_a}{\partial t}\right)_{coll} = \frac{V}{8\pi^3}\int \{S(k', k) f_a(k') - S(k, k') f_a(k)\}\, dk' \tag{2.22}$$

In equilibrium, $f_s = f_o$, and hence $[\partial f_s / \partial t]_{coll} = 0$. Thus, from equation (2.21) we find that at equilibrium, *S(k´,k) = S(k,k´)*, i.e. forward and backward transitions occur with equal probability[1]. Even under non-equilibrium conditions, if the applied fields are weak, the deviation from equilibrium is small, and the principle of detailed balance remains applicable. Moreover, $f_s \approx f_o$ under such conditions, and it is reasonable to assume that $[\partial f_s / \partial t]_{coll} = 0$. The collision term then reduces to:

$$\left(\frac{\partial f}{\partial t}\right)_{coll} = \frac{V}{8\pi^3}\int S(k, k')\, [f_a(k') - f_a(k)]\, dk' \tag{2.23}$$

1. Commonly known as the principle of detailed balance [18].

Equation (2.23) is still complicated because it is a functional of f_a. We need to arrive at a form for $[\partial f/\partial t]_{coll} = 0$ that would make it proportional to f_a, not a functional of f_a. Since integration in equation (2.23) is being carried over k', we can rewrite it as follows:

$$\left(\frac{\partial f}{\partial t}\right)_{coll} = \frac{V}{8\pi^3}\left[\int S(k,k')f_a(k')\,dk'\right] - \frac{V}{8\pi^3}\left[f_a(k)\int S(k,k')\,dk'\right] \tag{2.24}$$

If the first integral term on the right hand side of equation (2.24) vanishes, then the collision term would become proportional to f_a as desired. Since $f_a(k')$ is an odd function of k', if $S(k,k')$ can be shown to be an even function of k', then their product would be an odd function of k', and hence the integral would vanish when integrated over k'. $S(k,k')$ gives the probability that an electron in state k would scatter to state k'. For Bloch electrons, $v_g = \hbar k/m^*$. Hence, a velocity-randomizing scattering event is one in which an electron incident on the scattering center with velocity v_i has an equal probability of scattering off in any direction (i.e. $S(k,k')=S(k,-k')$ which implies that k' and $-k'$ are equally probable final states). Thus, for a given value of k, all values of k' are equally probable, implying that $S(k,k')$ is an *even* function of k'. That is why velocity randomizing collisions are also known as isotropic scattering events, since all angles after scattering are equally probably — the direction of the final wavevector is independent of the direction of the incident wavevector. Collisions with phonons are typically isotropic, whereas those with Coulombic centers are not. Thus, for isotropic scattering, the collision integral takes on the simple form:

$$\left(\frac{\partial f}{\partial t}\right)_{coll} = -\frac{V}{8\pi^3}f_a(k)\int S(k,k')\,dk' \tag{2.25}$$

Going back to the definition of the RTA in equation (2.18), we have:

$$\left(\frac{\partial f}{\partial t}\right)_{coll} = -\frac{f-f_o}{\tau(k)} = -\frac{f_a(k)}{\tau(k)} \tag{2.26}$$

Equating (2.25) and (2.26), the relationship between τ and $S(k,k')$ is then given by:

$$\frac{1}{\tau(k)} = \frac{V}{8\pi^3}\int S(k,k')\,dk' \tag{2.27}$$

The fact that τ in equation (2.27) is independent of f implies that the collision integral in equation (2.16) can be effectively reduced to the algebraic expression in equation (2.18). The approximations and assumptions made in reducing equation (2.16) to equation (2.25) are collectively referred to as the *relaxation time approximation* or RTA.

A velocity randomizing collision is not the only type of scattering event that is compatible with the RTA. Here, we discuss another type of scattering event, namely an elastic collision, that can treated in the RTA. For arbitrary electric field strengths, the non-equilibrium distribution function *f(k)* can be expanded in a series of spherical harmonic functions [41], [42]:

$$f(k) = \sum_{m=0}^{\infty} f_m(\varepsilon)\,P_m(\cos\theta) = f_o(\varepsilon)\,P_o(\cos\theta) + f_1(\varepsilon)\,P_1(\cos\theta) + \ldots \tag{2.28}$$

where θ is the angle between the electron wave vector $\boldsymbol{k}$ and the applied electric field, and ε is the electron energy given by $\varepsilon = (\hbar k)^2/2m^*$. The unknown functions $f_m(\varepsilon)$ need to be solved for by substituting for f in the BTE. The rationale for this choice of expansion is that the electric field is a symmetry-breaking operator that introduces a preferred axis (i.e. the direction of the electric field) along which a shift of the distribution function occurs. On the other hand, there is no breaking of symmetry in the azimuthal plane around the electric field vector, so that the polar angle becomes a good expansion function for the cylindrical symmetry of the problem. For low applied electric fields, the perturbation would be weak, and thus the series may be terminated after the second term to give:

$$f(k) = f_o + k\cdot\cos\theta\cdot f_1(\varepsilon) \tag{2.29}$$

Thus, according to our definition, $f_a(\boldsymbol{k}) = k\cdot\cos\theta\cdot f_1(\varepsilon)$. Substituting for f_a in equation (2.23) gives:

$$\left(\frac{\partial f}{\partial t}\right)_{coll} = \frac{V}{8\pi^3} f_1(\varepsilon)\,k\cos\theta\int S(\boldsymbol{k},\boldsymbol{k}')\left[\frac{f_1(\varepsilon')\,k'\cos\theta'}{f_1(\varepsilon)\,k\cos\theta} - 1\right]d\boldsymbol{k}' \tag{2.30}$$

If scattering is elastic, then $\varepsilon' = \varepsilon$ and $k' = k$. Note that $\boldsymbol{k}' \neq \boldsymbol{k}$. Then equation (2.30) reduces to:

$$\left(\frac{\partial f}{\partial t}\right)_{coll} = -\frac{V}{8\pi^3} f_a(\boldsymbol{k}) \int S(\boldsymbol{k}, \boldsymbol{k}') \left[1 - \frac{\cos\theta'}{\cos\theta}\right] d\boldsymbol{k}' \tag{2.31}$$

Therefore, if we define relaxation time as

$$\frac{1}{\tau(\boldsymbol{k})} = \frac{V}{8\pi^3} \int S(\boldsymbol{k}, \boldsymbol{k}') \left[1 - \frac{\cos\theta'}{\cos\theta}\right] d\boldsymbol{k}' \tag{2.32}$$

the collision integral takes on the familiar form $\left(\frac{\partial f}{\partial t}\right)_{coll} = -\frac{f_a(\boldsymbol{k})}{\tau(\boldsymbol{k})}$. Equation (2.32) can be simplified further if we assume spherical bands. Figure 2.4 represents the coordinate system illustrating a scattering event. We are interested in finding the relationship among

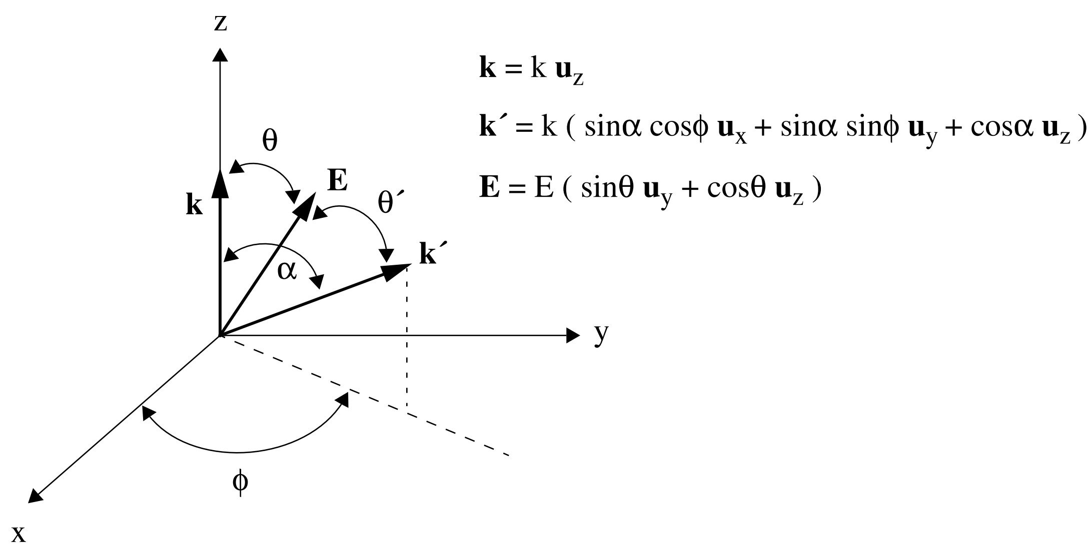

Figure 2.4 Coordinate system illustrating a scattering event. The incident carrier has wavevector **k**, the scattered electron has wavevector **k´**, and the applied force is **E**.

α (the angle between k and k´), θ, and θ'. Using the expression for dot product between two vectors $\mathbf{r}_1 \bullet \mathbf{r}_2 = |\mathbf{r}_1|\,|\mathbf{r}_2| \cos(\theta)$, we get for $\cos(\theta')$:

$$\frac{\boldsymbol{E} \cdot \boldsymbol{k}'}{|\boldsymbol{E}||\boldsymbol{k}'|} = \cos\theta' = \sin\theta\sin\alpha\sin\phi + \cos\theta\cos\alpha \tag{2.33}$$

and hence,

$$\frac{\cos\theta'}{\cos\theta} = \tan\theta\sin\alpha\sin\phi + \cos\alpha \tag{2.34}$$

For spherical bands, *S(k,k´)* is independent of ϕ; hence, *sin*ϕ would integrate to zero, leaving the *cos*α term. Thus, relaxation time can be expressed more simply as:

$$\frac{1}{\tau(\boldsymbol{k})} = \frac{V}{8\pi^3}\int S(\boldsymbol{k}, \boldsymbol{k}')\ [1 - \cos\alpha]\, d\boldsymbol{k}' \tag{2.35}$$

In summary, the assumptions under which the relaxation time approximation holds are:

(1) *Non-degenerate semiconductor.*

(2) *Low applied fields, i.e. carrier temperature ≈ lattice temperature.*

(3) *Deviation of the distribution function from equilibrium is small.*

(4) *Collisions are either velocity randomizing or elastic.*

(5) *If collisions are elastic, then energy bands must be spherical.*

2.3 Calculation of Mobility from the BTE in the RTA

The relaxation time approximation to the collision integral allows us to solve for the non-equilibrium distribution function *f(r,k,t)* for some special cases of interest. An important parameter appearing in the solution *f(r,k,t)* is the relaxation time, which is calculated from either equation (2.27) or (2.35) as discussed in the previous section. Equations (2.27) and (2.35) in turn need to know the transition rate *S(k,k´)*, which is calculated quantum mechanically from first-order time-dependent perturbation theory. In the next section, we show how *S(k,k´)* can be calculated if the nature of the interaction between the electron and the scattering center is known.

Once *f(r,k,t)* is known, it is possible to calculate macroscopic transport coefficients such as mobility and thermal conductivity. In this section, we show how the low-field mobility is calculated from the BTE using the RTA.

The expression for the convective current density[1] vector is given by

$$\boldsymbol{J} = qn\langle \boldsymbol{v}(\boldsymbol{r})\rangle \tag{2.36}$$

where $\boldsymbol{J} = J_x\hat{i} + J_y\hat{j} + J_z\hat{k}$, and <**v**(**r**)> is the average velocity vector at point **r**. Since the average is over the ensemble of particles, the average velocity is calculated by weighting it with the non-equilibrium distribution function *f(r,k,t)*. Therefore, in terms of the distribution function, the expression for $\boldsymbol{J}$ takes on the following form:

$$\boldsymbol{J} = 2\frac{q}{(2\pi)^3}\int \boldsymbol{v}f(\boldsymbol{r}, \boldsymbol{k}, t)\, d\boldsymbol{k} \tag{2.37}$$

where $f(r,k,t)=f_s(r,k,t)+f_a(r,k,t)$ as given in equation (2.19). Since the symmetric part of the distribution function does not contribute to current[2], equation (2.37) reduces to:

$$\boldsymbol{J} = 2\frac{q}{(2\pi)^3}\int \boldsymbol{v}f_a(\boldsymbol{r}, \boldsymbol{k}, t)\, d\boldsymbol{k} \tag{2.38}$$

In order to proceed with the calculation of $\boldsymbol{J}$, we first need to evaluate the non-equilibrium distribution function *f(r,k,t)* from the BTE using the RTA, which assumes the form:

$$\frac{\partial f}{\partial t} + v_g \cdot \nabla_r f + q\boldsymbol{E} \cdot \nabla_p f = -\frac{f_a(\boldsymbol{k})}{\tau(\boldsymbol{k})} \tag{2.39}$$

In steady state, $\partial f/\partial t = 0$, and if we further assume a spatially homogeneous semiconductor, $\nabla_r f = 0$ as well. The asymmetric part of the distribution f_a is then given by:

1. Convective current density is due to flow of particles. This is contrasted with the displacement current density which is due to the rate of change of electric field with respect to time at a certain point in space.
2. For the symmetric part of the distribution function, $f_s(r,k,t)=f_s(r,-k,t)$; hence, there are as many carrier moving to the right as there are to the left. Therefore, net movement of the carriers is zero.

$$f_a(k) = -\tau(\boldsymbol{k})\frac{q\boldsymbol{E}}{\hbar}\cdot\nabla_k f \tag{2.40}$$

Relaxation time approximation holds under the condition that f should not deviate significantly from f_o. By replacing f by f_o in the momentum-space gradient, and with a change of variables, we get:

$$\nabla_k f \approx \nabla_k f_o = \frac{\partial f_o}{\partial \varepsilon}\cdot\nabla_k \varepsilon(k) = \hbar\frac{\partial f_o}{\partial \varepsilon}\boldsymbol{v} \tag{2.41}$$

Therefore, f_a takes on the following form:

$$f_a(\boldsymbol{k}) = -q\tau(\boldsymbol{k})\frac{\partial f_o}{\partial \varepsilon}(\boldsymbol{v}\cdot\boldsymbol{E}) \tag{2.42}$$

Hence, $\boldsymbol{J}$ is now given by:

$$\boldsymbol{J} = -\frac{q}{4\pi^3}\int\tau(\boldsymbol{k})\frac{\partial f_o}{\partial \varepsilon}\boldsymbol{v}(\boldsymbol{v}\cdot\boldsymbol{E})\,d\boldsymbol{k} \tag{2.43}$$

According to Ohm's law, $\boldsymbol{J} = \sigma\boldsymbol{E}$. In tensor form, $\boldsymbol{J}$ is given by:

$$\begin{pmatrix} J_x \\ J_y \\ J_z \end{pmatrix} = \begin{bmatrix} \sigma_{xx} & \sigma_{xy} & \sigma_{xz} \\ \sigma_{yx} & \sigma_{yy} & \sigma_{yz} \\ \sigma_{zx} & \sigma_{zy} & \sigma_{zz} \end{bmatrix}\begin{pmatrix} E_x \\ E_y \\ E_z \end{pmatrix} \tag{2.44}$$

Equating (2.43) and (2.44), we see that an entry in the conductivity tensor is given by:

$$\sigma_{ij} = -\frac{q}{4\pi^3}\int\tau(\boldsymbol{k})\frac{\partial f_o}{\partial \varepsilon}v_i v_j d\boldsymbol{k} \tag{2.45}$$

For elastic scattering mechanisms $|\mathbf{k}|=|\mathbf{k}'|$, and hence the transition rate is independent of the initial direction of the wavevector $\mathbf{k}$ since $S(\mathbf{k},\mathbf{k}')=S(\mathbf{k}-\mathbf{k}')=S(|\mathbf{k}|,\theta)$. Thus, $\tau(\mathbf{k})$ can be expressed as $\tau(\varepsilon)$. Moreover, if the band structure is assumed to be isotropic, the conductivity tensor becomes diagonal [60]. Thus, any one component on the diagonal is given by:

$$\sigma_i = qn\mu = -\frac{q}{4\pi^3}\int \tau(\varepsilon)\frac{\partial f_o}{\partial \varepsilon} v_i^2 d\boldsymbol{k} \tag{2.46}$$

where i=x, y, or z, and μ is the mobility. Assuming Maxwell-Boltzmann statistics, $f_o \propto e^{-\varepsilon/kT}$, which implies that $\partial f_o/\partial\varepsilon = -f_o/kT$. Given that the electron concentration n can be written as:

$$n(r,t) = \frac{1}{4\pi^3}\int f(r,k,t)\, d\boldsymbol{k} \tag{2.47}$$

the expression for mobility[1] becomes:

$$\mu = \frac{\dfrac{q}{4\pi^3}\displaystyle\int \tau(\varepsilon)\frac{f_o}{kT} v_i^2 d\boldsymbol{k}}{\dfrac{1}{4\pi^3}\displaystyle\int f_o d\boldsymbol{k}} \tag{2.48}$$

Since we are dealing with an isotropic band structure, we can perform the integration over the scalar ε instead of the vector $\boldsymbol{k}$. For an isotropic band structure, the constant energy surfaces are spherical, i.e. $\varepsilon = (\hbar k)^2/2m^*$. The density of states in energy is defined as:

$$\begin{aligned} D(\varepsilon)\, d\varepsilon &= \text{No. of states in } d\varepsilon/\text{Crystal Volume} \\ &= [\,(\text{Vol in k-space corresponding to } d\varepsilon)\cdot D(k)\,]\,/\,Vol \\ &= d\boldsymbol{k}\cdot\frac{1}{4\pi^3} \end{aligned} \tag{2.49}$$

From the equipartition of energy, $v^2 = v_x^2 + v_y^2 + v_y^2 = 3v_i^2$, and

1. In semiconductors, mobility is treated separately from conductivity since n can vary by orders of magnitude in doped semiconductors, and μ can vary independently of n. However, in metals, n is constant and very high, and conductivity is taken to be synonymous with mobility.

$\varepsilon = (1/2)\,m^*v^2 = (3/2)\,m^*v_i^2$. Changing the variable of integration from $\boldsymbol{k}$ to ε and substituting for v_i^2, the expression for mobility in equation (2.48) simplifies to:

$$\mu = \frac{q\int \tau(\varepsilon)\frac{f_o}{kT}\left(\frac{2\varepsilon}{3m^*}\right)4\pi^3 D(\varepsilon)\,d\varepsilon}{\int f_o 4\pi^3 D(\varepsilon)\,d\varepsilon} \tag{2.50}$$

Since $f_o \propto e^{-\varepsilon/kT}$, and in 3D, $D(\varepsilon) = \frac{(2m^*)^{3/2}}{2\pi^2\hbar^3}\varepsilon^{1/2}$, the expression for mobility in equation (2.50) becomes:

$$\mu = \frac{\frac{q}{m^*}\int\left(\frac{\varepsilon}{kT}\right)\tau(\varepsilon)\,e^{-\frac{\varepsilon}{kT}}\left(\frac{\varepsilon}{kT}\right)^{1/2}d\left(\frac{\varepsilon}{kT}\right)}{\frac{3}{2}\int e^{-\frac{\varepsilon}{kT}}\left(\frac{\varepsilon}{kT}\right)^{1/2}d\left(\frac{\varepsilon}{kT}\right)} \tag{2.51}$$

If we define $x \equiv \varepsilon/kT$, and are able to express $\tau(\varepsilon)$ as

$$\tau(\varepsilon) = \tau_o \cdot \left(\frac{\varepsilon}{kT}\right)^s \tag{2.52}$$

then,

$$\mu = \frac{\left(\frac{q\tau_o}{m^*}\right)\int x^{\left(\frac{3}{2}+s\right)}e^{-x}dx}{\frac{3}{2}\int x^{1/2}e^{-x}dx} \tag{2.53}$$

Now, $\int_0^\infty e^{-x}x^s dx = \Gamma(s+1)$, where $\Gamma(1/2) = \sqrt{\pi}$ and $\Gamma(s+1) = s\Gamma(s)$. Therefore, equation (2.53) can be rewritten as:

$$\mu = \frac{q\tau_o}{m^*} \cdot \frac{\Gamma(s+5/2)}{\Gamma(5/2)} \tag{2.54}$$

Equation (2.54) specifies the relationship between the momentum relaxation time $\tau(\varepsilon)$ and mobility μ. Momentum relaxation time when expressed as $\tau(\varepsilon)$ specifies the time it would take for an electron with energy ε to randomize its initial momentum. Since electrons in a system are distributed in energy, electrons with different energies would take different times to randomize their initial momentum. Mobility can thus be viewed as being proportional to the *average* time it takes the electron gas to randomize its initial momentum.

In summary, starting with Boltzmann's transport equation as given in equation (2.17), the following assumptions and simplifications allow us to derive an expression for low-field mobility:

(1) *In the relaxation time approximation, the collision integral in equation (2.16) can be reduced to the simplified form in equation (2.26) provided the collisions are either elastic (as in Coulomb scattering) or velocity randomizing (as in acoustic phonon scattering).*

(2) *An implicit assumption in the RTA is that the non-equilibrium distribution function f is only slightly perturbed from the equilibrium distribution function f_o. Hence $\nabla_k f \approx \nabla_k f_o$.*

(3) *Maxwell-Boltzmann statistics is assumed, which is consistent with the assumption underlying the derivation of the BTE that the gas should be weakly interacting. If the gas is dense, then due to strong interactions among the particles, the single-electron distribution function f(r,p,t) loses its validity.*

(4) *Momentum relaxation time is assumed to be independent of the direction of the wavevector of the incident electron. This can only be true if the scattering event is elastic, i.e. $S(\boldsymbol{k}, \boldsymbol{k}') = S(\boldsymbol{k} - \boldsymbol{k}') = S(|\boldsymbol{k}|, \theta)$ which implies that the transition rate depends upon the speed with which the carriers approach the scattering potential and the angle through which they are deflected. Under this simplification, $\tau(\boldsymbol{k})$ can be written as $\tau(\varepsilon)$.*

(5) *The band structure is assumed to be spherical (i.e. isotropic) and parabolic. The assumption of isotropy allows us to perform integrations over the scalar*

quantity ε *as opposed to the vector quantity* ***k***.

Thus, the calculation of mobility in equation (2.54) starting with the momentum relaxation time τ(ε) is a purely classical calculation since it involves the use of the classically-described distribution function *f(r,k,t)*. Momentum relaxation time can be calculated from either equation (2.27) or equation (2.35). In either case, we need to know the transition rate *S(k,k´)* first, calculation of which is based on purely quantum mechanical terms. We discuss this calculation in the next section. The mix of quantum and classical calculations in calculating the macroscopic transport parameter mobility is what makes this particular treatment *semi-classical* in nature.

2.4 Calculation of the Transition Rate from Perturbation Theory

In this section, we draw the connection between the transition rate *S(k,k´)* and scattering potential $V_s(r, t)$ which describes the potential field created by the scattering center. It is the interaction of an electron with the scattering potential that is phenomenologically known as an scattering event, and mathematically described through time-dependent perturbation theory as we discuss next.

At the fundamental level, Schrodinger's equation describes the interaction of the electrons with various forces, or equivalently potential fields, appearing in the solid:

$$i\hbar\frac{\partial\Psi}{\partial t} = [V_c(r) + V_a(r, t) + V_s(r, t)]\Psi - \frac{\hbar^2}{2m}\nabla^2\Psi \qquad (2.55)$$

The crystal potential, $V_c(r)$, is periodic in nature and it describes the electrostatic potential due to the atomic cores. $V_a(r, t)$ describes potentials that are built-in or applied to the device, while $V_s(r, t)$ describes the scattering potential due to random deviations in potential that may be caused by ionized impurities or lattice vibrations. As discussed in Section 2.2.1, applied potentials are treated classically, and hence $V_a(r, t)$ need not be considered in equation (2.55). Even with this simplification, it is not possible to solve equation (2.55). We make another simplification by neglecting $V_s(r, t)$ under the assumption that it is much smaller than $V_c(r)$. The resulting equation yields the well-known Bloch wavefunction as its solution, described by equation (2.9).

Since $V_s(r, t) \ll V_c(r)$, it is treated as a small perturbation to $V_c(r)$. The effect of such a perturbation is to cause an electron initially in Bloch state $\Psi_i(r, t)$ to make a transition to another Bloch state $\Psi_f(r, t)$. The rate of transition *S(k,k´)* is given by the Fermi's Golden Rule [70] that is derived from first-order time-dependent perturbation theory [70]:

$$S(k, k') = \frac{2\pi}{\hbar} \left|\langle\Psi_f|V_s|\Psi_i\rangle\right|^2 \delta[\varepsilon(k_f) - \varepsilon(k_i)] \tag{2.56}$$

The rate of transition quadratically depends upon how strongly the scattering potential V_s couples the two Bloch states Ψ_i and Ψ_f. This coupling is expressed through the matrix element $<\Psi_f \mid V_s \mid \Psi_i>$. The delta function appearing in equation (2.56) expresses the conservation of energy during the scattering process.

The task that finally remains is identifying the nature of the scattering potential $V_s(r)$. The discussion so far is applicable to all kinds of scattering mechanisms. However, calculation of $V_s(r)$ specifically depends upon the nature of the scattering process. In the next chapter, we shall discuss in considerable detail how to set up V_s for a two-dimensional Coulombic potential that is screened by a two-dimensional electron gas. Once V_s has been calculated, we shall use the machinery developed in this chapter to calculate the mobility for two-dimensional Coulombic scattering.

More commonly, the Fourier transform of the scattering potential $V_s(q)$ is easier to calculate than $V_s(r)$ itself. As we shall show, it is not necessary to convert back to real space *r* since we can very well work in its Fourier space representation.

When the matrix element $\langle\Psi_f|V_s|\Psi_i\rangle$ is expressed in the coordinate-space representation, we get:

$$\langle\Psi_f|V_s|\Psi_i\rangle = \int_v \Psi_f^*(r)\, V_s(r)\, \Psi_i(r)\, dr \tag{2.57}$$

The Fourier series expansion of $V_s(r)$ is given by $V_s(r) = \sum_q V_s(q)\, e^{i(q \cdot r)}$, where the Fourier coefficients are given by $V_s(q) = \frac{1}{V}\int_v V_s(r)\, e^{-i(q \cdot r)}$. For Bloch electrons, $\psi_k = u_k(r)\, e^{i(k \cdot r)}$. Hence, equation (2.57) becomes [59]

$$
\begin{aligned}
\langle \Psi_f | V_s | \Psi_i \rangle &= \int_v \left[u_{k_f}{}^* e^{-ik_f \cdot r} \right] \bullet \left[\sum_q V_s(q)\, e^{iq \cdot r} \right] \bullet \left[u_{k_i} e^{ik_i \cdot r} \right] dr \\
&= \sum_q V_s(q) \int_v u_{k_f}{}^*(r)\, u_{k_i}(r)\, e^{i(q + k_i - k_f) \cdot r} dr
\end{aligned}
\tag{2.58}
$$

Since the integral is zero except when $q = k_f - k_i$, equation (2.58) simplifies to

$$
\langle \Psi_f | V_s | \Psi_i \rangle = V(q) \int_v u_{k_f}{}^*(r)\, u_{k_i}(r)\, dr \tag{2.59}
$$

For parabolic bands, $u_{k_f}(r) = u_{k_i}(r)$; hence, the overlap integral in equation (2.59) reduces to unity, and we get

$$
\langle \Psi_f | V_s | \Psi_i \rangle = V(q) \tag{2.60}
$$

Therefore, calculation of the matrix element simply reduces to evaluating the Fourier transform $V(q)$ of the perturbing potential $V_s(r)$, and equation (2.56) simplifies to:

$$
S(k, k') = S(q) = \frac{2\pi}{\hbar} \left| V_s(q) \right|^2 \delta[\varepsilon(k') - \varepsilon(k)] \tag{2.61}
$$

2.5 Summary

In this chapter, we have presented a systematic treatment of the calculation of mobility μ from the Boltzmann Transport Equation provided the scattering potential $V_s(r)$ is known. In the next chapter, we shall calculate $V_s(r)$ for a screened two-dimensional Coulombic potential, and make use of the methodology outlined in this chapter to calculate the mobility associated with this scattering potential.

We summarize here the mobility calculation methodology presented in this chapter. Starting with a description of the scattering potential $V_s(q)$, the transition rate $S(k,k')$ is calculated according to Fermi's golden rule as given in equation (2.61):

$$S(k, k') = S(q) = \frac{2\pi}{\hbar} \left| V_s(q) \right|^2 \delta[\varepsilon(k') - \varepsilon(k)] \tag{2.61}$$

If the scattering mechanism is elastic, as in Coulombic scattering, then the momentum relaxation $\tau(\varepsilon)$ is given by equation (2.35):

$$\frac{1}{\tau(\boldsymbol{k})} = \frac{V}{8\pi^3} \int S(\boldsymbol{k}, \boldsymbol{k}') [1 - \cos\alpha] \, d\boldsymbol{k}' \tag{2.35}$$

Expressing $\tau(\varepsilon)$ as $\tau_o (\varepsilon / kT)^s$, where s denotes the energy dependence of $\tau(\varepsilon)$, mobility μ is given by equation (2.54):

$$\mu = \frac{q\tau_o}{m^*} \cdot \frac{\Gamma(s + 5/2)}{\Gamma(5/2)} \tag{2.54}$$

It should be noted that the calculation methodology for mobility presented in this chapter is *semiclassical* in nature: calculation of scattering potential and transition rate invokes quantum mechanics, whereas calculation of momentum relaxation time and mobility is based on classical laws.

Chapter 3

Coulombic Scattering in MOS Inversion Layers

3.1 Introduction

Design of low-power systems has gained considerable interest in recent years, particularly for portable applications such as laptops computers and cellular phones. For maximum savings in power dissipation with minimum impact on performance, optimizations would have to be carried out at all levels in the design hierarchy — device, circuit, system, and software [97]. To address the issue of power dissipation in today's ULSI chips, various technology options are being explored that would help minimize both standby and active power dissipation without compromising the operating speed. One such option is the design of low threshold devices with aggressively scaled V_{dd} [84]. Proper design and optimization of such devices requires accurate prediction of threshold voltage (V_T) and drain leakage current (I_{off}), particularly since small changes in V_T can significantly alter I_{off}. It is recognized that the I-V characteristics of a MOSFET in the subthreshold region, and hence the calculation of $\mathrm{V_T}$, are severely affected by the Coulombic scattering of inversion-layer electrons due to channel impurities [2]. This is exacerbated in scaled devices, that tend to have high channel doping levels to prevent undesirable short channel effects. However, what has been lacking is accurate characterization and fundamental modeling of Coulombic scattering in the inversion layer.

In light of the above concerns, we present in this chapter a first-principles calculation of Coulombic scattering in the quasi two-dimensional inversion layer. The objectives are two fold: (i) to formulate a closed-form (analytical) model for Coulombic scattering that can be readily implemented in moment-based device simulators, and (ii) a physically-based model is an essential requirement for predictive device simulation.

The organization of this chapter is as follows. In Section 3.2, we discuss the new modeling approach and identify the deficiencies of existing models. There are two aspects to Coulombic scattering: the screened and unscreened components. Unscreened Coulombic scattering is due to a bare Coulombic potential which, if *screened* by free carriers, results in screened Coulombic scattering. An important aspect of first-principles modeling is the formulation of the scattering potential for both screened and unscreened two-dimensional Coulombic charge effects. Once the scattering potentials have been calculated, we then employ the methodology developed in the previous chapter to calculate respective mobility terms from their scattering potentials. Section 3.2.1 is devoted to the calculation of unscreened Coulombic scattering, and in Section 3.2.2, screened Coulombic scattering is considered.

In Section 3.3, we test the accuracy of the new 2D model by comparing it with experimental data obtained from the literature. The new model, properly accounting for 2D confinement and quantum mechanical effects, is shown to be in much better agreement with experimental data compared to the 3D model by Brooks and Herring.

In Section 3.4, we investigate the effect of substrate bias on screened Coulombic scattering. This experimental investigation confirms the hypothesis that Coulombic scattering is a stronger function of electron density compared to the effective normal field in the inversion layer. It will be seen in Chapter 4 that it is this property of Coulombic scattering that causes marked deviations from the universal behavior of mobility [43].

In Section 3.5, we present a *new* systematic technique for extracting unscreened Coulombic mobility from experimental data. Currently, techniques only exist for extracting screened Coulombic mobility. We then present a comparison between the extracted data and various models for unscreened Coulombic scattering, and show that our new modeling approach yields better fits than 3D classical models previously published in literature.

Finally in Section 3.6, we establish the importance of modeling Coulombic scattering in MOS inversion layers by demonstrating its impact on critical design parameters such as threshold voltage and off-state leakage current.

3.2 New Modeling Approach

The scattering of inversion layer electrons by charge centers in its vicinity is generically termed as Coulombic scattering. Possible sources of charge centers include ionized impurities in the channel, interfacial charge, fixed oxide charge, and mobile oxide charge. Since we shall only be concerned with modeling ionized impurity scattering, in the ensuing discussion Coulombic scattering will be synonymous with impurity scattering.

The three parameters that affect impurity scattering in MOS inversion layers are ionized impurity concentration, carrier density and temperature. Charge carriers respond to an electrostatic potential in such a way as to always reduce its strength. This effect is known as screening, and it is typically proportional to the density of mobile carriers. In the limit of low carrier concentrations, scattering is essentially due to the bare Coulomb potential and is termed as *unscreened* Coulombic scattering. With the increase of carrier density in the inversion layer, Coulombic scattering makes a transition from the unscreened to the *screened* regime.

From a physical stand point, since there is a smooth transition from one regime to the next, one might expect that a single mathematical expression would be sufficient to model both the regimes. However, such is not the case since a mathematical singularity occurs if the carrier density is set to zero in the expression for screened Coulombic scattering. As a result, a separate formulation is required for unscreened Coulombic scattering.

Over the last three decades, Coulombic scattering has received scrutiny by both theorists and experimentalists since it was recognized earlier on that ionized impurity scattering would be a limiting factor in carrier transport in semiconductors. The earliest theoretical works on Coulombic scattering include that of Brooks and Herring [13] and of Conwell and Weisskopf [12]. Brooks and Herring computed the screened Coulombic mobility of a three dimensional electron gas whereas Conwell and Weisskopf computed the unscreened mobility. While these 3D models were expressed in closed form, and hence suitable for implementation in a 2D device simulator, they did not accurately model Coulombic scattering in MOS inversion layers, as will be shown in Sections 3.3 and 3.5. Thus, what we need to consider are analytical models formulated for a two-dimensional electron gas.

With the emerging interest in MOS systems, several works appeared on Coulombic scattering in a two-dimensional electron gas. The seminal paper on this subject by Stern and Howard [8] presented a theoretical treatment of Coulombic scattering in MOS inversion layers assuming that only the lowest sub-band (i.e. the ground state) was occupied. Since the treatment was quite rigorous, they were unable to arrive at a closed form solution for mobility. Instead, the results were obtained through numerical integration for very low temperature cases. The objective here is in achieving a closed form solution for mobility, applicable at room temperature, that can be implemented in a moment-based device simulator such as PISCES [54].

Following the work of Stern and Howard [8], Sah *et. al.* [47] calculated a closed-form solution for unscreened Coulombic mobility in MOS inversion layers. However, this work only considered the scattering of electrons by fixed oxide charges, which at that time was the dominant source of Coulombic scattering. However, significant advances in MOS processing technology have led to a considerable reduction of interfacial and oxide charges in modern day MOSFETs. Instead, now the dominant source of Coulombic scattering in the inversion layer is due to ionized impurities in the channel [1] whose concentration, as a result of device scaling, continues to increase in an effort to suppress short channel effects such as punchthrough and drain-induced-barrier lowering.

Subsequently, Ning and Sah [98] expanded on their earlier work of Sah [47] and included screening among other effects in their calculation. However, this work still concentrated on Coulombic scattering due to oxide charges. Based on current needs, interest has now shifted to the study of Coulombic scattering due to channel dopants.

Other works have appeared in literature that have treated impurity scattering in a quantum well [100]-[104] instead of an MOS inversion layer. While the structure is different, the problem is essentially similar since in both cases the electron gas behaves as a quasi two-dimensional system. However, the major shortcoming with these analyses is that they treat Coulombic scattering only in the low-temperature limit.

Recently, a comprehensive account of Coulombic scattering has been presented by Gamiz *et. al.* [99]. Due to the completeness and complexity of their treatment, they are only able to calculate the mobility numerically. Such a model however is not suitable for implementation in a drift-diffusion device simulator.

In direct support of creating a mobility model for Coulombic scattering that can be implemented in a device simulator requires the following features:

(1) The model should be analytical — expressed in closed-form.

(2) *The model should consider Coulombic scattering due to channel dopants.*

(3) *The model should be applicable at room temperature.*

Since none of the previous works provide a model that possess the features mentioned above, our objective in performing a first-principles calculation of Coulombic scattering is to arrive at a model that would exhibit all these three features. Since screened scattering logically follows unscreened scattering, we first present a calculation for unscreened Coulombic scattering in Section 3.2.1 followed by a calculation for screened Coulombic scattering in Section 3.2.2.

3.2.1 Unscreened Coulombic Scattering

In this section, we shall compute the mobility due to unscreened Coulombic scattering. In computing this mobility, we will ignore the screening effect due to the electron gas which will be taken up in the next section. Assume that the electron gas can move in the *x-y* plane and is confined in the *z* direction[1]. Electrons are considered confined or *quantized* if their deBroglie wavelength is larger than or comparable to the width of the confining potential. The deBroglie wavelength of electrons, given by $\lambda = h/\sqrt{2m^*kT}$, is approximately 150Å at room temperature, whereas the thickness of the inversion layer is typically around 50Å to 100Å. Thus, we are justified in treating the inversion layer as a two dimensional electron gas. However, due to its finite extension in the *z* direction, the inversion layer is considered as a quasi 2D as opposed to a strictly 2D gas. As we shall see, the finite extension of the inversion layer in the *z* direction leads to further complexity in our analysis of Coulombic scattering.

The Coulomb potential due to a charge center located at ($\mathbf{r}_i$, z_i) in the semiconductor is given by [8]

$$V(r,z) = \left(\frac{e^2}{4\pi\kappa_{si}\varepsilon_o}\right)\left[(r-r_i)^2 + (z-z_i)^2\right]^{-1/2} + \left(\frac{e^2}{4\pi\varepsilon_o}\right)\left(\frac{\kappa_{si}-\kappa_{ox}}{\kappa_{si}(\kappa_{si}-\kappa_{ox})}\right)\left[(r-r_i)^2 + (z+z_i)^2\right]^{-1/2} \tag{3.1}$$

1. z = 0 corresponds the Si/SiO_2 interface. z > 0 is in silicon whereas z < 0 is in the oxide.

where κ_{si} and κ_{ox} is the dielectric constant of silicon and oxide respectively, and ε_o is the permittivity of free space. The first term on the right hand side of equation (3.1) corresponds to the direct interaction between the electron at (**r**, z) and the charge center at ($\mathbf{r}_i$, z_i), whereas the second term corresponds to the interaction between the electron and the charge center's *image* at ($\mathbf{r}_i$, -z_i). The image charge is a result of the differing dielectric constants of oxide and silicon.

Since inversion layer electrons are restricted to move in the x-y plane, they would only scatter off potential perturbations that they see in the x-y plane. Therefore, we are only interested in determining the potential variations along that plane. To do so, we need to calculate the two dimensional Fourier transform of the potential appearing in equation (3.1), where the result is given by [8]

$$V(q, z_i) = \frac{e^2}{2\tilde{\kappa}\varepsilon_o q} F(q, z_i) \tag{3.2}$$

where $\tilde{\kappa} = (\kappa_{si} + \kappa_{ox})/2$ and the form factor $F(q, z_i)$ accounts for the separation z_i between the impurity layer and the electron gas and also for the finite extension of the electron gas in the z dimension. Considering that the wavefunction of inversion-layer electrons in the ground state is given by $\zeta_o(z)\, e^{i(k \cdot r)}$, where $\zeta_o(z)$ is the envelope function, $F(q, z_i)$ is also given by [8]

$$F(q, z_i) = \frac{1}{2}\int_o^{\infty}|\zeta_o(z)|^2\left\{\left(1 + \frac{\kappa_{ox}}{\kappa_{si}}\right)e^{-q|z - z_i|} + \left(1 - \frac{\kappa_{ox}}{\kappa_{si}}\right)e^{-q(z + z_i)}\right\}dz \tag{3.3}$$

The form factor appearing in equation (3.3) is complex enough that it does not permit a closed form solution for mobility. In order to make the solution tractable, we assume the inversion layer to be infinitesimally thin, i.e. $\zeta_o(z) = \delta(z)$. In this strictly two dimensional limit, equation (3.3) simplifies to

$$F(q, z_i) = e^{-q|z_i|} \tag{3.4}$$

Inserting $V(q)$ from equation (3.2) into (2.61), the transition rate $S(q,z_i)$ takes the following form:

$$S(q, z_i) = \frac{2\pi}{\hbar}\left(\frac{e^2}{2\tilde{\kappa}\varepsilon_o q}\, e^{-q|z_i|}\right)^2 \delta[\varepsilon(k') - \varepsilon(k)] \tag{3.5}$$

The transition rate given in equation (3.5) is due to a sheet of impurity atoms located at a distance z_i from the electron gas. Since, the impurity atoms are distributed in a three dimensional space underneath the interface, we need to sum the contribution due to each sheet of impurity atoms. If this distribution is given by *N(z)*, then the total transition rate *S(q)* is given by

$$S(q) = \frac{2\pi}{\hbar}\left(\frac{e^2}{2\tilde{\kappa}\varepsilon_o q}\right)^2 \delta[\varepsilon(k') - \varepsilon(k)] \int_o^{\infty} N(z)\, e^{-2qz} dz \tag{3.6}$$

In an attempt to arrive at a closed form solution, we assume that scattering is primarily due to a two-dimensional sheet of charge located at the interface, i.e. $N(z) = N_{2D}\,\delta(z)$. In modern submicron MOSFETs, the channel region is typically doped more heavily than the substrate to suppress drain-induced-barrier lowering (DIBL) and surface punchthrough effects. Thus, it is reasonable to assume that impurity scattering is primarily due to dopants that are situated near the interface. With this assumption, equation (3.6) reduces to

$$S(q) = \frac{2\pi}{\hbar}\left(\frac{e^2}{2\tilde{\kappa}\varepsilon_o q}\right)^2 N_{2D}\ \delta[\varepsilon(k') - \varepsilon(k)] \tag{3.7}$$

Since, Coulombic scattering is an elastic scattering mechanism, the scattering rate or equivalently the inverse of the momentum relaxation time is calculated according to equation (2.35) :

$$\frac{1}{\tau_m} = \frac{N_{2D}}{(2\pi)^2}\,\frac{2\pi}{\hbar}\left(\frac{e^2}{2\tilde{\kappa}\varepsilon_o}\right)^2 \int \frac{1}{q^2}\, \delta[\varepsilon(k') - \varepsilon(k)]\ [1 - \cos\theta]\, d\mathbf{k} \tag{3.8}$$

where **k** is the wavevector in the x-y plane, and in 2D $d\mathbf{k} = k\ dk\ d\theta$. The relationship between k, θ, and q for elastic scattering is illustrated in Fig. 3.1 In light of this

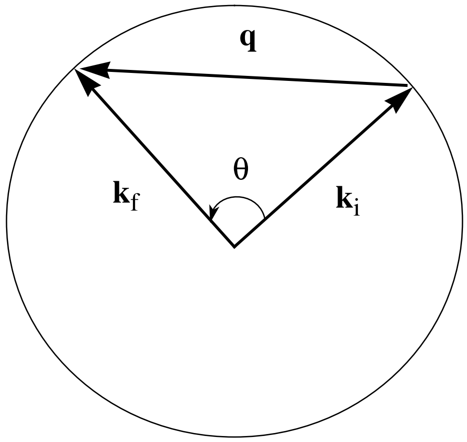

In elastic scattering, $|\mathbf{k}_f| = |\mathbf{k}_i|$

According to the law of cosines,

$$q^2 = k^2 + k^2 - 2k^2 \cos\theta$$
$$= k^2 [\, 2 - 2\cos\theta \,]$$
$$= 4k^2 \sin^2(\theta/2)$$
$$\therefore \quad q = 2\,k \sin(\theta/2)$$

Figure 3.1 Relationship among the various variables in elastic scattering.

relationship, equation (3.8) can be transformed to

$$\frac{1}{\tau_m} = \frac{N_{2D}}{2\pi\hbar}\left(\frac{e^2}{2\tilde{\kappa}\varepsilon_o}\right)^2 \left(\int \frac{1}{k}\,\delta\,[\varepsilon\,(k') - \varepsilon\,(k)\,]\,dk\right)\left(\int_o^{\pi} \frac{1}{2}\,d\theta\right) \tag{3.9}$$

For spherical parabolic bands, $\varepsilon = (\hbar k)^2 / (2m^*)$, and the transformation $dk = \left[m^* / \hbar^2 k\right] d\varepsilon$ simplifies the integral in equation (3.9) with the delta function to $m^* / (\hbar k)^2$. Thus, the expression for momentum relaxation simplifies to :

$$\tau_m\,(\varepsilon) = \frac{32\hbar\,(\tilde{\kappa}\varepsilon_o)^2\,(kT)}{e^4 N_{2D}}\left(\frac{\varepsilon}{kT}\right) \tag{3.10}$$

Mobility is calculated according to equation (2.54), and with the energy dependence of τ_m equal to unity, s equals 1 in equation (2.52). Hence, mobility due to unscreened Coulombic scattering is given by

$$\mu_{unscreened} = \frac{80\ \bar{h}\ (\tilde{\kappa}\varepsilon_o)^2\ (kT)}{e^3\ m^*\ N_{2D}} \tag{3.11}$$

3.2.2 Screened Coulombic Scattering

Having calculated the expression for unscreened mobility in the previous section, we now consider the effect of screening due to inversion layer electrons on Coulombic scattering. Screening is actually a many-body phenomena since it involves the collective motion of the electron gas. To keep the analysis simple, we shall consider screening only in the context of the linear response theory, wherein applied fields are treated as small perturbations to which the response of the electron gas is assumed linear. We consider a free electron gas that is subjected to a perturbation that varies in both space and time. Suppose that the potential seen by an electron at **r** and at time *t* is given by

$$V_{ext}(\mathbf{r}, t) = V_{ext}\ e^{i(\mathbf{q} \cdot \mathbf{r} + \omega t)} \tag{3.12}$$

This externally applied potential gives rise to a fluctuation in electron density that obeys the same dependence in space and time :

$$\rho_{ind}(\mathbf{r}, t) = \rho_{ind}\ e^{i(\mathbf{q} \cdot \mathbf{r} + \omega t)} \tag{3.13}$$

According to Poisson's equation, the induced charge density results in an induced potential $V_{ind}(\mathbf{r},t)$ with the same **q** and ω dependence :

$$\nabla^2 V_{ind}(\mathbf{r}, t) = -\frac{e}{\kappa_{si}\ \varepsilon_o}\ \rho_{ind}(\mathbf{r}, t) \tag{3.14}$$

In the random phase approximation [105], the electrons respond linearly to the effective potential V_{eff}, which is given by the sum of V_{ext} and V_{ind}. Thus, we have

$$\rho_{ind} = e\chi(q, \omega)\ V_{eff} \tag{3.15}$$

where $\chi(q,\omega)$ is known as the screened response function [86]. From equations (3.14) and (3.15), we get the following relationship between V_{ext} and V_{eff} for a two-dimensional electron gas [86] :

$$V_{ext} = \left[1 - \left(\frac{e^2}{2\kappa_{si}\,\varepsilon_o q}\right)\chi(q,\omega)\right]V_{eff} \tag{3.16}$$

If we define

$$V_{ext} = \varepsilon(q,\omega)\,V_{eff} \tag{3.17}$$

where $\varepsilon(q,\omega)$ is the longitudinal dielectric function of the electron gas [87], then

$$\varepsilon(q,\omega) = 1 - V_{ext}(q)\cdot\chi(q,\omega) \tag{3.18}$$

where $V_{ext}(q)$ is the 2D Fourier transform of the 3D Coulomb potential $e^2/(4\pi\kappa_{si}\varepsilon_o r)$ [86]. The interaction potential between two inversion-layer electrons is given by [8], [88] :

$$V_{ext}(q) = \frac{e^2}{2\tilde{\kappa}\varepsilon_o q}F(q) \tag{3.19}$$

where $\tilde{\kappa} = (\kappa_{si} + \kappa_{ox})/2$ and $F(q)$ is the form factor accounting for the finite width of the inversion layer. Neglecting the potential due to image charges [8], the form factor is given by

$$F(q) = \int_o^{\infty}\left|\zeta_o(z)\right|^2 e^{-qz}dz \tag{3.20}$$

where $\zeta_o(z)$ is the ground-state envelope function. To keep the analysis tractable, we assume that the inversion layer has an infinitesimal thickness, i.e. $\zeta_o(z) = \delta(z)$. Under this assumption, $F(q) \rightarrow 1$ and we get

$$V_{ext}(q) = \frac{e^2}{2\tilde{\kappa}\varepsilon_o q}. \tag{3.21}$$

In the random phase approximation, the screened response function is given by the Lindhard function [86], [88]:

$$\chi(q,\omega) = \sum_k \left[\frac{f(k) - f(k+q)}{\varepsilon(k+q) - \varepsilon(k) + (\hbar\omega - i\hbar\alpha)}\right] \tag{3.22}$$

where α accounts for the dissipative part of the carrier-carrier interaction [41]. Typically it has a small effect, and hence we shall neglect it in our analysis. Since the potential due to an ionized impurity atom does not vary with time, we only need to compute the screened response function in the static limit, i.e. $\omega \to 0$. Also Coulombic scattering is non-isotropic in nature and it tends to deflect carriers through small angles. Finally, $q = 2k\sin(\theta/2)$, and since θ is assumed to be small, it is reasonable to assume that $q \ll k$. With this assumption, we get the following pair of simplifications :

$$f(k) - f(k+q) \approx -q \cdot \frac{\partial f}{\partial k} = -q \cdot \frac{\partial f}{\partial \varepsilon} \cdot \frac{\partial \varepsilon}{\partial k} \tag{3.23}$$

$$\varepsilon(k+q) - \varepsilon(k) \approx q \cdot \frac{\partial \varepsilon}{\partial k} \tag{3.24}$$

With the help of equation (3.23) and (3.24), the expression for the screened response function in equation (3.22) simplifies to :

$$\chi(q) = \sum_k -\frac{\partial f}{\partial \varepsilon} \tag{3.25}$$

Assuming Maxwell-Boltzmann statistics, $f(\varepsilon) \sim e^{\varepsilon/kT}$ which implies $\partial f/\partial \varepsilon = f/kT$. Hence, χ(q) in equation (3.25) transforms to $\chi(q) = -\frac{1}{kT}\sum_k f(k)$. Since, $f(r, k)$ corresponds to the probability of finding an electron at **r** with momentum **k**, if we perform the summation over all **k**, we simply get the 2D electron density N_{inv} at point **r**, where **r** is a vector in the x-y plane of the inversion layer. Thus, the expression for the screened response function becomes :

$$\chi = -\frac{N_{inv}(\mathbf{r})}{kT} \tag{3.26}$$

Substituting for χ in the expression for the dielectric function in equation (3.18), and using the expression for V_{ext} from equation (3.21), we get for $\varepsilon(q)$ the following:

$$\varepsilon(q) = 1 + \frac{e^2}{2\tilde{\kappa}\varepsilon_o q} \frac{N_{inv}(\mathbf{r})}{kT} \tag{3.27}$$

If we define the inverse screening length q_d in the inversion layer as

$$q_d \equiv \frac{e^2 N_{inv}}{2\tilde{\kappa}\varepsilon_o kT} \tag{3.28}$$

then the dielectric function $\varepsilon(q)$ for a 2D electron gas can be rewritten as :

$$\varepsilon(q) = 1 + \frac{q_d}{q} \tag{3.29}$$

In contrast, the dielectric function for a 3D gas is given by $\varepsilon(q) = 1 + \left(q_d^{3D}/q\right)^2$.

Now that the dielectric function for the 2D electron gas has been computed, we proceed to compute the screened Coulombic potential in the inversion layer. Combining equations (3.17), (3.21), and (3.29), the expression for screened Coulombic scattering is given by :

$$V_{eff}(q) = \left(\frac{e^2}{2\tilde{\kappa}\varepsilon_o}\right) \frac{1}{q + q_d} \tag{3.30}$$

To obtain the transition rate for screened Coulombic scattering, we replace the unscreened Coulombic potential in equation (3.7) with $V_{eff}(q)$ given in equation (3.30) to obtain :

$$S(q) = \frac{2\pi}{\bar{h}}\left(\frac{e^2}{2\tilde{\kappa}\varepsilon_o(q+q_d)}\right)^2 N_{2D}\ \delta[\varepsilon(k') - \varepsilon(k)] \tag{3.31}$$

As in the case for unscreened Coulombic scattering, screened scattering is assumed to be predominantly due to a sheet of impurity atoms located near the interface.

Due to the elastic nature of Coulombic scattering, its scattering rate ought to be calculated according to equation (2.35). However, in trying to calculate the elastic scattering rate (i.e. $1/\tau_m$) we find that the resulting integral $\int \frac{(1-\cos\theta)}{[\sin(\theta/2) + q_d]^2} d\theta$ does not permit a closed-form solution. We instead find that such a solution exists for the isotropic scattering rate (also defined as the inverse of the single-particle relaxation time τ_s) as given in equation (2.27). While unscreened and weakly screened Coulombic potentials lead to non-isotropic scattering, moderately and strongly screened potentials result in isotropic scattering [15]. It has also been experimentally observed that in a silicon MOSFET, momentum relaxation and single-particle relaxation times are nearly equal [89], [90]. Hence, it is a reasonable approximation to calculate screened Coulombic mobility based on the single-particle relaxation time as opposed to the momentum relaxation time. The isotropic scattering rate, defined in equation (2.27), is given by :

$$\frac{1}{\tau_m} \approx \frac{1}{\tau_s} = \frac{N_{2D}}{(2\pi)^2}\frac{2\pi}{\bar{h}}\left(\frac{e^2}{2\tilde{\kappa}\varepsilon_o}\right)^2 \int \frac{1}{(q+q_d)^2}\ \delta[\varepsilon(k') - \varepsilon(k)]\, d\mathbf{k} \tag{3.32}$$

With $q = 2k\sin(\theta/2)$, $d\mathbf{k} = k\ dk\ d\theta$, and $dk = \left[m^*/\bar{h}^2 k\right] d\varepsilon$, equation (3.32) simplifies to :

$$\frac{1}{\tau_s} = \frac{e^4 N_{2D}}{32\pi\bar{h}(\tilde{\kappa}\varepsilon_o)^2}\ \frac{1}{\varepsilon}\int_o^{\pi/2} \frac{1}{[\sin\theta + q_d/(2k)]^2} d\theta \tag{3.33}$$

If we define $\alpha = q_d/2k$, and represent the integral in equation (3.33) by $F(\alpha)$, then $F(\alpha)$ is given by :

$$F(\alpha) = \frac{1}{\alpha\left[1-\alpha^2\right]} - \frac{\alpha}{\left[1-\alpha^2\right]^{3/2}} \cdot \log\left(\frac{\alpha^2+\alpha\left[1+\sqrt{1-\alpha^2}\right]}{\alpha^2+\alpha\left[1-\sqrt{1-\alpha^2}\right]}\right) \qquad (3.34)$$

The energy dependence of the scattering rate in equation (3.33) is equal to unity. Thus, according to equation (2.54), mobility due to screened Coulombic scattering is given by :

$$\mu_{screened} = \frac{80\pi\hbar(\tilde{\kappa}\varepsilon_o)^2(kT)}{e^3 m^* N_{2D} F(\alpha)} \qquad (3.35)$$

where $F(\alpha)$ is given by equation (3.34). α is evaluated at $\varepsilon = (s + 3/2)kT$ [15], and hence we get:

$$\alpha = \frac{e^2 \hbar N_{inv}}{4(\tilde{\kappa}\varepsilon_o)\sqrt{5m^*}(kT)^{3/2}} \qquad (3.36)$$

At room temperature, $\alpha \sim N_{inv}/1\times10^{13}$, and hence for N_{inv} varying between 1×10^{11} and $1\times10^{12}\ \mathrm{cm}^{-2}$, α is 0.1 or smaller. From equation (3.34), we see that for small α, $F(\alpha) \propto 1/\alpha$. Thus, over this range of N_{inv}, $\mu_{screened} \propto N_{inv}$.

3.3 Comparison with Experimental data

The first experimental investigation of Coulombic scattering due to ionized impurity atoms in the channel was reported by Takagi *et. al.* [9], [10]. However, Takagi's extraction technique, based on the split C-V method [75], restricted him to study only the screened aspect of Coulombic scattering. Since Takagi's first results on Coulombic scattering, other works have appeared in the literature [78], [80] that support the original findings. Moreover, improved techniques have been proposed for extracting Coulombic scattering [91], [92].

In an attempt to model screened Coulombic scattering in MOS inversion layers, consistent with 2D device simulation, researchers [80] have examined existing models in the literature that were originally formulated in closed form. The premier analytical model based on a first-principles calculation was first proposed by Brooks and Herring [13] who had treated screened Coulombic scattering in a three dimensional electron gas. However, it was noted by Shin *et. al.* [80] that the Brooks-Herring model did not provide good agreement with Takagi's [9] experimental data for 2D screened Coulombic scattering. Shin's solution to this problem was to introduce sufficient number of calibrating parameters to fit the model and data. In doing so however, there still exists a fundamental deficiency in Shin's model since it was not obtained from a first-principles calculation of 2D Coulombic scattering. The first principles calculation presented in Section 3.2 is an attempt to more accurately model 2D Coulombic scattering, and in doing so, fewer calibrating parameters are needed to fit the model with experimental data.

As a demonstration of the success of the new modeling effort, Fig. 3.2 presents a comparison between the Brooks-Herring model, the new 2D model for screened Coulombic scattering (specified by equations (3.34)-(3.36)), and experimental data[1] by Takagi *et. al.* [9]. It should be emphasized that in presenting the comparison in Fig. 3.2, no calibrating parameters have been introduced in either the Brooks-Herring model or the new 2D model. For the Brooks-Herring model, one can observe that both the magnitude of mobility and its dependence on N_{inv} do not agree with experimental data. While the new model does not predict the magnitude of mobility correctly, it does capture the N_{inv} dependence with great accuracy.

From Fig. 3.2, we note that Brooks-Herring model exhibits a super-linear dependence on N_{inv} whereas the new 2D model exhibits a linear dependence. This behavior, which results from fact that screening in 3D is stronger than in 2D [85], can be explained as follows. Imagine a point charge (whose electric field lines emanate in all three dimensions) which is immersed in an electron gas whose movement is confined to a plane. This 2D electron gas would be able to effectively screen *only* those field lines that lie within its plane, whereas the field lines that are perpendicular to the plane of the electron gas would be poorly screened. On the other hand, an electron gas that can freely move in all three dimensions would be able to screen field lines in all three dimensions. As a result, 3D electrons screen Coulomb potentials better than 2D electrons.

Due to the nature of first-principles calculations, it is not expected that the new 2D

1. extraction of screened Coulombic scattering from experimental data is discussed in Section 3.5.

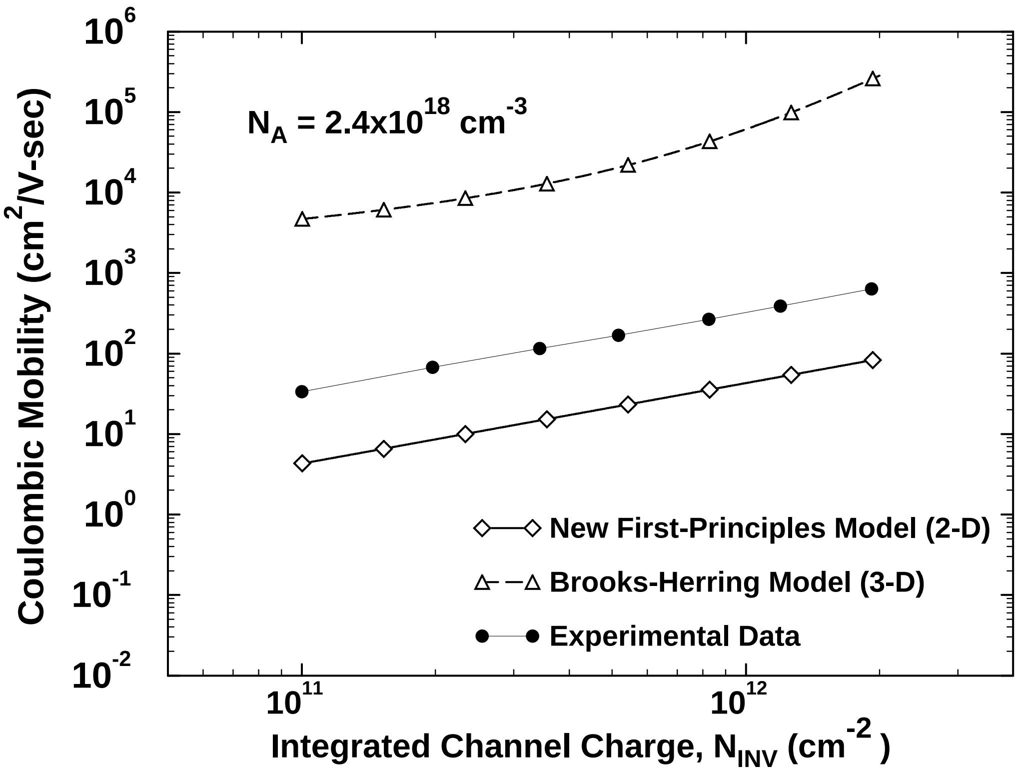

Figure 3.2 Comparison between Brooks-Herring model, the new 2D model, and Takagi *et. al.*'s experimental data [9]. Mobility is higher in 3D compared to 2D because of stronger screening [85], which results from the fact that field lines emanating in 3D can never be completely screened in 2D.

model would correctly predict both the magnitude as well as the screening dependence, since a series of simplifying assumptions have to be made to render the solution possible. In light of this fact, the screening dependence correctly predicted by the new model when the 3D model could not certainly implies that the inversion layer should be treated as a 2D gas. The major benefit of this new model, as we have already stated, is that only one calibrating parameter in the form of a pre-factor is required to achieve complete agreement with the experimental data. This, however, can not be said for the Brook-Herrings model since its screening dependence also needs to be "corrected" in order to match it with experimental data.

The calibrated model $\tilde{\mu}_{screened}$ is given by $k \cdot \mu_{screened}$, where k is the calibrating parameter and $\mu_{screened}$ is given by equation (3.35). Broad applicability of the new calibrated model is demonstrated in Fig. 3.3 which exhibits excellent agreement between the new model and experimental data over a wide range of channel doping values. It may

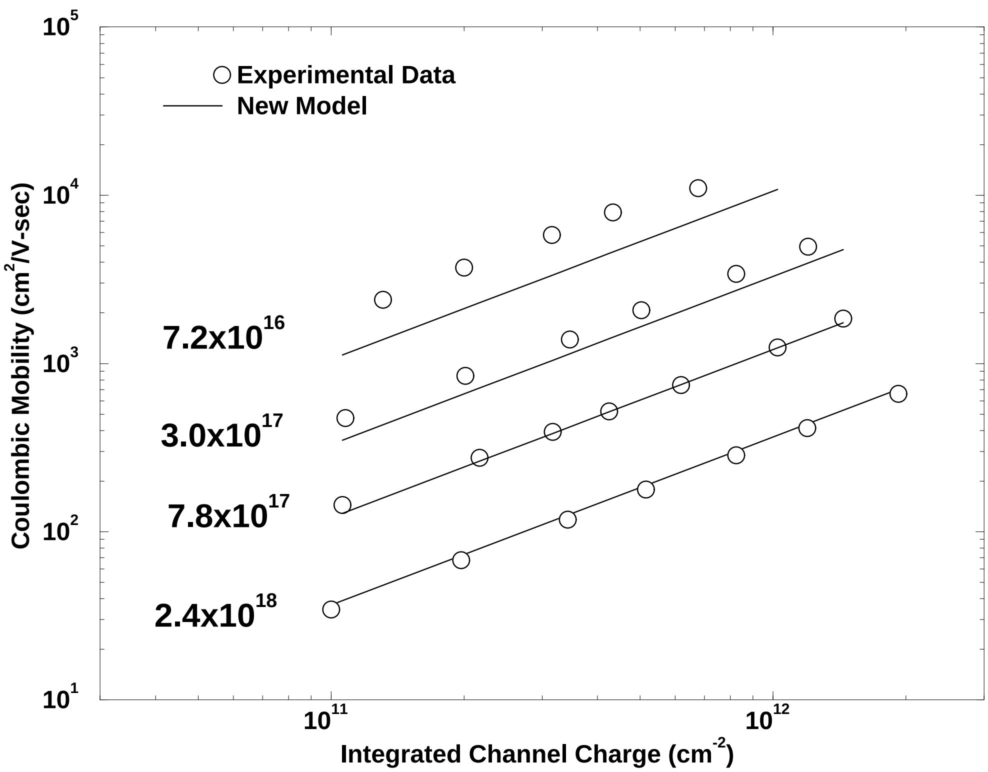

Figure 3.3 Broad applicability of the new model, fitted with one calibrating parameter, is demonstrated by comparing it with experimental data over a wide range of channel doping levels and electron densities.

be noted from Fig. 3.3 that the fit for the lowest doping case is not as good as for the higher doped cases. This has to do with the fact that the model for screened Coulombic scattering was derived for a strictly two-dimensional gas. For the higher doped cases, the potential well in the inversion layer is steep, leading to strong quantization. Hence, the assumption of two-dimensionality holds quite well for the higher doped cases. For the lower doped cases, the potential well is fairly shallow, and quantization is weak. Thus, a strictly 2D model for the electron gas is a poor approximation for low doped substrates.

3.4 Substrate Bias Dependence

One aspect of Coulombic scattering that distinguishes it from phonon and surface roughness scattering in the inversion layer is that Coulomb scattering is a function of N_{inv} whereas the latter two are functions of the effective electric field E_{eff} which is defined as [43]:

$$E_{eff} = \frac{1}{\varepsilon_{si}}\left[\frac{1}{2}Q_{inv} + Q_{depl}\right] \tag{3.37}$$

In order to express E_{eff} in terms of terminal voltages, use of the following relations is made ([93]) : $Q_{inv} = C_{ox}(V_{GS} - V_T)$, $V_T = V_{TO} + Q_{depl}/C_{ox}$, and $Q_{depl} = \gamma\, C_{ox}\sqrt{2\phi_p + |V_{SB}|}$, where $\gamma = \sqrt{2\varepsilon_{si} q N_{sub}}/C_{ox}$. Thus, E_{eff} is given by:

$$E_{eff} = \frac{C_{ox}}{2\varepsilon_{si}}\left[(V_{GS} - V_{TO}) + \gamma\sqrt{2\phi_p + |V_{SB}|}\right] \tag{3.38}$$

Both phonon and surface-roughness mobility decrease with increasing E_{eff} [43]. Thus, according to equation (3.38), increasing either V_{GS} or V_{SB} would increase E_{eff}, which would cause phonon and surface roughness mobilities to decrease. If V_{GS} and V_{SB} are both increased such that Q_{inv} is held constant (i.e. screening strength is not changed), then although phonon and surface roughness mobilities would decrease, we would expect Coulombic mobility to remain unchanged based on the model derived in Section 3.2.2.

To test our hypothesis, we experimentally investigated the effect of substrate bias on screened Coulombic mobility. Results shown in Fig. 3.4 indicate that Coulombic mobility is a very weak function of substrate bias, thus confirming our hypothesis as well as the validity of the new model.

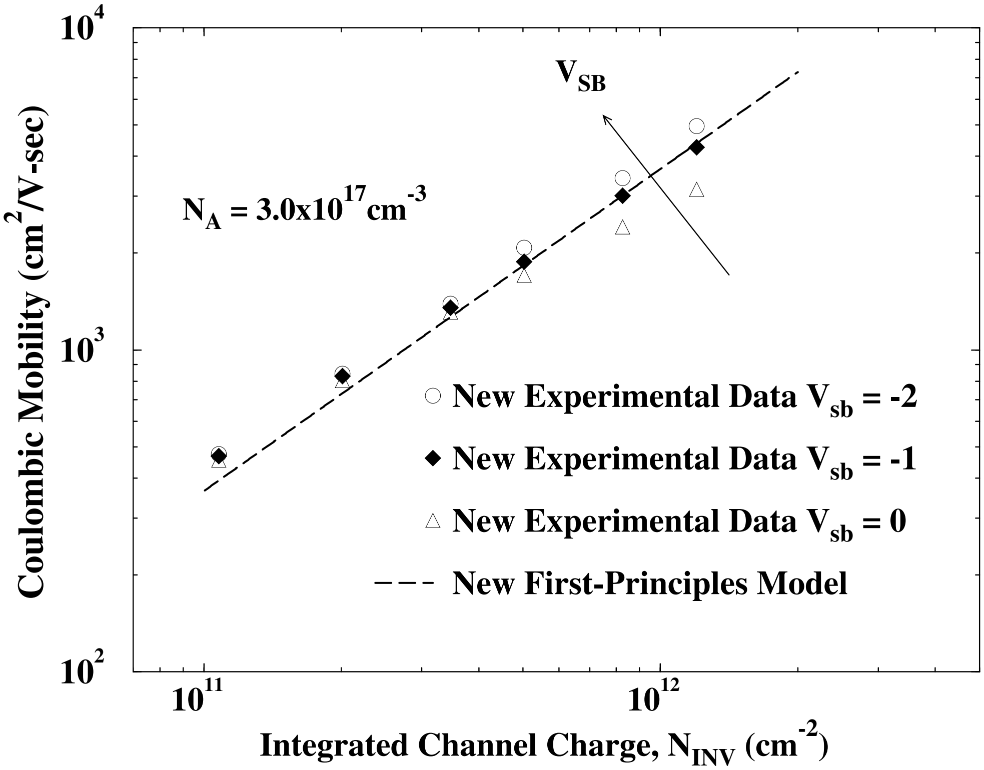

Figure 3.4 Coulombic mobility is shown to be a weak function of substrate bias, demonstrating that electron density and channel charge are the dominant parameters affecting Coulombic scattering.

3.5 Systematic Extraction Technique

The technique used by Takagi *et. al.* [9] and other researchers [91] for extracting Coulombic mobility in the inversion-layer is based on the split C-V method [75]. For a MOSFET biased in the linear region, the expression for drain current I_{DS} is given by (see Ref. [93]) :

$$I_{DS} = \frac{W}{L}\mu_{eff}\int_{o}^{V_{DS}} Q_{inv}\,[\varphi(x)]\,d\varphi \tag{3.39}$$

where φ is the quasi-fermi potential, Q_{inv} is the inversion charge per unit of channel area, W and L are the channel width and length respectively, and V_{DS} is the drain voltage. In the limit of $V_{DS} \rightarrow 0$, Q_{inv} can be considered as a constant, and equation (3.39) reduces to:

$$I_{DS} = W\mu_{eff} Q_{inv}\frac{V_{DS}}{L} \tag{3.40}$$

Thus, if measurements are performed at a vanishingly small V_{DS} (around 10 to 30 mV in practice), effective mobility can be computed from equation (3.40) as

$$\mu_{eff} = \frac{I_{DS}}{WQ_{inv}(V_{DS}/L)} \tag{3.41}$$

Inversion charge per unit area can be mapped as a function of gate voltage by noting that

$$Q_{inv}(V_{gs}) = \int_{-\infty}^{V_{GS}} \left[dQ_{inv}/d\tilde{V}_{GS}\right] d\tilde{V}_{GS} \tag{3.42}$$

where dQ_{inv}/dV_{GS} is simply the gate-to-channel capacitance which can be measured using the “split” C-V technique [94] performed at intermediate frequencies to suppress the response of interface states and the effect of channel resistance [95]. Resolution of the split C-V technique is severely degraded if the carrier concentration in the inversion layer is small [96] (i.e. in weak inversion which corresponds to the subthreshold region of operation). Since equation (3.42) gives accurate results in strong inversion, the C-V technique can be successfully applied to extract screened Coulombic mobility from equation (3.41). However, the split C-V technique can not be extended to extract unscreened Coulombic mobility from equation (3.41) since that requires measurement of Q_{inv} in subthreshold which can not be accurately performed by the split C-V technique.

Since Q_{inv} can not be accurately measured in subthreshold, we instead work with I_{DS} which *can* be accurately measured in subthreshold. A new and systematic technique is proposed that involves classical and quantum simulations, and requires I-V and C-V data from measurements. We see from equation (3.40), which is applicable in subthreshold, that an accurate simulation of I_{DS} would require correctly calculating Q_{inv} and μ_{eff}. The simulations are performed using PISCES [54], a two-dimensional device simulator that solves the drift-diffusion equation. The following pieces of information must be supplied to PISCES in order for it to accurately calculate Q_{inv} :

(1) Doping profile:

The devices that are being simulated have a uniform doping profile [9]. A high degree of uniformity was achieved by annealing the samples at 1190°C for 60 minutes. Background doping was determined from the C-V capacitance measurements in the high-frequency[1] (100 *kHz*) [10] regime using the maximum-minimum capacitance method [109]. Based on comparison with process simulation results, the accuracy of this extraction was found to be limited to 10% [96].

(2) Oxide thickness:

The oxide thickness was determined from high frequency C-V measurements in the accumulation region. The accuracy of this measurement is typically within 2% [109].

(3) Interfacial and fixed oxide charge:

Interfacial and fixed oxide charges were determined by comparing theoretical and measured high-frequency C-V curves. Accuracy of the theoretical curves is limited to the accuracy with which oxide thickness and substrate doping is known. Since, shifts are measured between flatband and threshold voltage, based on the expression for capacitance near flatband [93], the accuracy of this calculation is around 12%.

(4) Quantum corrections:

Since PISCES does not solve the Schrodinger's equation for electrons in the inversion layer, we need to consider two corrections that arise from the quantization of the electron gas. The first effect of quantization is the creation of energy sub-bands in the inversion layer [8]. Classically, electrons would start occupying the conduction band at $\varepsilon = 0$. However, quantum mechanically, the lowest energy level in the conduction band that they can occupy corresponds to the first sub-band at $\varepsilon = \varepsilon_o$. This energy separation ε_o appears as

1. High frequency suppresses the response of interface states [109].

an effective increase in band-gap which tends to reduce Q_{inv}. The other effect of quantization is the emergence of wavefunctions. Classically, electrons would distribute themselves according to Maxwell-Boltzmann statistics, in which case the electron concentration would be maximum at the interface and decrease monotonically away from the interface. Quantum mechanically, electron concentration peaks where the wavefunction is a maximum which occurs at a certain distance z_m below the interface. The effective oxide thickness ($t_{ox} + z_m$) is larger than the physical oxide thickness t_{ox}, which also tends to reduce Q_{inv}. The net effect of both the quantum corrections can be determined by comparing the Q_{inv}-V_{gs} curves of a self-consistent Schrodinger-Poisson solution with a classical solution from PISCES. The shift due to the quantum mechanical correction approximately follows $T_{ox}\sqrt{N_A}$ [110]. Hence, the accuracy of this calculation is limited to about 5%.

Calculation of drain current by PISCES, using the four pieces of information mentioned above, would be limited to an accuracy of about 30%.

To correctly calculate mobility in *subthreshold*, the model in PISCES should incorporate the following terms:

(1) Phonon scattering:

Mobility due to phonon scattering is extracted using the same methodology [43] as for screened Coulombic scattering. When plotted as effective mobility versus effective field E_{eff}, phonon scattering yields what is known as the universal mobility curve. The concept of the universal mobility curve (UMC) was first proposed by Sabnis and Clemens [43], and since then other researchers [9], [33], [77], have successfully reproduced the UMC. While phonon mobility is extracted in strong inversion, its model can be extended to the subthreshold region by virtue of the UMC, and is explained as follows. From equation (3.38), for the same V_{GS} - V_{TO} (which determines the degree to which the channel is inverted), a lightly doped substrate results in a smaller value of E_{eff} compared to a heavily doped substrate. It is an experimentally observed property of the UMC that both the doping levels would overlap on the UMC [43], with the curve generated by the lightly doped substrate starting at a smaller value of E_{eff} compared to the heavily doped substrate. The UMC is applicable to phonon mobility regardless of substrate doping [43], since an E_{eff} value corresponding to subthreshold for a certain doping would correspond to strong inversion for a lighter doping. Hence, the UMC can be used to determine phonon mobility in subthreshold. Implicit in this argument is that the screening of the phonon deformation potential by the electron gas is considered to be negligible [106].

(2) Surface roughness scattering:

Mobility due to surface roughness scattering is extracted using the same methodology as for screened Coulombic scattering [10]. Surface roughness scattering will follow the UMC provided the interfacial properties of the $Si\text{-}SiO_2$ system remain invariant. This for instance would be true for MOSFETs whose gate oxide is grown under similar conditions. Based on the same reasoning as for phonon scattering, surface roughness scattering can also be determined from the UMC in subthreshold.

(3) Coulombic scattering

Unscreened mobility is the last piece of information that would be needed to accurately simulate I_{DS} in subthreshold. Unlike phonon and surface roughness scattering, Coulombic mobility in strong inversion is very different from that in weak inversion; hence Coulombic scattering does not follow the UMC [9].

The new extraction technique for unscreened Coulombic mobility is based on the following observation: for the simulated I_{DS} to exactly match the measured I_{DS} in subthreshold, the device simulator would have to correctly calculate Q_{inv} and μ_{eff} in this region. Assume that the four pieces of information required to accurately calculate Q_{inv} are available. On the other hand, the only available mobility model is the one that is based on the UMC (see Section 4.6), which incorporates phonon and surface roughness scattering. Due to the lack of a term for unscreened Coulombic scattering, calculation of μ_{eff} in subthreshold is inaccurate. Any discrepancy between simulated and measured I_{DS} in subthreshold is now attributed to unscreened Coulombic scattering. The extraction of unscreened Coulombic scattering from this discrepancy is described below.

The MOSFET devices used in this study are 200µm long and 100µm wide, each with a gate oxide thickness of 250Å, and a uniform substrate doping that lies between $1x10^{16}$ and $1x10^{18}$ cm^{-3}. For each substrate doping level, the following five steps are performed to arrive at a value for unscreened mobility and its corresponding effective doping level:

(1) *For the device under test, the interfacial and fixed oxide charges are determined from high-frequency C-V measurements, and the values supplied to PISCES. Since interfacial and oxide charge is typically positive, its electrostatic effect on* Q_{inv} *is to increase it. This results in a rigid left shift of the* I_{DS}-V_{GS} *curve in subthreshold. The accuracy of this correction is limited to 12%. It should be mentioned that the value extracted for interfacial and oxide charges also includes the difference in workfunctions.*

(2) *For that particular substrate doping level, self-consistent 1-D Schrodinger-Poisson simulations are performed to generate an* Q_{inv}-V_{GS} *curve which is then compared with a corresponding classical curve generated by PISCES. The shift between the two curves is taken to be the quantum correction, which is supplied to PISCES in the form of a rigid* V_T *shift. The shift in the* I_{DS}-V_{GS} *curve is to the right since quantum corrections appear as an effective increase in bandgap. The accuracy of this calculation is limited to around 5%.*

After steps 1 and 2 have been performed, the simulated I_{DS} curve, accurate to within 30%, is compared with the corresponding experimental I_{DS} curve, an illustration of which is shown in Fig. 3.5. We note from Fig. 3.5 that the simulation results predict I_{DS} that is higher than the measured values. Since we have accounted for all the factors affecting the calculation of Q_{inv}, this discrepancy is attributed to an incorrect calculation of mobility by PISCES. The mobility model used in PISCES simulations has terms for phonon and surface roughness scattering. Thus, it is the lack of a term for unscreened Coulombic scattering that is the cause of this discrepancy. Since $Q_{SIM} = Q_{EXP}$, from equation (3.40), the ratio of drain currents is simply the ratio of mobilities:

$$\frac{I_{SIM}}{I_{EXP}} = \frac{\mu_{UMC} Q_{SIM} V_{DS}/L}{\mu_{EXP} Q_{EXP} V_{DS}/L} = \frac{\mu_{UMC}}{\mu_{EXP}} \tag{3.43}$$

where I_{SIM} and I_{EXP} are simulated and experimental I_{DS} respectively, μ_{UMC} is the mobility model based on the universal mobility curve, μ_{EXP} is the actual value for

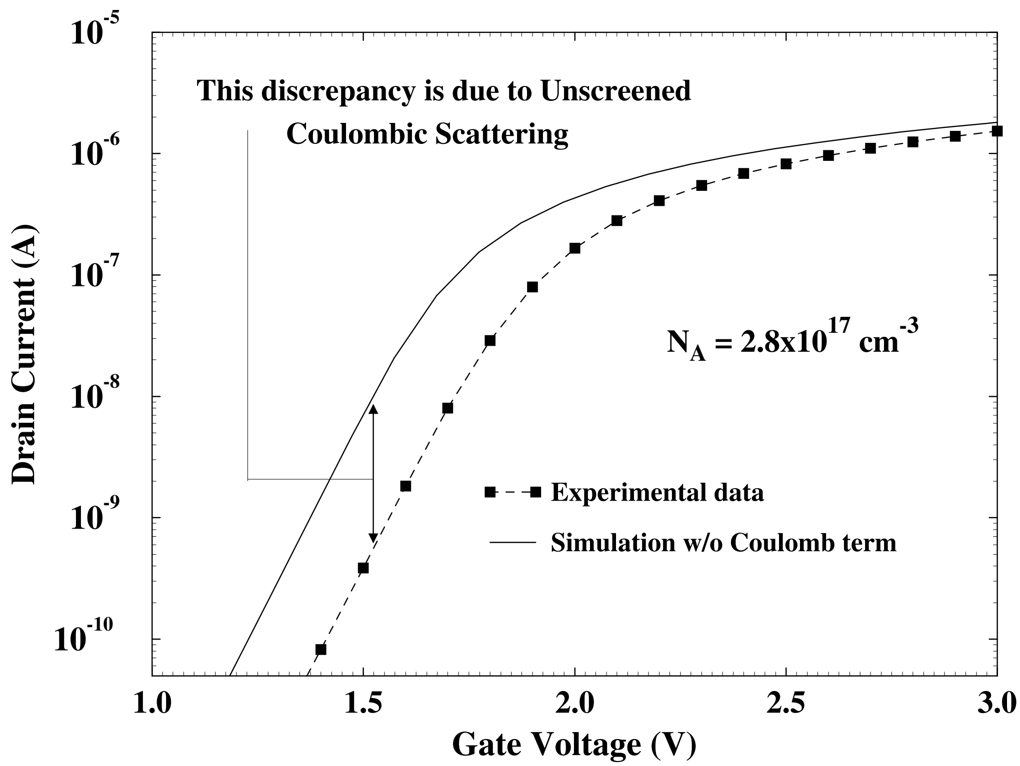

Figure 3.5 Comparison between simulated and experimental I_{DS} in subthreshold. Lack of the unscreened Coulomb term accounts for the discrepancy.

mobility in subthreshold, and Q_{SIM} and Q_{EXP} are simulated and experimental Q_{inv} respectively. For the three doping cases considered in this work, the ratio I_{SIM} / I_{EXP} took on values between 10 and 20. The 30% error in I_{SIM} is clearly much less than the discrepancy due to unscreened Coulombic scattering, thus establishing the accuracy of the proposed extraction technique.

In the third step, μ_{EXP} is obtained from equation (3.43) as:

(3) Calculation of μ_{EXP} *:*

$$\mu_{EXP} = \frac{I_{EXP}}{I_{SIM}} \mu_{UMC} \tag{3.44}$$

If we assume that the various scattering mechanisms can be summed up using Matthiessen's rule [14], then the unscreened Coulombic mobility μ_{UN} is calculated as:

(4) Calculation of μ_{UN} *:*

$$\mu_{UN} = \frac{\mu_{UMC} - \mu_{EXP}}{\mu_{UMC}\mu_{EXP}} \tag{3.45}$$

Thus, for each channel doping level, we are able to extract a value for unscreened Coulombic mobility by performing steps 1 through 4. In the final step, we need to calculate the effective substrate doping level associated with this mobility value.

It is important to note that besides affecting the calculation of Q_{inv}, interfacial and oxide charges also affect the calculation of Coulombic mobility. The total charge in two-dimensions that would scatter inversion layer electrons is:

$$N_{2D} = N_{if} + N_f + N_A \cdot \langle Z_{inv} \rangle \tag{3.46}$$

where N_{if} is the interfacial charge, N_f is the oxide charge, N_A is the acceptor charge in the channel and $\langle Z_{inv} \rangle$ is the average thickness of the inversion layer in subthreshold. This thickness is calculated from a self-consistent 1-D solution of the Schrodinger-Poisson's equation. Thus, the equivalent charge in the substrate $\langle N_A \rangle_{eff}$ that would scatter the electrons is calculated as:

(5) Calculation of effective charge in substrate:

$$\langle N_A \rangle_{eff} \equiv \frac{N_{2D}}{\langle Z_{inv} \rangle} = \frac{N_{if} + N_f}{\langle Z_{inv} \rangle} + N_A \tag{3.47}$$

As can be seen from equation (3.47), the effect of interfacial and oxide charges is to increase the "effective" channel doping density seen by the inversion layer electrons.

The result of applying steps 1 through 5 is shown in Fig. 3.6 which also presents the comparison between extracted data, the new 2D model for unscreened Coulombic scattering, and the 3D model of Conwell and Weisskopf [12]. As can be seen from Fig. 3.6, the new 2D model exhibits much better agreement than the 3D model, suggesting that even in subthreshold, the electron gas behaves as a two-dimensional gas. This has to do with the fact that at high doping levels, such as those shown in Fig. 3.6, the potential wells are still quite steep in subthreshold, leading to significant quantization of the electron gas.

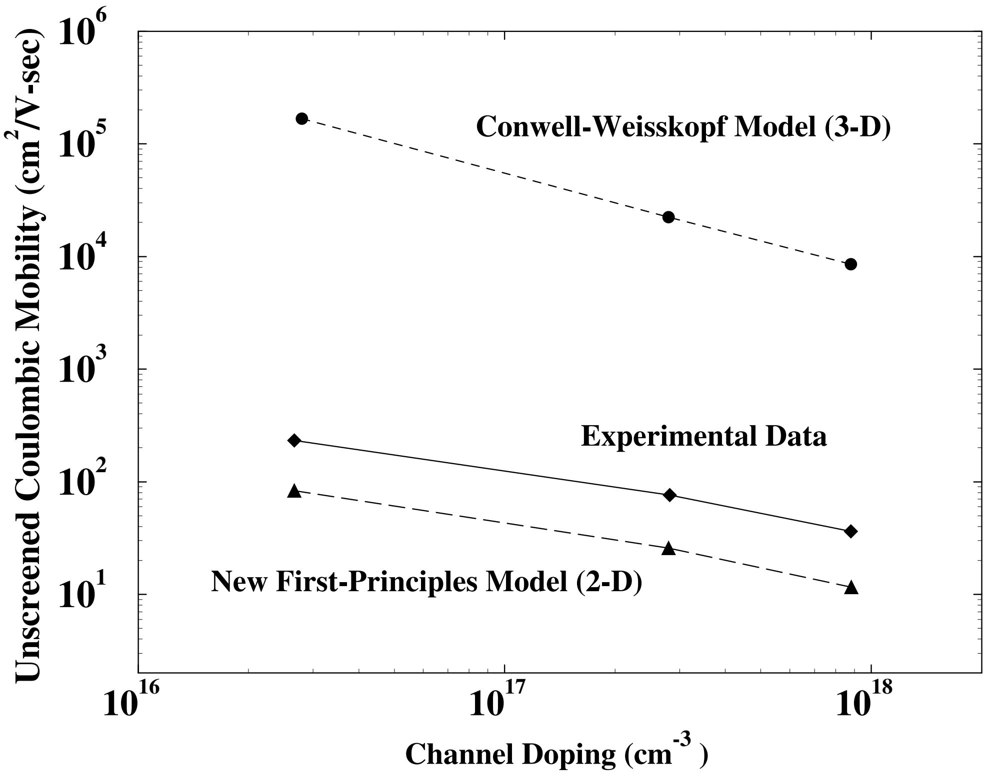

Figure 3.6 Comparison between extracted experimental data, new 2D model for unscreened Coulombic scattering, and 3D model due to Conwell and Weisskopf.

3.6 Impact of Coulombic scattering on V_T

Threshold voltage, V_T, is a very important design parameter for digital MOS applications since it represents the trade-off between I_{off}, the off-state leakage, and I_{on}, the current drive of the MOSFET. Aggressive design and optimization of submicron MOSFETs would require an accurate prediction of V_T.

Consider the design of MOSFETs for low-power applications. One method for reducing power dissipation, which is proportional to V_{dd}^2, is to scale V_{dd}. However, reduction of V_{dd} causes I_{on} to decrease, which negatively impacts the performance of the system. In an effort to improve the performance, the design of low-threshold devices has been suggested [84], [4]. While the I_{on} of such devices would increase, so would I_{off} which would result in increased standby power dissipation. Thus, for devices that are to operate at low V_{dd}, optimization of V_T is required to maximize performance and minimize standby power dissipation. If deep submicron MOSFETs are to be designed for low-power applications using 2D device simulation tools, it is essential that the simulator be able to accurately calculate the V_T of such devices which are doped heavily to suppress punchthrough and DIBL effects.

Figure 3.7 presents the V_T comparison between experimental data and simulation results obtained without a model for unscreened Coulombic scattering. The devices used in this study have the same oxide thickness (250Å) but different channel doping levels. Thus, as the channel doping is increased, the absolute value of threshold voltage also increases. In practice, MOSFETs with heavily doped channels will have thinner oxides (less than 250Å), as mandated by the scaling rules to keep the V_T at a reasonable value.

What is important to note, however, is that the discrepancy between predicted and measured V_T values increases as the channel doping goes up. This is because there is increased Coulombic scattering at higher channel doping levels, and hence the error is expected to be larger. Therefore, it becomes even more important to include a model for Coulombic scattering when designing MOSFETs with heavily doped channels. For instance, 0.1μm MOSFETs are expected to have channel doping levels around $1\text{x}10^{18}$ cm^{-3} and would be designed to operate at a V_{dd} of 1.0 to 1.5V [6]. Thus, a mobility model containing Coulombic scattering would be an important aid in technology scaling and optimization.

3.7 Conclusion

In this chapter, a first-principles analysis of two dimensional Coulombic scattering was presented. Unscreened Coulombic scattering was treated first, which is the scattering of electrons by a bare Coulombic potential. This type of scattering dominates in weak

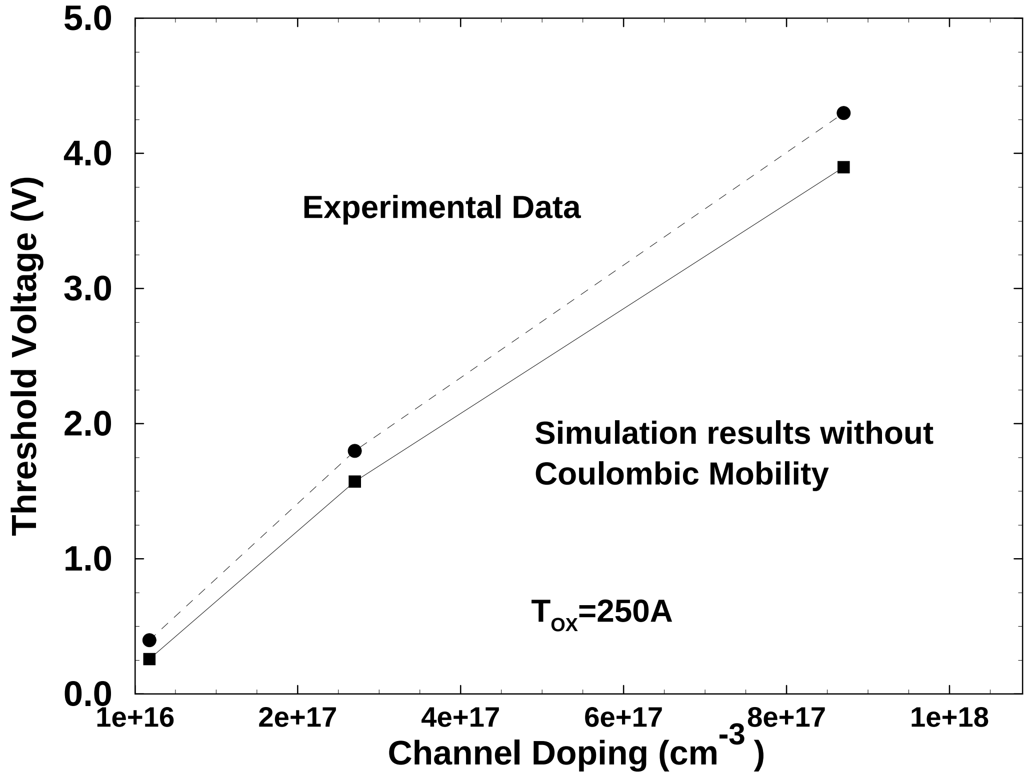

Figure 3.7 Comparison between experimental data and simulation results obtained without a model for unscreened Coulombic scattering.

inversion where there are too few carriers to screen the Coulomb potential. To keep the analysis tractable, the following assumptions were made: (a) the electron gas was treated as being strictly two dimensional (i.e. the envelope wavefunction was taken to be a delta function), and (b) the impurity atoms were assumed to be distributed as a sheet of charge near the interface. The first assumption holds if there is strong quantization (i.e. the deBroglie wavelength of electrons is larger than the confining potential). The second assumption holds in deep submicron MOSFETs that tend to have a large amount of charge implanted near the interface to suppress DIBL and punchthrough effects.

Screened Coulombic scattering was treated next. The longitudinal dielectric function for the electron gas was calculated in the random phase approximation, which led to an expression for the screened Coulomb potential. In addition to the assumptions made for unscreened scattering, it was further assumed that for strongly screened scattering, the single-particle relaxation time is approximately equal to the momentum relaxation time. This assumption permitted a closed-form solution to be calculated for screened Coulombic mobility. On comparison with experimental data, it was demonstrated that the new 2D model for screened Coulombic scattering accurately captures the screening dependence whereas the 3D model due to Brooks-Herring fails to do so. It was also established that screened Coulombic mobility is a strong function of channel charge and not of the effective electric field. This behavior is in sharp contrast with phonon and surface roughness scattering.

Since no known technique exists for extracting unscreened Coulombic scattering, a new and systematic technique was presented that involves quantum and classical simulations and requires the use of C-V and I-V data. Comparison of the extracted data with models showed that the new 2D model for unscreened Coulombic scattering gives better agreement with experimental data than the 3D model based on the formulation of Conwell and Weisskopf.

Finally, the importance of modeling Coulombic scattering in MOS inversion layers was established by demonstrating its impact on critical design parameters such as threshold voltage and off-state leakage current. It was noted that a mobility model containing Coulombic scattering would be an important aid in technology scaling and optimization.

Chapter 4

Numerical Modeling of the Generalized Mobility curve

4.1 Introduction

To be able to better predict the I-V characteristics of modern scaled MOSFETs, accurate mobility models are required which incorporate all of the basic scattering mechanisms operating in the inversion layer. At least three different scattering mechanisms have been identified that affect carrier mobility in the inversion layer. These include phonon scattering, Coulomb scattering, and surface roughness scattering [72]. At room temperature, Coulomb scattering is only important if there are a large number of charge centers present which can arise from either interfacial charge or channel dopants. Both phonon scattering and surface roughness scattering are important at room temperature, with surface roughness being especially important at high transverse electric fields. Therefore, in long channel MOSFETs with moderate to low channel doping levels, inversion-layer mobility is primarily limited by phonon scattering and surface roughness scattering.

There are two kinds of interactions possible between electrons and phonons: elastic and inelastic scattering. In elastic scattering, the energy of the electron after collision with the phonon is relatively unchanged, and this type of interaction dominates when the electrons are not very energetic. In contrast, inelastic scattering involves energy exchange between the electron and phonon systems, and the probability of this interaction increases as the energy of the carriers increase.

In the ohmic regime, the relationship between carrier velocity v and longitudinal electric field E is linear. In this regime, the applied fields are sufficiently low such that the electron gas is always in thermodynamic equilibrium with the lattice, i.e. the temperature of the electron gas is approximately equal to the lattice temperature. Thus, in the ohmic regime, phonon scattering is predominantly elastic. However, as the magnitude of the applied field increases, the electron gas is able to gain more energy from the field and "heat" itself. The resulting hot carriers have a much higher probability of engaging in inelastic collisions. In this regime, the relationship between velocity and applied field is no longer linear. In the discussion that follows, we shall be concerned exclusively with aspects of low-field transport in which $v \propto E$. The constant of proportionality is termed as mobility μ, and it is a measure of how well the carriers respond to a driving field E.

It is well known that low field mobility in a *long* channel MOSFET follows the universal mobility curve [9], [33], [43], a concept that was first introduced by Sabnis and Clemens [43]. The principal features of the universal mobility curve (UMC) are that it is invariant to changes in (i) oxide thickness, (ii) channel doping, and (iii) substrate bias. The universality of mobility indicates that it is a property associated with the Si/SiO_2 system and not a parameter sensitive to nominal process variations [43]. It was shown by Lee *et. al.* [53] that the universal mobility curve can be explained on the basis of phonon scattering and surface roughness scattering in the inversion layer.

In *short* channel MOSFETs, which tend to have high channel doping levels to suppress punchthrough and drain-induced-barrier-lowering effects, another scattering mechanism has become important, namely Coulombic scattering due to ionized channel dopants. While phonon scattering and surface roughness scattering lead to the universal mobility curve, it was experimentally observed by Takagi *et. al.* [9] that in the presence of strong Coulombic scattering, marked deviations from the universal mobility curve are obtained. The resulting curve is termed as the *generalized mobility curve* or the GMC.

In the previous chapter, we presented a theoretical analysis for two dimensional Coulombic scattering in the inversion layer. The model presented there (see equations (3.11), (3.35), and (3.36)) was cast in terms of non-local variables such as N_{inv} and N_{2D}, the electron and impurity charge density per unit of channel area respectively. While physically based models may originally appear in non-local form, for implementation in device simulators based on the finite-volume method [55] such as PISCES [54], it is highly desirable to reformulate the model in terms of local variables such as n and N, the electron and impurity charge density per unit volume respectively.

Moment-based device simulators [55] solve a set of coupled non-linear partial differential equations by discretizing them in space and time domain[1]. These discretized equations are then solved by either linearizing or decoupling them [55], [56]. In the discretization process, the continuum of space and time is broken into a set of discrete points, which are typically called nodes. The goal then is to calculate the variables of interest at these nodes at a given time. Thus, within a device simulator, a *local* computation is one which involves information from the nearest neighboring nodes only. The implication is that during the linearization step, the less the coupling among the various nodes, the easier it is to solve the discretized set of algebraic equations. On the other hand, a *non local* computation involves information from nodes that can be far apart. This tends to increase the degree of *coupling* among the nodes in the device, whose primary effect is to increase the computation time.

There are other attributes to implementing models in a local form. Parallel device simulators that are based on the domain decomposition scheme [57] see a significant decrease in computation speedup if non-local models are used. Moreover, local models allow for the simulation of complex, non-planar 2-D and 3-D structures which is not possible if a non-local formulation is used since a non-local model *assumes* a planar structure [30].

In this chapter we present a *local* model for low-field mobility that includes phonon, surface-roughness, and Coulombic scattering. A local model should satisfy the properties attributed to the non-local generalized mobility curve (GMC), since the general form of the GMC lends itself to physical interpretation [53]. We define the GMC as the sum of a universal part (the Universal Mobility Curve (UMC) [43]) and a non-universal part [9]. The new model has been implemented in PISCES [54], a 2-D device simulator, and it indeed reproduces the GMC over a wide range of parameters. Good agreement of the new model with several sets of experimental data is shown.

The organization of this chapter is as follows. First, in Section 4.2, a physically correct scheme is presented for combining the various scattering mechanisms. In Section 4.3, phonon scattering in MOSFETs is discussed: Section 4.3.2 presents the theoretical

1. The differential equations are converted into algebraic equations through the discretization procedure.

basis for 2D phonon scattering; Section 4.3.3 outlines the extraction of a 2D semi-empirical model from the first-principles model; and Section 4.3.4 presents an empirical model for 3D phonon scattering.

Surface roughness scattering is discussed next in Section 4.4: theoretical treatment is considered in Section 4.4.1, and its semi-empirical formulation presented in Section 4.4.2.

Section 4.5 is concerned with Coulombic scattering. Since, a first-principles model for 2D Coulombic scattering was presented in Chapter 3, Section 4.5.1 discusses the extraction of the semi-empirical model. Section 4.5.2 presents an empirical model for 3D Coulombic scattering.

The universal mobility curve is modeled in Section 4.6 by combining the semi-empirical models for phonon and surface-roughness scattering. The parameters appearing in phonon and surface-roughness terms are calibrated to reproduce all the properties of the UMC.

Finally, in Section 4.7, the generalized mobility curve is modeled by including the term for Coulombic scattering in the model for the UMC. The resulting semi-empirical model is shown to accurately reproduce the GMC over a wide range of biases and channel doping levels.

4.2 Formulation of the Model

Most formulations of inversion-layer mobility start with the following functional form [29], [30], [31], [32]:

$$\frac{1}{\mu_{total}} = \frac{1}{\mu_{surface}} + \frac{1}{\mu_{bulk}} \tag{4.1}$$

The surface term models the 2D scattering mechanisms, whereas the bulk term models the 3D effects. Matthiessen's rule summation is strictly correct when the scattering mechanisms that are being added are independent [15], but not mutually exclusive. Independence here means that the probability of scattering due to a particular mechanism does not depend on the previous scattering events of a particle. Assumption of independence allows us to simply add the momentum relaxation times to arrive at the total relaxation time [15]. Moreover, if the energy-dependence of the scattering mechanisms are identical, then we can add the mobilities instead of relaxation times to arrive at the net mobility [15]. This in essence is the Matthiessen's summation rule.

The property of mutual-exclusiveness means that if a certain scattering event occurs, then it precludes some other scattering event from happening. For example, in equation (4.1), the phonon scattering term is added twice: first as a 2D term, and then as a 3D term. However, calculation of mobility near the surface must only consider the interaction of a quantized electron with a 3D phonon, and not the interaction of 3D electrons with 3D phonons. Nevertheless, equation (4.1) includes both interactions, and thus is a limitation of that formulation. We present a more physically-based formulation which is consistent with the nature of the various scattering mechanisms involved. Instead of partitioning events as either surface or bulk, we split them according to the nature of the perturbing potential. Thus, the proposed formulation takes on the following form:

$$\frac{1}{\mu_{total}} = \frac{1}{\mu_{phonon}} + \frac{1}{\mu_{surface\ roughness}} + \frac{1}{\mu_{Coulomb}} \tag{4.2}$$

The hierarchical taxonomy of the new model in equation (4.2) is shown in Figure 4.1. A detailed discussion on the modeling of each term in the hierarchy is covered in the following sections.

4.3 Phonon Scattering

4.3.1 General Considerations

To ensure the mutual-exclusivity of phonon scattering, it is expressed as the infinity norm[1] of 2D phonon and 3D phonon scattering:

$$\mu_{ph} = \boldsymbol{min}\left[\mu_{2D}^{ph}, \mu_{3D}^{ph}\right] \tag{4.3}$$

In this formulation, μ_{2D}^{ph}, the phonon-limited mobility near the surface, represents the

---

1. L_p norm of vector $\mathbf{x}$ is $\sqrt[p]{\sum_i x_i^p}$. Euclidean norm is p=2, whereas $p \to \infty$ yields $\boldsymbol{min}\{x_i$: i=1,....,N$\}$.

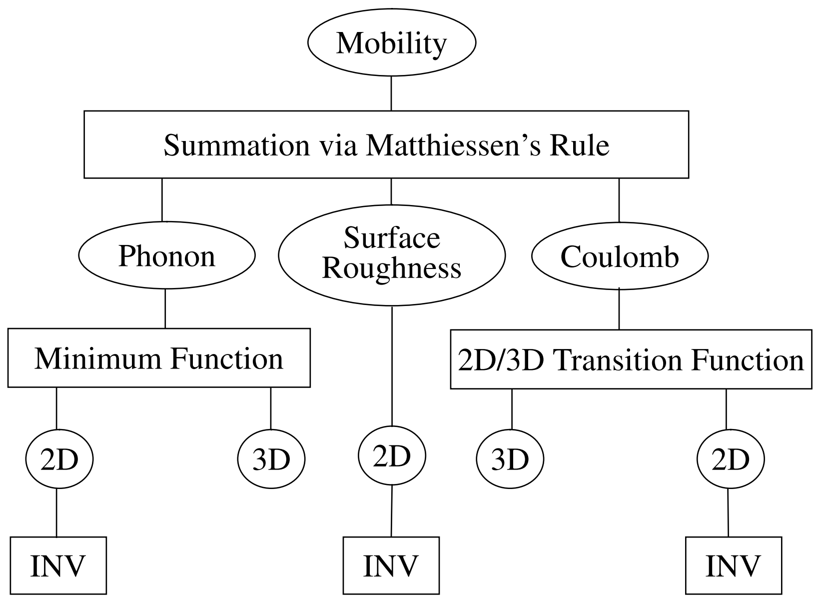

Figure 4.1 Hierarchical taxonomy of the new semi-empirical local model.

interaction between quantized electrons and bulk-mode (3D) phonons[1], whereas μ_{3D}^{ph}, the phonon-limited mobility in the bulk, represents the interaction between bulk electrons and bulk-mode phonons. On the other hand, the physical interpretation of the commonly used formulation — the one given in equation (4.1) — is that the calculation of phonon-limited mobility near the surface considers the interaction of 2D electrons with 3D phonons (the surface term) as well as the interaction of 3D electrons with 3D phonons (the bulk term). Clearly, calculation of mobility near the surface in the presence of a strong transverse field need not include the interaction of 3D electrons with phonons since electrons near the surface are quantized! This distinction is elegantly handled by equations (4.2) and (4.3).

1. 3D phonons are generated by atomic vibrations in which the elastic constant of the lattice is close to identical in all three directions, thus allowing bulk modes to exist. 2D phonons, also known as surfons, are generated if the elastic constant is sufficiently different in one direction, thus allowing interface modes to exist. In the Si/SiO_2 system, velocity of sound is not very different between the two media; hence, interface modes do not play a significant role in electron-phonon scattering. Thus, electron-phonon scattering in the inversion layer is treated entirely as the interaction between bulk-mode phonons and the two dimensional electron gas [8], [46].

Besides the fact that equation (4.1) inherently presents a non-physical picture, we shall see later that such a formulation does not allow us to extend the model to accumulation layers. Moreover, it was found that with the improved formulation given in equation (4.2), calibrating parameters assumed values that were in closer agreement with first-principle calculations.

4.3.2 Theoretical basis for 2D Phonon scattering

At room temperature, mobility in semiconductors is often dominated by phonon scattering, and hence its study occupies a central place in the theory of electrical transport in semiconductors. More importantly, phonon scattering unlike impurity scattering provides a mechanism for energy loss, i.e. interaction of electrons with certain kinds of phonons are inelastic in nature. In contrast, impurity scattering is purely elastic, and other than contributing to momentum randomization, it plays no role in energy relaxation. For instance, velocity saturation in semiconductors occurs entirely due to inelastic phonon scattering.

In developing the theory of energy band structure, it is assumed that the lattice atoms are frozen in space. However, in reality, the atoms vibrate about their equilibrium position, and it is this vibration that accounts for the thermal energy of the lattice. As a result of these vibrations, the periodic potential in the crystal varies with time and causes alterations in the electronic states with time. The scattering of electrons due to alterations in the periodic potential arising from atomic vibrations depends on the nature of these vibrations and the nature of the atoms making up the crystal.

Atomic vibrations in the crystal generate elastic waves which can vibrate in one of two modes. In the acoustic mode, neighboring atoms vibrate in phase, whereas in the optical mode, they vibrate out of phase. The frequency of vibration, and hence the energy, associated with the optical mode is higher than that of the acoustic mode. Optical mode gets it name because electromagnetic radiation in the optical region of the spectrum interacts with the optical mode, whereas acoustic mode gets it name because sound waves in a solid propagate via the longitudinal[1] acoustic mode. Phonons represent the quasi-particles associated with vibratory motion in the crystal, and depending on the

1. It should be pointed out that both acoustic and optical modes can vibrate either transversely or longitudinally.

mode, they are also termed as either acoustic or optical phonons.

Acoustic phonons in a crystal cause perturbations in potential in one of two ways. First, due to changes in the spacing of the lattice atoms, the energy band gap and the position of conduction and valence band edges vary from point to point. Potential discontinuites are thus produced in the conduction and valence bands. The potential so produced due to the deformation of the crystal is called the *deformation potential*, the magnitude of which is evidently proportional to the strain produced by the vibrations. The scattering of carriers by the deformation potential is called deformation potential scattering. The second kind of perturbation is produced by acoustic vibrations through the piezoelectric effect. If the atoms constituting the crystal are partially ionized, the displacement of atoms due to the acoustic vibrations would produce potentials, the magnitude of which would depend on the arrangement of the ionized atoms in the crystal. The scattering of electrons by a piezoelectric potential is referred to as piezoelectric scattering. This kind of scattering is important in compound semiconductors, particularly at low temperatures.

Optical phonons also scatter electrons in one of two ways. The deformation of the crystal due to optical vibrations produces a perturbing potential that is proportional to the optical strain. This type of scattering is termed as deformation potential scattering via the optical phonons, and in order to differentiate it from acoustic phonon deformation potential scattering, it is typically termed as non-polar optical phonon scattering. The second type of optical phonon scattering occurs by the creation of dipole moments due to oppositely charged neighboring atoms. These dipole moments result in a perturbing potential, and this type of scattering is known as polar optical phonon scattering.

Lastly, phonon scattering can either be intravalley or intervalley. The hierarchy of lattice scattering is shown in Figure 4.2. In silicon with six equivalent X-valleys, intervalley phonon scattering is an extremely important process, especially at high fields. It should also be pointed out that acoustic phonon scattering is quasi-elastic since it involves little exchange of energy with the electron. On the other hand, optical phonon scattering is highly inelastic, and hence plays an important role in high-field transport.

In low field transport, acoustic phonon scattering plays an important role. In pure silicon at low temperatures, intravalley acoustic phonon scattering dominates. As temperature rises, intervalley scattering becomes important, while at room temperature intravalley acoustic phonon scattering via the deformation potential and intervalley

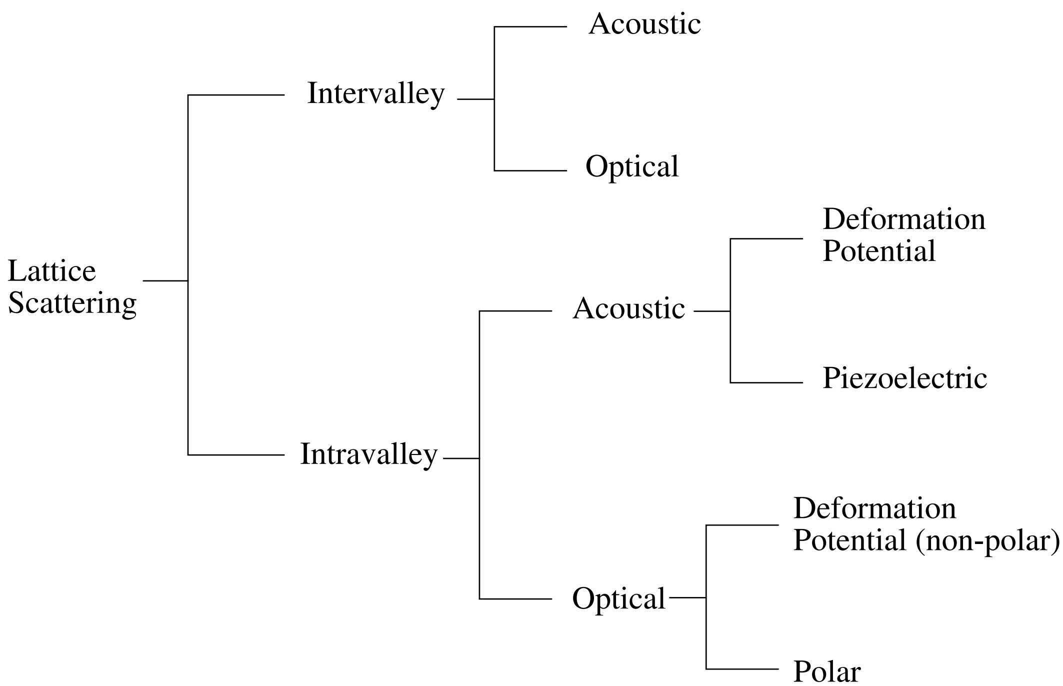

Figure 4.2 Hierarchical taxonomy of lattice scattering.

scattering are equally frequent. While intravalley scattering is predominantly due to acoustic phonon scattering, intervalley scattering is primarily due to optical phonon scattering. Since, we are interested in deriving an expression for low field mobility, we present a theoretical treatment of acoustic phonon scattering via the deformation potential (ADP).

In the deformation potential interaction, the scattering between electrons and phonons occurs when the electron waves scatter off phonon waves which are represented by elastic waves in a solid [15]:

$$u(x, t) = A_\beta e^{i(\mp \beta x - \omega t)} \tag{4.4}$$

where *u(x,t)* is the atomic displacement from the equilibrium position, A_β is the amplitude of the wave, β is the wavevector, and ω is the frequency. Since atoms vibrate in phase in acoustic phonon scattering, the interaction potential is given by [15]:

$$H_{ac} = D_{ac}\frac{\partial u}{\partial x} = \pm i\beta D_{ac}u \tag{4.5}$$

where H_{ac} is the interaction potential, and D_{ac} is known the deformation potential. The matrix element can hence be written as:

$$M(k, k') = \pm iD_{ac}A_{\beta}\beta\int e^{i(k-k'\pm\beta)x}dx = \pm iD_{ac}A_{\beta}\beta\delta(k-k'\pm\beta) \tag{4.6}$$

By equating classical and quantum energy terms, the following expression for A_{β} is obtained [15]:

$$A_{\beta}^{2} = \frac{(N_{\omega}+1/2)\hbar}{2M\omega} \tag{4.7}$$

N_{ω} is the occupation number of phonons (i.e. the number of phonons with frequency ω and hence with energy $\hbar\omega$), M is the total mass of atoms that interact with the electrons, N_{ω} is specified by Bose-Einstein statistics, and in the equipartition approximation, $N_{\omega} \approx kT/\hbar\omega$. From the dispersion relationship for phonons, $\omega/\beta = u_{l}$, where u_l is the velocity of sound in the crystal. Thus, the square of the matrix element becomes:

$$|M(k, k')|^{2} = \frac{D_{ac}kT}{2u_{l}^{2}M}\delta(k-k'\pm\beta) \tag{4.8}$$

In 3D, $M = \rho_{bulk}V$, where ρ_{bulk} is the density of silicon atoms per unit volume and V is the volume. In 2D, $M = \rho_{area}\Omega$, where ρ_{area} is the density of silicon atoms per unit area and Ω is the area. Since phonon scattering is isotropic (i.e. velocity randomizing), momentum relaxation time is the same as the inverse of the total scattering rate [15] (also see equation (2.27)). The expression for the total scattering rate in two dimensions is given by:

$$\frac{1}{\tau(\varepsilon)} = \frac{\Omega}{(2\pi)^{2}}\int\frac{2\pi}{\hbar}|M(k, k')|^{2}\delta(\varepsilon-\varepsilon'+\pm\hbar\omega)\ \mathrm{d}^{2}k \tag{4.9}$$

Substituting equation (4.8) in (4.9), the following expression for the momentum relaxation time is obtained [58], [46], [63]:

$$\frac{1}{\tau_{ac}} = \frac{m^* D_{ac}^2 kT}{\bar{h}^3 \rho_{area} u_l^2} \tag{4.10}$$

Low-field mobility is obtained by averaging the momentum relaxation time weighted by the energy over the distribution function [15], [59], [60]:

$$\mu = \frac{q}{m^*} \frac{2}{3kT} \frac{\int \varepsilon \cdot \tau(\varepsilon) \cdot f_o(\varepsilon) \cdot D(\varepsilon)\, d\varepsilon}{\int f_o(\varepsilon) \cdot D(\varepsilon)\, d\varepsilon} \tag{4.11}$$

where $f_o(\varepsilon)$ is the Maxwell-Boltzmann distribution function, $D(\varepsilon)$ is the density of states, and ε is the energy. Substituting the momentum relaxation time given in equation (4.10) into equation (4.11) yields the following expression for mobility [58], [47]:

$$\mu_{ac}^{2D} = \frac{q \bar{h}^2 \rho_{area} u_l^2}{(m^*)^2 D_{ac}^2 kT} \tag{4.12}$$

Since ρ_{area} is the areal mass density, it can be expressed as $\rho_{area} = \rho_{bulk} \cdot Z_{inv}$, where Z_{inv} is the thickness of the inversion layer. Hence, the expression for mobility takes on the following form:

$$\mu_{ac}^{2D} = \left[\frac{q \bar{h}^2 \rho_{bulk} u_l^2}{(m^*)^2 D_{ac}^2 k}\right] \cdot \frac{1}{T} \cdot Z_{inv} \tag{4.13}$$

4.3.3 A Semi-Empirical Model for 2D Phonon scattering

Although the model appearing in equation (4.13) is calculated from first-principles, it does not agree well with experimentally obtained results for phonon scattering in the inversion layer. Due to the simplifying assumptions made in the derivation of the model in equation (4.13), a good agreement is not expected in the first place. However, what equation (4.13) does provide is an insight into the trend of how acoustic phonon mobility changes with respect to parameters such as temperature and inversion-layer thickness. In formulating a model that must agree with experimental data, the functional dependences from the first-principles model in equation (4.13) are retained but the proportionality constant is allowed to vary to achieve good agreement with experimental data. Such an approach is termed as semi-empirical modeling since we start with a physically-based formulation, but vary prefactorial parameters until a good match with experimental data is obtained. At the other extreme is empirical modeling in which all the parameters are allowed to vary. Therefore, when equation (4.13) is cast in semi-empirical form, the following expression is obtained [30]:

$$\mu_{2D}^{phonon} = \Lambda \cdot \frac{1}{T} \cdot Z_{inv} \tag{4.14}$$

where Λ is a calibrating parameter to be determined by comparison with experimental data, T is the lattice temperature, and Z_{inv} is the thickness (or the width) of the quasi-two-dimensional[1] electron gas. The width of the inversion layer can be calculated either classically or quantum mechanically.

A quantum mechanical analysis, in which the wave nature of electrons is emphasized, is necessary if the dimension of the confining potential is comparable to the deBroglie wavelength, $\lambda_{el} = h/\sqrt{3m^* k_B T}$, of electrons, which at room temperature is approximately 150Å. In modern submicrometer MOSFETs, thinner gate oxides have resulted in steeper potential wells near the interface, thus mandating a partial if not a complete quantum mechanical treatment. If the electrons are indeed represented as wavefunctions, then it has been found that the nature of the electron distribution in the channel is significantly different from the case in which the electrons are treated as classical particles [48], [49]. Figure 4.3 illustrates this difference. The potential at the Si/SiO_2 interface is assumed to be infinitely large. Hence the wavefunction vanishes at the interface because of which the probability of finding an electron at the interface is zero. Contrast this with the classical calculation in which the electron density is maximum at the interface.

1. Quasi-2D instead of strictly 2D because of the finite spatial extent in the depth direction. It is this spatial extent that we are defining as the width of the inversion layer.

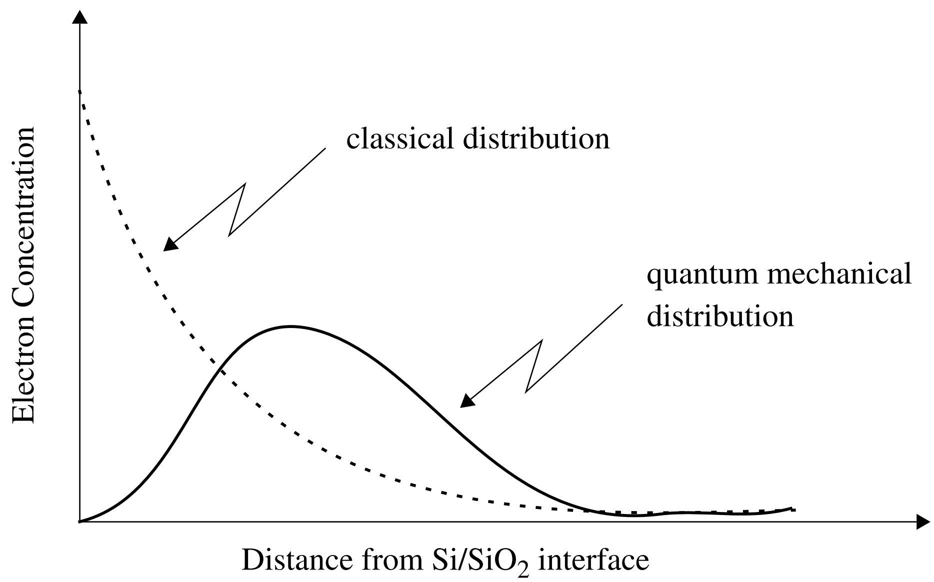

Figure 4.3 Comparison between classical and quantum mechanical calculations of electron density in the inversion layer of MOSFETs.

In the quantum mechanical calculation, Poisson and Schrodinger equation is solved self-consistently. For Poisson equation, the input is the charge density, and the output is the potential profile which forms the input to Schrodinger equation whose output is the wavefunction $\psi(z)$ and the energy eigen-values ε_i. Thus, the coupling between the two equations is via a constitutive equation relating the wavefunction to the electron density. If the number of electrons in a particular subband is N_i, then the electron density at a point z below the interface is:

$$n(z) = \sum_i N_i \cdot |\psi_i(z)|^2 \tag{4.15}$$

where $\psi_i(z)$ is the wavefunction in the *i-th* subband. N_i can be simply calculated through the 2D density of states and the Fermi-Dirac distribution function:

$$N_i = \frac{g_v m_d}{\pi \hbar^2} \int_{\varepsilon_i}^{\infty} f(\varepsilon)\, d\varepsilon = \frac{g_v m_d}{\pi \hbar^2} kT \ln\left[1 + e^{(\varepsilon_F - \varepsilon_i)/(kT)}\right] \tag{4.16}$$

where g_v is the valley degeneracy, m_d is the density-of-states effective mass, ε_i is the energy eigenvalue in the *i-th* band, and ε_F is the fermi level.

The primary difference between the quantum calculation and the classical calculation is that in the classical calculation, Schrodinger equation is not solved for. Instead the electron density is given by the usual 3D calculation:

$$n(z) = \int_{\varepsilon_C(z)}^{\infty} D(\varepsilon) f(\varepsilon)\, d\varepsilon \approx N_C e^{[\varepsilon_F - \varepsilon_C(z)]/(kT)} \tag{4.17}$$

To compute the quantum mechanical thickness of the electron gas, we start by computing the average thickness of the electron gas in each subband [44]:

$$\langle z_i \rangle = \int \psi_i^*(\boldsymbol{r}, z) \cdot z \cdot \psi_i(\boldsymbol{r}, z)\, dz d\boldsymbol{r} = \int \psi_i^*(z) \cdot z \cdot \psi_i(z)\, dz \tag{4.18}$$

The average thickness for the quantized gas is then given by averaging over all the $\langle z_i \rangle$:

$$Z_{QM} = \sum_i c_i \langle z_i \rangle \tag{4.19}$$

where c_i is the fraction of the total number of electrons in the *i-th* subband:

$$c_i = \frac{N_i}{\sum_i N_i} \tag{4.20}$$

Calculating Z_{QM} via equations (4.18) and (4.19) requires knowing $\psi_i(z)$ first, which can only be obtained by numerically solving Schrodinger's equation and Poisson's equation in a self-consistent fashion. However, if we seek an analytical solution, the two equations can be *decoupled* by assuming some reasonable form for the potential profile in the inversion layer. The assumption typically made is that of a triangular well and the resulting wavefunctions are given by Airy functions [49]. However, Stern [45] points out that the triangular well approximation is a reasonable one if there is little or no charge in the inversion layer, but it fails if the inversion-layer charge is comparable to or more than the depletion layer charge. When only one subband is occupied (i.e. in the electric quantum limit), a variational approach [51] gives a good estimate for the energy eigenvalue of the lowest subband. In this approach, instead of postulating a form for the potential well, a trial eigenfunction is used with a single undetermined parameter, that is calculated by minimizing the total energy of the system. When such an approach is used, Z_{QM} becomes $\langle z_o \rangle$, and is given by [45], [50]:

$$Z_{QM} = \left[\frac{9\hbar^2}{4m_{eff}qE_{\perp,\,eff}}\right]^{1/3} \tag{4.21}$$

where $E_{\perp,\,eff} = \frac{q}{\kappa_{si}\varepsilon_o}\left[\frac{11}{32}N_{inv} + N_{depl}\right]$ is the transverse effective field in the inversion layer. In the presence of strong transverse fields, the width of the inversion layer closely follows the quantum mechanical term due to strong quantization — most of the carriers do occupy the lowest subband. However, in weak quantization, multiple subband occupation takes place, and hence equation (4.21) breaks down. For this case, the width of the inversion layer is well modeled in classical terms. If we imagine that the spread of the electron gas in energy is of the order to the thermal energy kT, then *force* x *distance* gives the energy of the gas which is $qE_{surface} \cdot Z_{CL}$. If we replace $E_{surface}$ by the effective field in the inversion layer E_{eff}, and equate $qE_{surface} \cdot Z_{CL}$ with the thermodynamic energy of the gas which is *(3/2)kT*, we get the following expression for Z_{CL} [29]:

$$Z_{CL} = \frac{(3/2) \cdot kT}{qE_{\perp,\,eff}} \tag{4.22}$$

To arrive at a formulation for Z_{inv} that is applicable at all electric fields, one possibility is to express Z_{inv} as $Z_{QM} + Z_{CL}$, where the larger of the two numbers would set the value for Z_{inv}. If E_{eff} is small, $Z_{CL} > Z_{QM}$, and hence $Z_{inv} \approx Z_{CL}$, which is what is desired. Conversely, if E_{eff} is large, $Z_{CL} < Z_{QM}$, and hence $Z_{inv} \approx Z_{QM}$. The transition from classical to quantum regime is illustrated in Figure 4.4. Armed with this definition for Z_{inv}, phonon mobility in the inversion layer can be written as [30]:

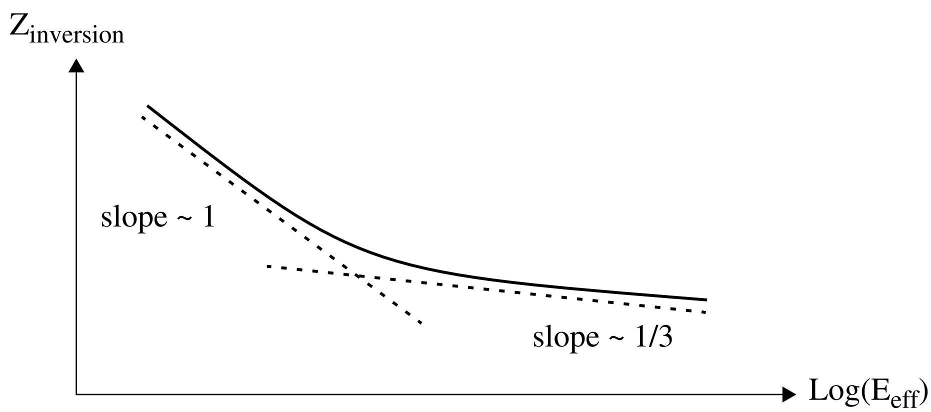

Figure 4.4 Thickness of the inversion layer as a function of transverse electric field. At low fields, classical formulation is required, whereas at high fields, quantum mechanical formulation is applicable.

$$\mu_{inv}^{ph} = \frac{A}{E_{\perp,\,eff}} + \frac{B \cdot N_A^{\gamma}}{T \cdot E_{\perp,\,eff}^{1/3}} \tag{4.23}$$

The effective field appearing in equation (4.23) is a non-local quantity, i.e. its calculation requires summing information from various nodes. From a numerical simulation point of view, non-local quantities are highly undesirable since they potentially slow down the computation by increasing the bandwidth of the Jacobian matrix [55]. On the other hand, if the Jacobian entries are altogether neglected, then it is not possible to perform an accurate small signal analysis using the model [1]. Finally, it is implicit in the definition of the non-local field that it assumes planarity of the Si/SiO_2 interface which limits the simulation to planar devices only [1].

On the other hand, the definition of the local electric field is based on local information only. It allows the Jacobian to be set up symbolically for small signal analysis; does not increase the bandwidth of the Jacobian matrix, and allows for the simulation of non-planar devices. Thus, from a numerical implementation point of view, all models should be strictly locally based [1]. By their very nature, macroscopic models derived from basic physics would necessarily involve averaging over microscopic quantities. In certain instances, such as for the two dimensional electron gas, averaging would be performed spatially as well, resulting in a reduced-dimensionality variable such as integrated channel charge N_{inv}. For such cases, we need to make the transformation at the numerical level from a 2D variable to a 3D variable.

In going from a 3D to a 2D variable, integration needs to be performed over one of the space coordinates. For instance, in the case of the non-local effective field

$$E_{\perp,\,eff} = \frac{\int E_{\perp}(z)\, n(z)\, dz}{\int n(z)\, dz} \tag{4.24}$$

where $E_{\perp}(z)$ is the local transverse electric field at coordinate z below the Si/SiO$_2$ interface, and $n(z)$ is the local electron concentration at z. While there is a unique transformation from $E_{\perp}$ to E_{eff}, the reverse transformation is clearly not unique. One possibility is to simply set E_{eff} equal to $E_{\perp}$ as proposed by Lombardi *et. al.* [30]. Although this may appear to be an *ad hoc* approach, it should be noticed that the formulation in equation (4.14) is a semi-empirical approach to begin with, and hence any further deviation between theory and experiment due to such a transformation can be easily accommodated by recalibrating the fitting parameter Λ. Thus, the resulting semi-empirical model for phonon scattering in the inversion layer is given by:

$$\mu_{inv}^{ph}(\boldsymbol{r}) = \frac{A}{E_{\perp}(\boldsymbol{r})} + \frac{B \cdot N_A^{\gamma}}{T \cdot E_{\perp}^{1/3}(\boldsymbol{r})} \tag{4.25}$$

Ideally, the fitting parameter γ appearing in equation (4.25) should be zero, since electron-phonon interactions depend on the vibrational properties of the lattice and not specifically the dopant concentration. The need for a non-zero γ can be postulated as follows. Note that the model in equation (4.25) is formulated as a local model (i.e. $E_{\perp}$ is a local function of the space coordinates (x,y,z)). On the other hand, the experimentally observed universal mobility curve [43] is expressed as a function of the non-local transverse electric field E_{eff} defined in equation (4.24). The calculation of a non-local mobility from the local mobility involves integration in the depth direction (similar to the case of the non-local electric field):

$$\mu_{eff} = \frac{\int \mu(z)\, n(z)\, dz}{\int n(z)\, dz} \tag{4.26}$$

The effective mobility obtained via equation (4.26) needs to reproduce the universal mobility curve [43], and it was observed that a slight dependence of N_A is required in equation (4.25) in order to fit the local model with experimental data. This may have to do with the fact that since there is no unique transformation from the non-local field to the local electric field, making the arbitrary transformation of $E_{eff} \rightarrow E_{\perp}$ in equation (4.25) introduces a functional dependence on N_A.

4.3.4 An Empirical Model for 3D Phonon Scattering

Scattering rate due to any perturbing potential is proportional to the density of states available to the particles [64]. Confinement changes the energy dependence of the electron density of states in a parabolic band structure from $\varepsilon^{1/2}$ in the bulk to ε^{o} in 2D. Thus, for three dimensional scattering, the momentum relaxation time obtained in equation (4.10) for two dimensions changes to:

$$\frac{1}{\tau_{ac}} = \frac{\pi D_{ac}^{2} kT}{\hbar \rho_{bulk} u_l^2} g_{3D}(\varepsilon) = \frac{D_{ac} kT (2m^*)^{3/2} \varepsilon^{1/2}}{4\pi \hbar^4 \rho_{bulk} u_l^2} \tag{4.27}$$

From equation (4.11), mobility for 3D phonons is thus calculated to be:

$$\mu_{ac}^{3D} = \frac{2^{2/3}}{3} \frac{q \pi^{1/2} \hbar^4 \rho_{bulk} u_l^2}{D_{ac}^2 (m^*)^{5/2} (kT)^{3/2}} \tag{4.28}$$

In comparing 3D mobility with 2D mobility (see equation (4.12)), we see that the temperature dependence is much stronger in 3D compared to 2D. While equation (4.28) provides a first-principles model, it is found experimentally that phonon mobility does not quite follow the $T^{-1.5}$ dependence as given in (4.28). Instead, the dependence is found to be stronger, and hence the model for phonon scattering becomes purely empirical since we calibrate both the proportionality constant as well as the exponent. Recall that in a semi-empirical model, the exponent is taken straight from first-principles analysis. Thus, the model for three dimensional phonon scattering takes the form [61], [62]:

$$\mu_{ac}^{3D} = \mu_{max}\left(\frac{300}{T}\right)^{\theta} \tag{4.29}$$

where $\theta = 2.285$ and $\mu_{max} = 1417$ cm^2/V-sec. Therefore, the expression for total phonon mobility given by equation (4.3) becomes:

$$\mu_{ph} = \boldsymbol{min}\left[\frac{A}{E_{\perp}(\boldsymbol{r})} + \frac{B \cdot N^{\gamma}{}_{A}}{T \cdot E_{\perp}^{1/3}(\boldsymbol{r})}, \mu_{max}\left(\frac{300}{T}\right)^{\theta}\right] \tag{4.30}$$

In equation (4.30), the parameter that determines whether phonon mobility is given by the 2D term or by the 3D term is the transverse electric field $E_{\perp}(\boldsymbol{r})$. If gate bias is sufficiently large to cause inversion and hence quantization of the electron gas, then $E_{\perp}(\boldsymbol{r})$ is large near the interface. Thus, the calculation of μ_{ph}^{2D}, which is inversely related to $E_{\perp}(\boldsymbol{r})$, would result in a small numerical value. If this value is less than the value for μ_{ph}^{3D}, then μ_{ph} would be given by μ_{ph}^{2D}. In going from the surface into the bulk, $E_{\perp}(\boldsymbol{r})$ decreases in value, and hence μ_{ph}^{2D} increases in value. If μ_{ph}^{2D} exceeds μ_{ph}^{3D}, then at that point, μ_{ph} is given by μ_{ph}^{3D}. The transition from 2D to 3D mobility is illustrated in Figure 4.5.

4.4 Surface Roughness Scattering

In deep submicron MOSFETs with scaled dielectrics, surface roughness scattering has become a major limiting factor due to the presence of high transverse electric fields. We first present a first principles approach to modeling surface roughness, and then present a semi-empirical model that is calibrated against experimental data.

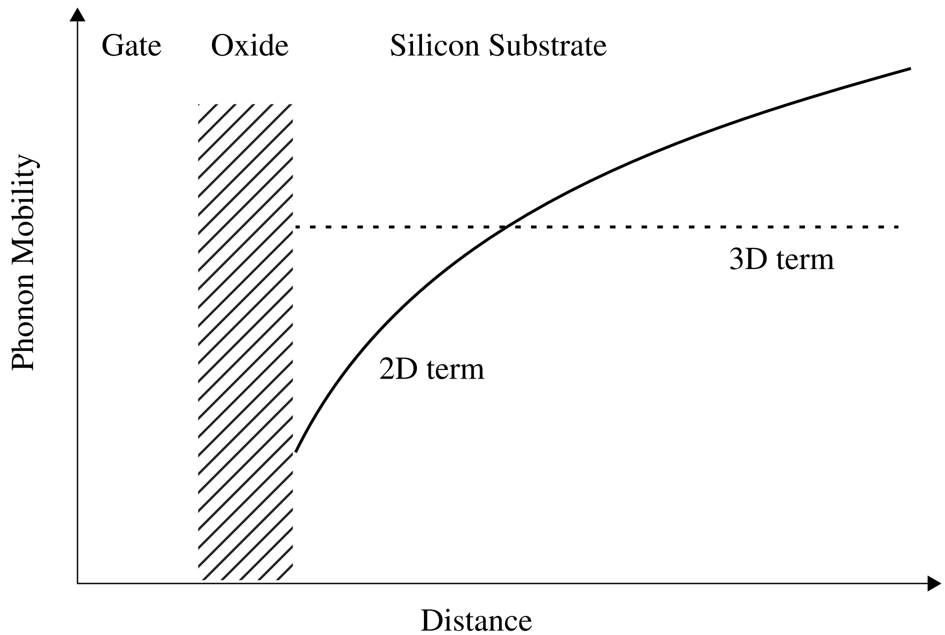

Figure 4.5 Illustrating the transition from 2D mobility to 3D mobility as one moves from the surface into the bulk. The assumption in this figure is that there is sufficient gate bias to cause the 2D term at the interface to be less than the 3D term (which is independent of the value of transverse electric field).

4.4.1 Theoretical basis for Surface Roughness Scattering

Surface roughness occurs due to surface irregularities at the interface. Thus, it is purely a two dimensional effect with no analog in the bulk. Surface roughness scattering has been theoretically investigated using a simple model [65] which assumes that only the lowest subbands are occupied, and deviations from perfect planarity $\Delta(x,y)$ are small in magnitude and slowly varying in the x-y plane. Here we assume that the x-y plane is parallel to the Si/SiO_2 interface.

Due to variations in the z direction, i.e. the direction normal to the interface, potential in the z direction is perturbed as well. Hence, the resulting Hamiltonian is given by [66]:

$$H = H_o + \delta H = -\frac{\hbar^2}{2m}\nabla^2 + V[z + \Delta(x, y)] \tag{4.31}$$

Thus, the perturbing (interaction) potential, H-H_o, is given by:

$$\delta H = V[z - \Delta(x, y)] - V[z] \approx \frac{\partial V}{\partial z}\Delta(x, y) \tag{4.32}$$

Therefore, the matrix element for this perturbing potential is given by [67]:

$$\langle \Psi' | \delta H | \Psi \rangle = \left[\int_{-\infty}^{\infty} \zeta^*(z) \frac{\partial V}{\partial z} \zeta(z)\, dz \right] \times \frac{1}{A}\left[\int_A \Delta(\boldsymbol{R})\, e^{i(k-k)\cdot R} d\boldsymbol{R} \right] \tag{4.33}$$

To evaluate the first integral on the right hand side, the variational wavefunction ζ(z) proposed by Stern and Howard [50] is used:

$$\zeta(z) = \sqrt{\frac{b^3}{2}}\, z e^{-bz/2} \tag{4.34}$$

where

$$b = \sqrt[3]{\left[\frac{48\pi e^2 m}{\kappa_{si}\hbar^2}\right] \cdot \left[N_{depl} + \frac{11}{32}N_{inv}\right]} \tag{4.35}$$

As shown by Matsumoto and Uemura [68], the integral is proportional to the effective field in the inversion layer:

$$\int_{-\infty}^{\infty} \zeta^*(z) \frac{\partial V}{\partial z} \zeta(z)\, dz = \frac{q^2}{\kappa_{si}\varepsilon_o}\left(\frac{11}{32}N_{inv} + N_{depl}\right) = qE_{eff} \tag{4.36}$$

The second integral on the right hand side of equation (4.33) is simply the spatial Fourier transform of Δ(x,y):

$$\Delta(\boldsymbol{q}) = \frac{1}{A}\int_A \Delta(\boldsymbol{R})\, e^{i(k-k')\cdot R} d\boldsymbol{R} \tag{4.37}$$

where $\boldsymbol{q} = k - k'$. $\Delta(\boldsymbol{R})$ is assumed to have a Gaussian form of correlation between two points [69] such that:

$$\langle \Delta(\boldsymbol{R})\, \Delta(\boldsymbol{R} + \boldsymbol{R_1}) \rangle = \Delta^2 e^{-\boldsymbol{R}_1^2/\Lambda^2} \tag{4.38}$$

where <· · ·> denotes the sample average, Δ is the root mean square deviation of the interface, and Λ is the correlation length. Defined this way, $|\Delta(\boldsymbol{q})|^2$ is obtained as [67]:

$$|\Delta(\boldsymbol{q})|^2 = \frac{\pi\Delta^2\Lambda^2}{A} e^{-q^2\Lambda^2/4} \tag{4.39}$$

If we neglect screening by the 2D electron gas, then the square of the matrix element is given by:

$$|\langle\Psi'|\delta H|\Psi\rangle|^2 = q^2 E_{eff}^2 |\Delta(\boldsymbol{q})|^2 \tag{4.40}$$

and hence the scattering probability via the Fermi's Golden Rule is obtained as:

$$S(k, k') = \frac{2\pi}{\hbar}|\langle\Psi'|\delta H|\Psi\rangle|^2 \delta[\varepsilon(k) - \varepsilon(k')] = \frac{2\pi}{\hbar} q^2 E_{eff}^2 |\Delta(\boldsymbol{q})|^2 \delta(\varepsilon_k - \varepsilon_{k'}) \tag{4.41}$$

The momentum relaxation time for an elastic scattering event such as Coulombic scattering or surface roughness scattering is given by equation (2.35):

$$\frac{1}{\tau_m(\boldsymbol{k})} = \frac{A}{(2\pi)^2}\int S(\boldsymbol{k}, \boldsymbol{k'})\, [1 - \cos\theta]\, d\boldsymbol{k'} \tag{4.42}$$

Therefore, the momentum relaxation time for surface roughness scattering is given by:

$$\frac{1}{\tau_{sr}} = \frac{q^2 E_{eff}^2 \Delta^2 \Lambda^2}{2h}\int e^{-q^2\Lambda^2/4} \delta(\varepsilon_k - \varepsilon_{k'})\, [1 - \cos\theta]\, d\boldsymbol{k'} \tag{4.43}$$

As shown by Harstein *et. al.* [52], the correlation length Λ is about 6Å, and hence the quantity $k\Lambda$ is much less than unity. In this case, the relaxation time for surface roughness is approximated by:

$$\frac{1}{\tau_{sr}} = \frac{\pi m^* (\Delta \Lambda q E_{eff})^2}{\hbar^3} \tag{4.44}$$

and the corresponding mobility calculated from equation (4.11) is obtained as:

$$\mu_{sr} = \left[\frac{\hbar^3}{\pi (m^*)^2 (\Delta\Lambda)^2 q}\right] \cdot \frac{1}{E_{eff}^2} \tag{4.45}$$

Thus, we find that surface roughness mobility has a much stronger dependence on the transverse effective field compared to phonon mobility. That is why at high electric fields, mobility is limited more by surface roughness scattering than by phonon scattering.

4.4.2 A Semi-Empirical Model for Surface Roughness Scattering

The first principles model for surface roughness scattering is presented in equation (4.45). In some sense, it is a semi-empirical model since the parameters Δ and Λ that characterize the Si/SiO_2 interface cannot be obtained from a microscopic description of the interface since such a calculation does not exist at present. Instead, Δ and Λ are typically determined by fitting experimental data with the model in equation (4.45). If we lump all the parameters and constants into one fitting parameter, the resulting semi-empirical model becomes [52]:

$$\mu_{sr} = \frac{\delta}{E_{eff}^2} \tag{4.46}$$

In transforming the model from a non-local formulation to a local formulation, we set E_{eff} as $E_{\perp}$ to obtain [1], [30]:

$$\mu_{sr} = \frac{\delta}{E_{\perp}^{2}(\boldsymbol{r})} \tag{4.47}$$

When the universal mobility curve was extracted using equations (4.24) and (4.26) from the local model as defined later in equation (4.80), it was found that a constant δ failed to reproduce the experimental UMC. As for the case of phonon scattering (see equation (4.25)), incorporating a slight doping dependence in the δ term led to good agreement between the local model and experimental results. Thus, the resulting model for surface roughness scattering is postulated as:

$$\mu_{sr} = \frac{C \cdot N_A^{\gamma}}{E_{\perp}^{2}(\boldsymbol{r})} \tag{4.48}$$

Note that surface roughness scattering is really a 2D scattering mechanism with no analog in 3D. Thus, as the distance from the surface increases, the magnitude of the transverse electric field decreases, and surface roughness mobility increases. The transverse electric field approaches zero in the bulk region; hence surface roughness mobility tends to infinity. Thus, the surface roughness term drops out in the calculation of total mobility as given by the Matthiessen's summation in equation (4.2).

4.5 Coulombic Scattering

Having discussed the semi-empirical formulations for phonon and surface roughness scattering, we now turn our attention to Coulombic scattering. In semiconductors, Coulombic scattering is the interaction of carriers (electron or holes) with any form of charge centers. These charge centers can be either stationary such as ionized impurity atoms, interfacial charges at the Si-SiO_2 interface, fixed charges in the oxide or they may be mobile such as carriers themselves. Coulombic scattering between carriers and stationary centers can be treated within the framework of one formulation, whereas carrier-carrier scattering requires a separate formulation since now the scattering potential is no longer constant as is the case for the scattering of carriers by stationary centers. In what follows, we are primarily interested in Coulombic scattering due to ionized impurities, which is also simply known as impurity scattering. Note that the terms

Coulombic scattering and impurity scattering would be used interchangeably since only one mechanism in the hierarchy of Coulombic scattering is being considered.

Coulombic scattering requires a slightly different formulation from phonon scattering since in the case of Coulombic scattering there is no natural variable that allows a transition to be made from 2D to 3D mobility. In the case of phonon scattering (see equation (4.30)), the transverse electric field $E_{\perp}$ serves the role of a transition variable, and such a formulation works very well since 2D phonon mobility is a function of $E_{\perp}$ (see equation (4.25)) whereas 3D phonon mobility is independent of $E_{\perp}$ (see equation (4.29)).

The problem arises because of the fact that inherently, Coulombic scattering in 2D is a function of the electron density, and not of the electric field. In other words, changes in E_{eff} do not necessarily cause changes in Coulombic mobility unless carrier density changes as well. This is due to the fact that E_{eff} can change while N_{inv} is held constant. This is seen most simply by examining the relationship between E_{eff} and N_{inv}:

$$E_{eff} = \frac{q}{\varepsilon_{si}}[\eta N_{inv} + N_{depl}] \tag{4.49}$$

While $N_{inv} \propto [V_{gs} - V_T(V_{sb})]$, it can be easily shown that $E_{eff} \propto [V_{gs} + V_T(V_{sb})]$. Thus combinations of V_{gs} and V_{sb} that keep N_{inv} constant would not hold E_{eff} constant and vice versa. The lack of a one-to-one correspondence between E_{eff} and N_{inv} is evident from equation (4.49) where it can be seen that a monotonically changing N_{inv} does not guarantee a monotonically changing E_{eff}. The lack of a unique relationship between N_{inv} and E_{eff} is why the N_{inv} dependence in Coulombic scattering cannot be transformed to an E_{eff} dependence.

For phonon scattering, the field term $E_{\perp}(\boldsymbol{r})$ serves as a useful transition variable since 2D phonon mobility varies with $E_{\perp}(\boldsymbol{r})$ but 3D phonon mobility does not. However, for Coulombic scattering, the electron density $n(\boldsymbol{r})$ cannot be directly used as a transition variable either since both 2D and 3D Coulombic mobilities are functions of $n(\boldsymbol{r})$. Since neither of the intrinsic variables $n(\boldsymbol{r})$ or $E_{\perp}(\boldsymbol{r})$ can be used as transition variables, transition *functions* are explicitly created that delineate the two and three dimensional regimes.

The most natural way to distinguish between 2D and 3D regimes is to consider the nature of a quantum well (i.e. the degree of quantization). A steep potential well would indicate strong quantization, and hence a two dimensional behavior, whereas a shallow potential well would indicate weak quantization, and thus warrant a three dimensional treatment.

To formulate the transition function for Coulombic scattering, it is postulated that in a narrow quantum well the electron gas is quantized, and Coulombic mobility is given by the 2D term. On the other hand, in a shallow quantum well the electron gas behaves like a 3D gas, and hence Coulombic mobility is given by the 3D term. In the triangular well approximation [8], the energy eigenvalue of the *i-th* sub-band is given by:

$$\varepsilon_i = \left(\frac{3\pi\hbar}{2}\right)^{2/3} \cdot q^{2/3} \cdot \left(\frac{1}{2m_z}\right)^{1/3} \cdot (i + 0.75)^{2/3} \cdot E_{\perp,\,eff}^{2/3} \tag{4.50}$$

Figure 4.6 illustrates the formation of subbands in the quasi-triangular potential well. Note

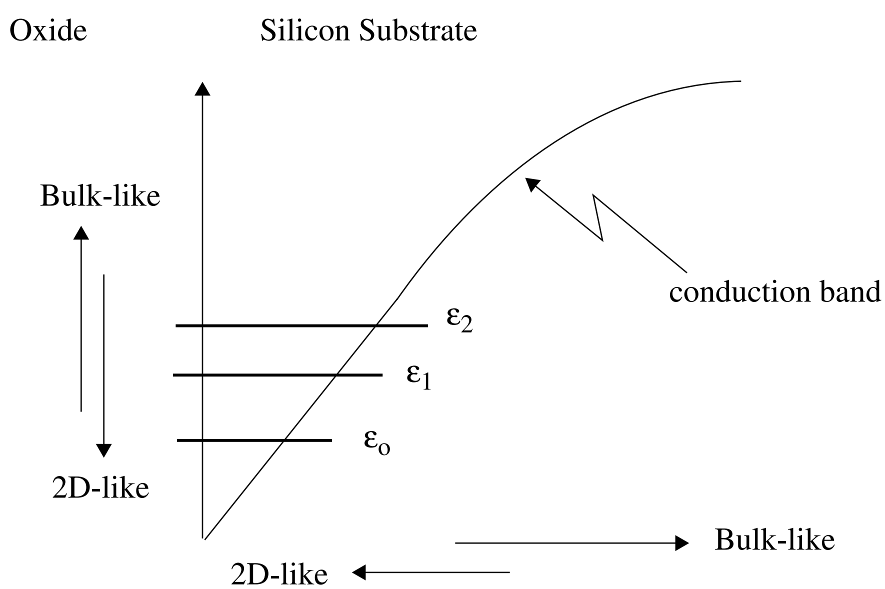

Figure 4.6 Illustrating the formation of energy subbands due to triangular well confinement of the electron gas near the Si-SiO_2 interface.

that in going from the surface into the bulk, the confinement length between the conduction band and the oxide barrier increases, thus reducing the degree of quantization. Since quantization is strongest near the bottom of the conduction band, the separation of sub-bands is largest near the bottom which decreases as one moves towards the bulk. Therefore, the energy separation between the lower subbands can serve as a good indicator for the degree of quantization. Considering just the energy separation between the zeroth and the first energy level, one obtains from equation (4.50):

$$\varepsilon_1 - \varepsilon_0 = \Delta\varepsilon = 9.49\times10^{-26} \cdot \left(\frac{E_{\perp, eff}^2}{m_{eff}}\right)^{1/3} \tag{4.51}$$

The transformation $E_{\perp, eff} \rightarrow E_{\perp}(\boldsymbol{r})$ is made in order to allow for a local calculation.

If the Si-SiO$_2$ interface is along the (100) plane, two sets of energy sub-bands, also known as ladders, are created in the quantum well due to differing effective masses. From the six-fold degeneracy of the silicon band structure, two valleys are aligned with the transverse field, whereas the other four valleys are perpendicular to the transverse field. Electrons in the aligned valleys exhibit longitudinal mass, whereas those in the perpendicular valleys exhibit transverse mass. In silicon, the transverse effective mass is smaller, and from equation (4.51) this set of energy bands exhibits greater sub-band separation. On the other hand, the two valleys with the longitudinal mass are less separated in energy, and in absolute values also are lower in energy. For instance, energy of the lowest sub-band in the longitudinal ladder set is lower than that of the transverse set. Thus, the longitudinal ladder set is considered in our calculations since it is the first to get occupied. For this ladder, $m_{eff} = 0.92$, and hence, equation (4.51) becomes:

$$\varepsilon_1 - \varepsilon_0 = \Delta\varepsilon = 9.757\times10^{-26} \cdot E_{\perp}^{2/3}(\boldsymbol{r}) \tag{4.52}$$

where $E_{\perp}$ is expressed in V/m and $\Delta\varepsilon$ in Joules.

If the energy separation, $\Delta\varepsilon$, is larger than kT, the thermal spreading energy, then most of the carriers would occupy the ground state, and the electron gas can be treated as being quantized or two-dimensional. Conversely, if the energy separation is smaller than kT, then both the sub-bands would be occupied, and we can treat the electron gas as being bulk-like. Thus, the parameter of interest, α, is defined as $\Delta\varepsilon / kT$:

$$\alpha = \frac{2.1 \times 10^{-24} \cdot E_{\perp}^{2/3}}{kT} \tag{4.53}$$

where $E_{\perp}$ is expressed in V/cm, k is the Boltzmann's constant, and T is the temperature in Kelvins.

If α is large, the quantization is strong, and conversely, for small α electrons behave like a 3D gas. A transformation is required from α to a number which is bounded between zero and one. For instance, when α is large, this function of α should map to zero, and if α is small, it should map to one. Clearly a threshold point is needed and also a specification of the degree of abruptness of the transition from zero to one. One possible transform function, closely resembling the Fermi-Dirac distribution function, is proposed below:

$$f(\alpha) = \frac{1}{1 + e^{(\alpha - \lambda)/\eta}} \tag{4.54}$$

The transition point is defined by λ (akin to the fermi level), and the abruptness of the transition is defined by η (akin to kT). Postulating that if $\Delta\varepsilon > 2kT$, the electron gas near the surface is quantized, and conversely if $\Delta\varepsilon < 2kT$, it is bulk-like, λ is set equal to 2. In order to make the transition from 2D to 3D sharp, η is chosen to be 0.5. The function $f(\alpha)$ is schematically shown in Figure 4.7. Thus, Coulombic mobility can now be expressed as:

$$\mu_{coulomb} = f(\alpha) \cdot \mu_{3D}^{coulomb} + [1 - f(\alpha)] \cdot \mu_{2D}^{coulomb} \tag{4.55}$$

Near the interface if $E_{\perp}$ is large, $\Delta\varepsilon$ would be large, and consequently α would be large. Hence, $f(\alpha)$ would be close to zero, and the Coulombic mobility in equation (4.55) would tend to $\mu_{2D}^{coulomb}$. Conversely, if at any point in the device the transverse field $E_{\perp}$ (also called the confining field) is small, α would be small and $f(\alpha)$ would be close to one. The resulting Coulombic mobility would then be equal to $\mu_{3D}^{coulomb}$.

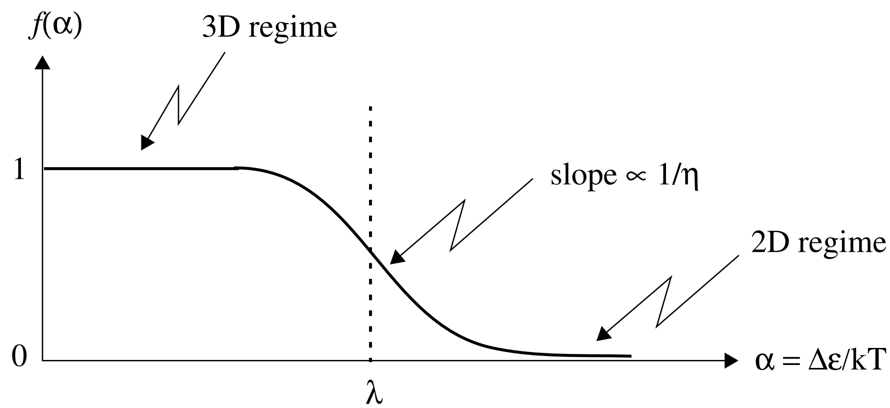

Figure 4.7 The transition function $f(\alpha)$ from 2D to 3D Coulombic mobility.

4.5.1 A Semi-Empirical Model for 2D Coulombic Scattering

In Chapter 3, a first principles model for two dimensional Coulombic scattering was presented [2], which is a non-local model since it is a function of the integrated channel charge, N_{inv} that is obtained from the local electron concentration by integration:

$$N_{inv}(x) = \int_0^\infty n(x, z)\, dz \tag{4.56}$$

where x is the direction from the source to the drain and z is the direction from the interface into the bulk. To arrive at a local formulation for 2D Coulombic scattering, the transformation $N_{inv} \to n$ is made, and all proportionality constants appearing in the first-principles model are replaced with calibrating parameters. For Coulombic scattering, it is found that to get the best fits, the exponents need to be perturbed as well, thus resulting in the following model [1]:

$$\mu_{coul}^{2D} = max\left[\left(D_1 \frac{n^{\kappa}}{N_A^{\beta_1}}\right), \left(\frac{D_2}{N_A^{\beta_2}}\right)\right] \tag{4.57}$$

where n is the local electron concentration and N_A is background acceptor atoms density. The first term represents the *screened* and the second term represents the *unscreened* Coulombic scattering. As electron density in the inversion-layer increases, the free charge carriers screen out the Coulomb field due to the acceptor atoms, and hence, the mobility increases. Conversely, as the free carrier concentration asymptotically goes to zero, mobility due to the screened term also goes to zero. However, physically, as the electron concentration decreases, mobility saturates at a constant value which is determined by unscreened mobility. Note that the second term in equation (4.57) is independent of n and is a function of N_A only.

4.5.2 An Empirical Model for 3D Coulombic Scattering

For three dimensional Coulombic scattering, i.e. Coulombic scattering in the bulk, the model presented by Klaassen [34] is used. There are two types of Coulombic scattering that can occur in the bulk. Majority impurity scattering is the scattering of majority carriers by background dopants such as the scattering of electron by donors or of holes by acceptors. On the other hand, minority impurity scattering is that of minority carriers by dopant atoms. This for instance would include cases such as the scattering of electrons by acceptor atoms or the scattering of holes by donor atoms. Similarly, there are two types of Coulombic scattering in 2D. In the previous section Coulombic scattering in the inversion layer was discussed, which can also be considered as minority impurity scattering. In the next chapter, 2D Coulombic scattering in MOS accumulation layer (such as those that occur in the LDD regions of MOSFETs) would be considered and a model presented for majority impurity scattering in 2D.

The case most often treated in bulk is majority impurity scattering, since majority carriers are supplied by the background dopant atoms. Minority carrier scattering in 3D only becomes significant in situations that involve carrier injection, such as in the base of a bipolar transistor or in a p-n junction diode. Moreover, the models typically quoted for 3D majority impurity scattering also tacitly assume that the majority carrier concentration is equal to the density of the background dopants. While such an assumption is reasonable for majority carriers, the concentration of minority carriers is set by the degree of injection (or inversion in the case of 2D). Thus, for minority impurity scattering, it can no longer be assumed that minority carrier concentration is equal to the background dopant concentration. Summing the contributions due to majority and minority impurity scattering via the Matthiessen's rule, the total mobility due to Coulombic scattering in 3D can be written as:

$$\frac{1}{\mu_{coul}^{3D}} = \frac{1}{\mu_{3D,\,coul}^{minority}} + \frac{1}{\mu_{3D,\,coul}^{majority}} \tag{4.58}$$

As discussed, majority impurity scattering is a function of both the carrier concentration and the background dopant density. Hence, the expression for majority impurity scattering takes the following form [34]:

$$\mu_{3D,\,coul}^{majority} = \left(\frac{\mu_{max}^{2}}{\mu_{max}-\mu_{min}}\right)\left(\frac{N_{ref1}}{N_D}\right)^{\alpha_1}\left(\frac{T}{300}\right)^{3\alpha_1-\frac{3}{2}} + \left(\frac{\mu_{min}\mu_{max}}{\mu_{max}-\mu_{min}}\right)\left(\frac{n}{N_D}\right)\left(\frac{300}{T}\right)^{\frac{1}{2}} \tag{4.59}$$

The interaction of carriers with a constant perturbing potential is often treated in the Born approximation [70] which assumes that the kinetic energy of the carriers is large in comparison with the interaction potential. The Born approximation is a first order formulation of the time-dependent perturbation theory which does not distinguish between attractive and repulsive scattering potentials. Majority carriers scatter off an attractive potential whereas minority carriers scatter off repulsive potentials; hence, their mobilities are expected to be different. To calculate this difference, an alternative technique known as phase shift analysis [40], [71] is used. In this technique the scattered wave is treated as the sum of spherical waves whose phase shift with respect to the incident wave has changed due to the scattering process. Compared to the Born approximation, phase shift analysis is a more accurate technique, albeit computationally more expensive as well. The ratio of repulsive to attractive scattering cross section is the same as the ratio of majority to minority mobilities. Klaassen has modeled this ratio using a seventh-order spline function [34]:

$$\frac{\sigma_{rep}}{\sigma_{att}} \rightarrow \frac{\mu_{maj}}{\mu_{min}} = G(P) = 1 - \frac{s_1}{\left[s_2 + \left(\frac{m_o}{m}\frac{T}{300}\right)^{s_4} P\right]^{s_3}} + \frac{s_5}{\left[\left(\frac{m}{m_o}\frac{300}{T}\right)^{s_7} P\right]^{s_6}} \tag{4.60}$$

where P is a parameter that depends upon carrier concentration and temperature [34]:

$$P = \frac{1.36\times 10^{20}}{n}\left(\frac{m}{m_o}\right)\left(\frac{T}{300}\right)^2 \tag{4.61}$$

where m is the effective mass, m_o is the free electron mass, and T is the temperature of the electron gas. Therefore, mobility due to minority impurity scattering is obtained from the majority impurity scattering mobility given in equation (4.59) as:

$$\mu_{3D,\,coul}^{minority} = \frac{\mu_{3D,\,coul}^{majority}}{G(P)} \tag{4.62}$$

Equation (4.61) is derived using the Brooks-Herring approach [13], and it has a singularity at $n = 0$. To remove this effect, an expression which is independent of electron concentration is used. This approach was first used by Conwell and Weisskopf [12]. Thus, the resulting expression for P is a suitably weighted harmonic mean of the two approaches [34]:

$$\frac{1}{P} = \frac{2.459}{P_{CW}} + \frac{3.828}{P_{BH}} \tag{4.63}$$

where,

$$\begin{aligned} P_{BH} &= \frac{1.36\times 10^{20}}{n}\frac{m}{m_o}\left(\frac{T}{300}\right)^2 \\ P_{CW} &= 3.97\times 10^{13}\left[\frac{1}{N_A + N_D}\left(\frac{T}{300}\right)^3\right]^{\frac{2}{3}} \end{aligned} \tag{4.64}$$

At ultra high dopant concentrations, clustering becomes an important consideration. This is accounted for by replacing N_A with N_A^{clus} and N_D with N_D^{clus} according to the following transformations [34]:

$$\begin{aligned} N_A^{clus} &= \left[1 + \frac{1}{0.5 + \left(\frac{7.2\times10^{20}}{N_A}\right)^2}\right] N_A \\ N_D^{clus} &= \left[1 + \frac{1}{0.21 + \left(\frac{4\times10^{20}}{N_D}\right)^2}\right] N_D \end{aligned} \tag{4.65}$$

Klaassen [34] notes that Matthiessen's rule as used in equation (4.58) does not ensure that collision events between electrons and other scattering centers are truly two-body interactions. While equation (4.58) works well if either N_A or N_D dominates, in heavily compensated regions where the probability of interacting with either dopant types is equally likely, an approach similar to Conwell-Weisskopf [12] needs to be used in which the impact parameter for scattering is limited to half the average separation between scattering centers regardless of their type. Using this cut-off criterion, majority and minority mobilities can then be lumped together as [34]:

$$\mu_{coul}^{3D} = \mu_1 \left[\frac{N_A + N_D}{N_D + G(P)N_A}\right]\left(\frac{N_{ref1}}{N_A + N_D}\right)^{\alpha_1} + \mu_2 \left[\frac{n}{N_D + G(P)N_A}\right] \tag{4.66}$$

where,

$$\begin{aligned} \mu_1 &= \frac{\mu_{max}^2}{\mu_{max} - \mu_{min}}\left(\frac{T}{300}\right)^{3\alpha_1 - \frac{3}{2}} \\ \mu_2 &= \frac{\mu_{min}\mu_{max}}{\mu_{max} - \mu_{min}}\left(\frac{300}{T}\right)^{\frac{1}{2}} \end{aligned} \tag{4.67}$$

The numerical values for the parameters appearing in the model for 3D Coulombic scattering are shown in Table 4.1.

Table 4.1: Parameter set for 3D Coulombic Mobility

α_1	0.69
N_{ref1}	9.45×10^{16}
μ_{max}	1415.50
μ_{min}	60.3
m	$0.26m_o$
s1	0.89233
s2	0.41372
s3	0.19778
s4	0.28227
s5	0.005978
s6	1.80618
s7	0.72169

4.6 Semi-Empirical Modeling of the Universal Mobility Curve

It was experimentally shown by Sabnis and Clemens [43] that if the effective mobility of electrons in the inversion layer is plotted as a function of the effective transverse electric field in the inversion layer, the universal mobility curve is obtained which is independent of changes in oxide thickness, channel doping and back gate bias. Similar results were subsequently obtained by other researchers as well [33], [9], [76]-[79].

In the drift-diffusion formulation [7] of electron transport, the current density J is given by $qn\mu\nabla\varphi_n$. The drain current in the linear region then becomes

$$I_{ds} = \mu Q_{inv} W \frac{d\varphi_n}{dx} \tag{4.68}$$

In the linear region, $d\varphi_n/dx = V_{ds}/L$ if the drawn gate length is sufficiently large such that it is approximately equal to the metallurgical channel length. Other than that, there is no other approximation in the expression for $d\varphi_n/dx$ since the applied drain bias sets the boundary condition for the electrochemical potential φ_n as opposed to the electrostatic potential ψ [73], [74]. Hence, the mobility μ is obtained as:

$$\mu = \frac{I_{ds}}{V_{ds}} \cdot \frac{L}{WQ_{inv}(x)} \tag{4.69}$$

The problem with the expression in equation (4.69) is that due to the finite drain bias, inversion charge density becomes a function of x, the distance from source to drain. In the asymptotic limit of V_{ds} tending to zero, Q_{inv} becomes independent of x, and it is in this case that the effective mobility in the inversion layer can be defined as:

$$\mu_{eff} = \left.\frac{I_{ds}}{V_{ds}} \cdot \frac{L}{WQ_{inv}}\right|_{V_{ds} \to 0} \tag{4.70}$$

Sabnis and Clemens [43] extracted μ_{eff} using the definition in equation (4.70) by setting V_{ds} to around 10 to 30 mV. They also discovered that if μ_{eff} is plotted as a function of the surface transverse electric field E_{surf} , then the curves do not overlap if either channel doping or substrate bias is varied. It is only for the case when μ_{eff} is plotted as a function of E_{eff} that the curves overlap — the resulting curve is known as the universal mobility curve. Since the original work various researchers have confirmed the existence of the universal mobility curve. Sabnis and Clemens defined the effective field E_{eff} in the inversion layer as the average of the field at the top of the inversion layer (i.e. the surface field) and the field at the bottom of the inversion layer:

$$E_{eff} = \frac{E_{top} + E_{bottom}}{2} \tag{4.71}$$

From Gauss's law for electrostatics,

$$E_{top} = \frac{Q_{inv} + Q_{depl}}{\varepsilon_{si}}$$
$$E_{bottom} = \frac{Q_{depl}}{\varepsilon_{si}} \tag{4.72}$$

Hence, effective field takes on the following form [43]:

$$E_{eff} = \frac{1}{\varepsilon_{si}}\left[\frac{1}{2}Q_{inv} + Q_{depl}\right] \tag{4.73}$$

Other researchers have noted that E_{eff} can be defined more generally as:

$$E_{eff} = \frac{1}{\varepsilon_{si}}[\eta Q_{inv} + Q_{depl}] \tag{4.74}$$

It has been experimentally observed that while η=1/2 for (100) electrons [43], η=1/3 for (111) and (110) electrons [76], [11]. Lee *et. al.* [53] have shown that the difference in η values can be explained on the basis of valley repopulation of electrons.

An accurate way to determine integrated channel charge is by integrating the data obtained from gate-to-channel capacitance measurements [75], [95]:

$$Q_{inv}(V_{gs}) = \int_{-\infty}^{V_{gs}} C_{gc}(V_{gs})\,dV_{gs} \tag{4.75}$$

However, Sabnis and Clemens used a first-order simplification, which holds reasonably well in strong inversion. In the next section when we discuss the generalized mobility curve, it will be noted that near threshold, equation (4.75) deviates significantly from the simplified expression used by Sabnis and Clemens [43]:

$$Q_{inv} = C_{ox}(V_{gs} - V_T) \tag{4.76}$$

The larger V_{gs} is compared to V_T, the more accurate the expression in equation (4.76) is. If the channel profile is uniform in the depth direction, Q_{depl} is calculated from

$$\begin{aligned} Q_{depl} &= \sqrt{4q\varepsilon_{si}\phi_B N_{sub}} \\ \phi_B &= \frac{kT}{q}\ln\left(\frac{N_{sub}}{n_i}\right) \end{aligned} \tag{4.77}$$

Thus, E_{eff} can be determined from equations (4.73), (4.75), and (4.77).

Our approach to modeling the universal mobility curve is as follows:

(1) The model should be physically based and should reproduce all the properties of the universal mobility curve over a wide range of oxide thicknesses, channel dopings, and back gate bias;

(2) The model should be formulated in a completely local form since from a device simulation point of view, local models exhibit better numerical characteristics than non-local ones.

Lee *et. al.* [53] have shown that the experimentally observed universal mobility curve can be explained on the basis of phonon and surface roughness scattering. Thus a physically based model should contain both terms. Shin *et. al.* [32] present a model which builds on the work of Schwarz and Russek [29]. However, the major deficiency in both these works is that they only consider phonon scattering in the inversion layer. Moreover, these models are non-local in nature, which makes them less attractive for implementation in drift-diffusion device simulators such as PISCES [54] or PADRE [28]. While Shin *et. al.* attempt to present a transformation from a non-local formulation to a local one, the resulting model is actually a non-local one since it requires the computation of the electric field at the bottom of the inversion layer, which for a highly non-uniform doping profile requires a computation of the form:

$$E_{bottom} = \frac{Q_{depl}}{\varepsilon_{si}} = \frac{1}{\varepsilon_{si}} \cdot \int_{Z_{inv}}^{\infty} \left[N_D^+(z) - N_A^-(z)\right] dz \tag{4.78}$$

where Z_{inv} is the z-coordinate which marks the end of the inversion layer. Since the width of the depletion layer is much larger than the thickness of the inversion layer, in the above integration, Z_{inv} can be set to zero to obtain:

$$E_{bottom} = \frac{1}{\varepsilon_{si}} \cdot \int_0^{\infty} \left[N_D^+(z) - N_A^-(z) \right] dz \tag{4.79}$$

If coupled 2D process and device simulations need to be performed in which the output of the process simulator gives an arbitrary doping profile, calculation outlined in equation (4.79) would have to be performed. Thus, the model by Shin *et. al.*, in addition to lacking a term for surface roughness scattering, is also not a local model.

The model by Lombardi *et. al.* [30] provides a good starting point to model the universal mobility curve since: (a) it is physically based with a term for phonon and surface roughness scattering, and (b) it uses a local formulation. However, Lombardi's model suffers from the short coming that was discussed earlier on in Section 4.2: it is based on the formulation given in equation (4.1) which is not entirely physical. Moreover, in modern submicron devices, channel dopings in excess of 10^{17} cm^{-3} are fairly common, and hence any mobility model should be calibrated such as to include this range of doping. In the case of Lombardi's model it was found that while it reproduces the experimentally observed universal mobility curve for lower doping levels, it fails to follow the universal mobility curve for channel dopings in excess of 10^{17} cm^{-3}. This is shown in Figure 4.8 where the open circles represent experimental data at room temperature, and Lombardi's model is shown for three different channel doping levels. Ideally, Lombardi's model should follow the universal mobility curve for all three channel doping levels; the model clearly breaks down at higher channel doping levels. Lombardi's model was calibrated against experimental data that was obtained from MOSFETs whose channel doping levels varied from 5×10^{14} cm^{-3} to 1×10^{17} cm^{-3}. The model, being semi-empirical, cannot really be expected to yield good fits for parameters that fall outside the range of calibration. However, the degree to which semi-empirical models may be extended outside their range of calibration has to do with the degree of "physics" incorporated in the model. The new model overcomes this weakness that is present in the formulation of Lombardi's model.

It is observed in the next section that to model Coulombic scattering, it is imperative that the model should first reproduce the universal mobility curve for higher channel doping levels before the term for Coulombic scattering can be added. In light of the above shortcomings in Shin's and Lombardi's model, a physically-based semi-empirical local model for electron mobility is considered based on a more accurate physical formulation which also reproduces the properties of the universal mobility curve over a wide range of

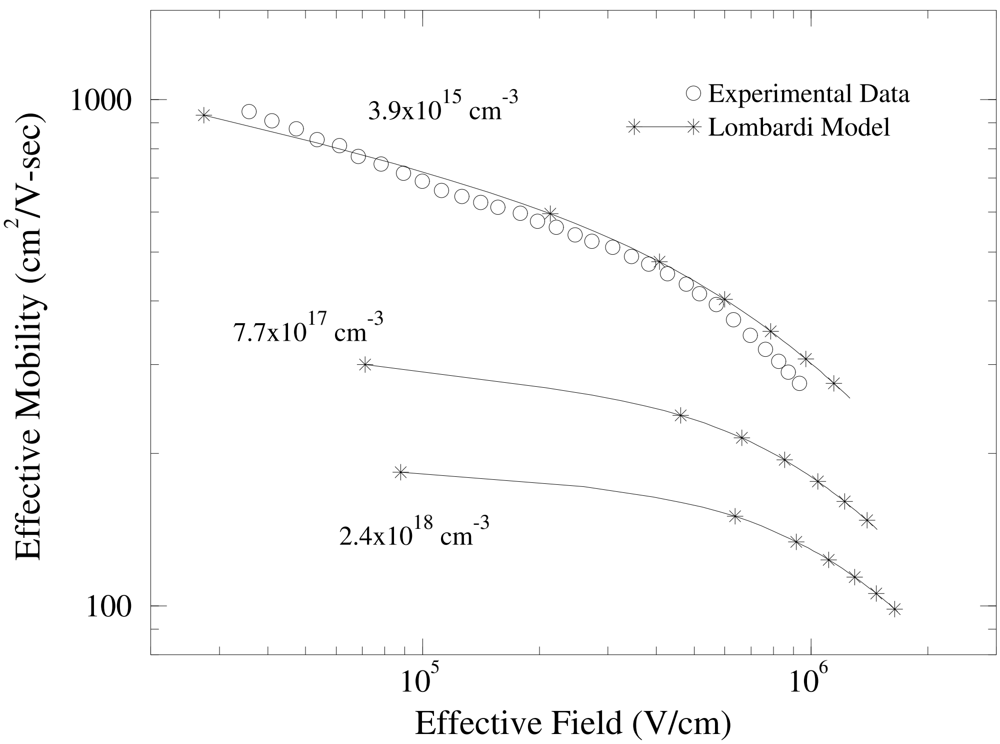

Figure 4.8 Comparison between Lombardi's model and experimental data for three different doping levels. Ideally, Lombardi's model should have followed the universal mobility curve shown by open circles for all three channel doping levels.

technology and bias conditions.

The semi-empirical terms for phonon, surface roughness and Coulombic scattering have been discussed extensively in Sections 4.3.3, 4.4.2, and 4.5.1 respectively. To model the universal mobility curve, we simply drop the term for Coulombic scattering in equation (4.2) to get:

$$\frac{1}{\mu_{umc}} = \frac{1}{\mu_{ph}} + \frac{1}{\mu_{sr}} \tag{4.80}$$

The model for phonon scattering appears in equation (4.30) and that for surface roughness scattering appears in equation (4.47). Since the model in equation (4.80) is a local one, the non-local effective mobility and non-local effective field need to be calculated in order to compare the new model with the experimentally-obtained universal mobility curve.

Within a drift-diffusion device simulator such as PISCES, the electrostatic potential ψ, the electron concentration *n*, and the hole concentration *p* are solved for at each node in the device for a certain applied bias at the electrodes. During the solution procedure, the mobility value is calculated at each node using the mobility model. The effective mobility can be calculated, as shown in equation (4.26), at the center of the channel (i.e. half way between the source and the drain) as a post-processing step using the information available within the device simulator at each node.

$$\mu_{eff}\left(\frac{L}{2}, V_{gs}, V_{bs}\right) = \frac{\int \mu_{umc}\left(\frac{L}{2}, z, V_{gs}, V_{bs}\right) \cdot n\left(\frac{L}{2}, z, V_{gs}, V_{bs}\right) dz}{\int n\left(\frac{L}{2}, z, V_{gs}, V_{bs}\right) dz} \tag{4.81}$$

where $\mu_{umc}(z)$ is supplied by the mobility model appearing in equation (4.80) and $n(z)$ is obtained from the device simulator via a self-consistent solution of Poisson and continuity equations. The functional dependence on V_{gs} and V_{bs} simply indicates that this calculation is performed each time either of the bias values change. Similarly, the effective electric field is obtained by integration, and is also calculated in the middle of the channel using equation (4.24):

$$E_{\perp, eff}\left(\frac{L}{2}, V_{gs}, V_{bs}\right) = \frac{\int E_{\perp}\left(\frac{L}{2}, z, V_{gs}, V_{bs}\right) \cdot n\left(\frac{L}{2}, z, V_{gs}, V_{bs}\right) dz}{\int n\left(\frac{L}{2}, z, V_{gs}, V_{bs}\right) dz} \tag{4.82}$$

where $E_{\perp}(z) = -[\nabla\psi \cdot \hat{z}]$.

Calibration of the model is performed in a step-wise manner. The experimentally obtained universal mobility curve has two distinct regimes: a low field regime in which the slope ~ 1/3, and a high field regime in which the slope ~ 2. It is thus realized that the phonon scattering term which goes as $E^{-0.33}$ dominates at low and moderate electric fields, whereas the surface roughness term which goes as E^{-2} dominates at high fields. The results of the calibration procedure are shown in Table 4.2 . One striking feature in Table 4.2 is that except for parameter *A*, the agreement between the new model and the first-principles calculation is *better* than the agreement between Lombardi's model and the first-principles calculation. In particular, the parameters *B* and γ in the new model are one

Table 4.2: Parameter set for the new Local-Universal Mobility Model

Parameter	Lombardi's Model	New Model	First-Principles' calculation values
A	4.75×10^7	9.0×10^5	3×10^8
B	1.74×10^5	1.32×10^6	3×10^7
γ	0.125	0.057	0
C		3.97×10^{13}	
$\delta = CN_A^{\gamma}$	5.82×10^{14}	3.0×10^{14}--4.4×10^{14}	2.83×10^{15}

order of magnitude closer to the first-principle's value than Lombardi's model. The fact that these parameters are closer to the theoretical values implies that the new formulation given in equation (4.2) exhibits a physical consistency.

With the values appearing in Table 4.2, the new model reproduces the universal mobility curve over a wide range of channel doping levels as shown in Figure 4.9. Here the doping level is varied about three orders of magnitude from 3.9×10^{15} to 2.4×10^{18} cm^{-3}, and excellent fits are obtained between the new model and experimental data. In contrast with Lombardi's model, the new model follows the universal mobility curve very well.

The other important property of the universal mobility curve [33], [43] is its invariance to changes in oxide thickness and back gate bias. In Figure 4.10, both variations are shown separately. First, oxide thickness is kept constant at 250 Å, and back gate bias is varied from 0 to -5 volts. In this case, the two curves represented by a solid line and a dashed one are seen to overlap. Then, back gate bias is kept constant at zero volts, and oxide thickness is varied from 250 to 500 Å. In this case as well, the curves overlap.

4.7 Semi-Empirical Modeling of the Generalized Mobility Curve

It was first reported by Takagi *et. al.* [9] that at high channel doping levels, marked deviations are observed from the universal mobility curve at low carrier concentrations

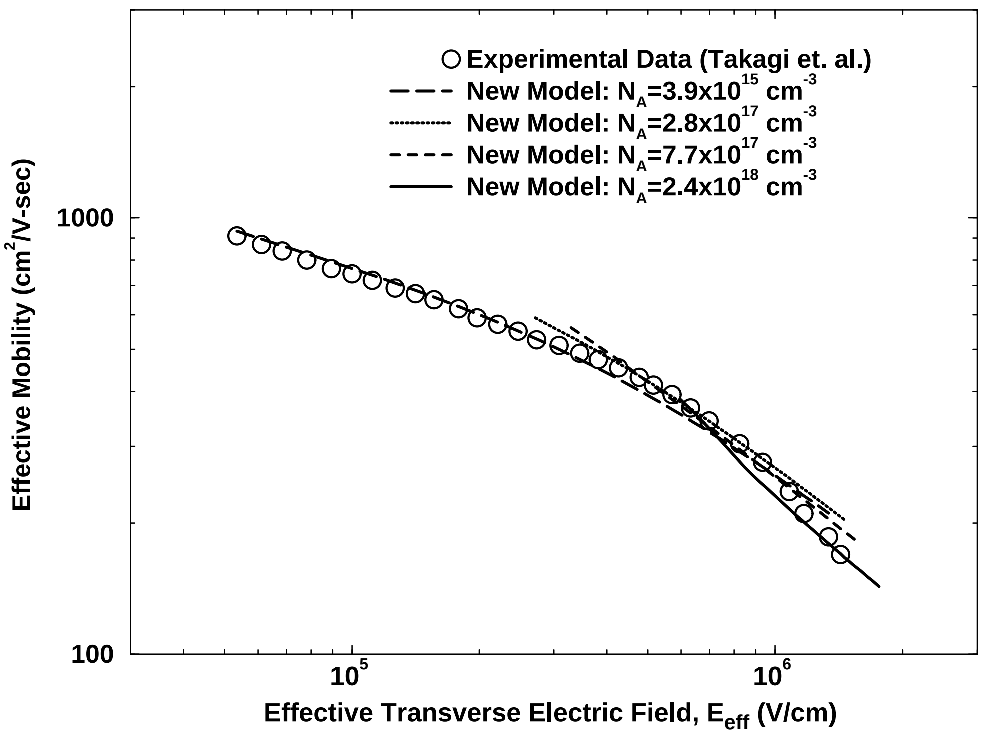

Figure 4.9 Comparison between the new model and the experimental universal mobility curve obtained by Takagi *et. al.* [9]. The new model exhibits excellent fits as channel doping is varied over three orders of magnitude.

(i.e. at low transverse effective fields). They attributed these deviations from universality as being due to increased Coulombic scattering owing to large number of dopant atoms in the channel. Other researchers have obtained similar experimental results which also indicate that increased impurity scattering causes significant reduction of mobility near the threshold region of operation [53], [80], [81]. These deviations are concentrated near the region where the gate voltage is close to the threshold voltage. For voltages much greater than V_T , the deviations disappear, and the universal mobility curve behavior is restored. Since, Coulombic scattering has only a partial effect on the universal mobility curve, we term the resulting curves as the *generalized mobility curves*. A set of experimentally obtained generalized mobility curves are shown in Figure 4.11.

It's well known that at low temperatures, Coulombic scattering becomes important in semiconductors [8], while at room temperature phonon scattering is dominant. The results obtained by Takagi *et. al.* [9] however indicate that even at room temperature,

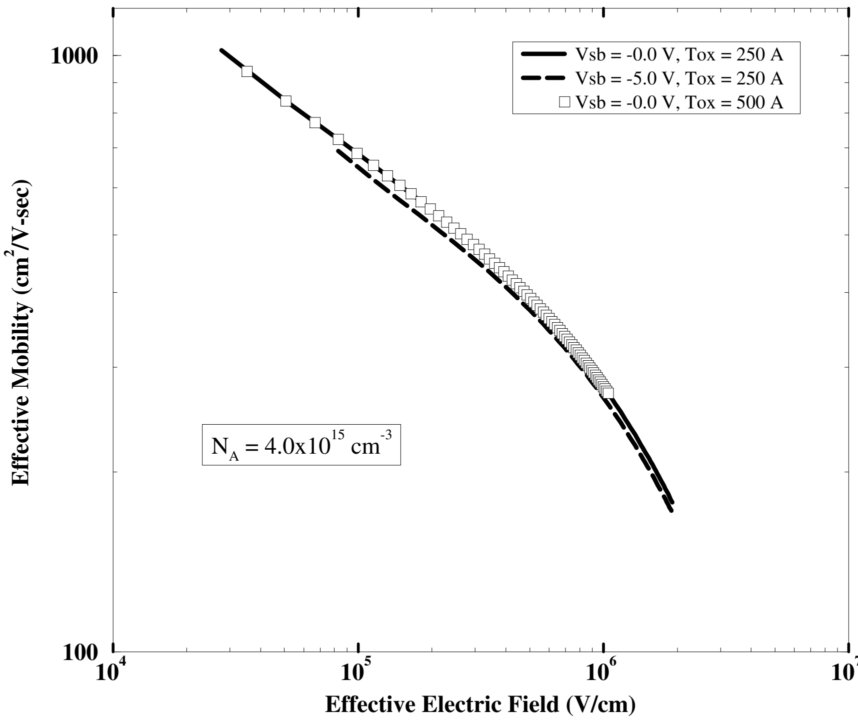

Figure 4.10 Universal mobility curves obtained from the new model in equation (4.80) remain invariant to changes in oxide thickness and back gate bias.

Coulombic scattering is important if the number of Coulombic scattering centers is extremely large. Thus, the reason why the universal mobility curve was observed by Sabnis and Clemens [43] and by other researchers is that the MOSFET devices they considered had low substrate dopings.

A detailed theoretical analysis for Coulombic scattering was presented in the previous chapter. There it was observed that Coulombic scattering is really a function of the integrated channel charge, N_{inv}, and not of the effective electric field, E_{eff}. However, the universal mobility relationship is between effective mobility and effective field. Hence, when Coulombic scattering dominates, it is not expected to follow the universal mobility curve, as observed experimentally in Figure 4.11.

Since Coulombic scattering causes a deviation from the universal mobility curve, the starting point for modeling purposes would be an accurate model for the universal

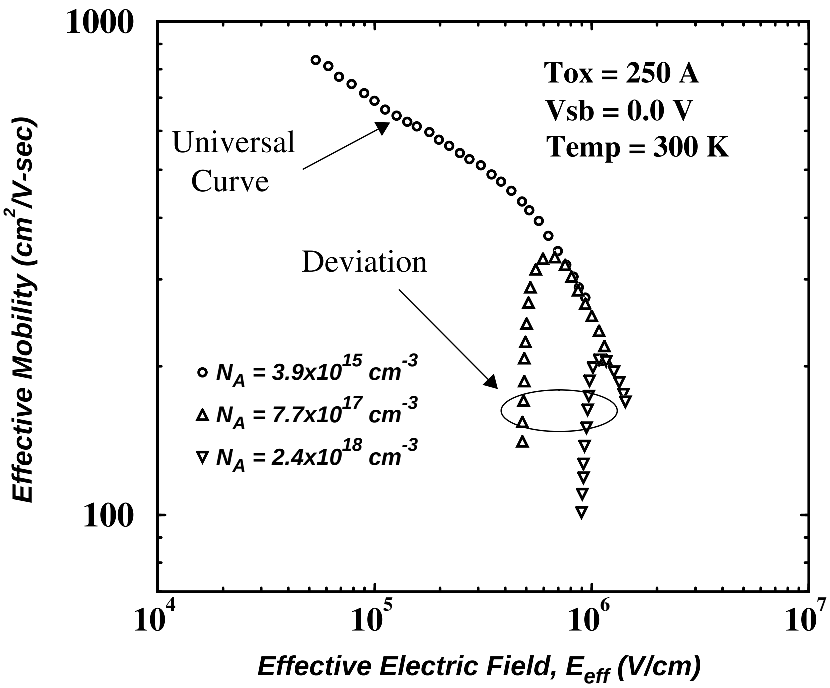

Figure 4.11 The generalized mobility curve shown here is the one that results when Coulomb scattering due to channel dopants causes deviations from the universal mobility behavior.

---

mobility curve. Such a model (equation (4.80)) was presented in Section 4.6. In this section, the model is extended to account for the deviations from the universal mobility curve. The extended formulation was discussed earlier in Section 4.2, and the resulting equation includes the terms for Coulombic, phonon, and surface roughness scattering (see equation (4.2)). In Section 4.6, phonon and surface roughness scattering models were used for purposes of modeling the universal mobility curve. In this section, the Coulombic scattering model, primarily developed in Section 4.5, would be invoked to model the generalized mobility curve shown in Figure 4.11. For Coulombic scattering, the principal equation is given by (4.55):

$$\mu_{coulomb} = f(\alpha) \cdot \mu_{3D}^{coulomb} + [1 - f(\alpha)] \cdot \mu_{2D}^{coulomb} \tag{4.83}$$

Here, $f(\alpha)$ is given by equation (4.54), where $\alpha = \Delta\varepsilon / kT$ is given by equation (4.53). The model for 2D Coulombic scattering is specified by equation (4.57), and the model for 3D

Coulombic scattering appears in equations (4.63)-(4.67).

Shin *et. al.* [80] have presented a model for electrons that includes Coulombic scattering due to ionized channel impurities as well. However, this model [80] is based on their earlier work [32], which as argued in Section 4.6 has the weakness of not being a local model. Hence, it is not the most suitable model for implementation in device simulators. Moreover, the model used for Coulombic scattering in their work [80] is based directly on the well-known Brooks-Herring model [13], which was formulated for a three dimensional electron gas. While they have included sufficient number of calibrating parameters to fit Brooks-Herring model with experimental data, this approach is unnecessary in light of the simple model presented in Section 4.5.1 for 2D Coulombic scattering. Finally, Shin *et. al.* overlook an important term in their model for Coulombic scattering — the unscreened mobility term. Their model has a numerical singularity at low electron concentrations, which is prevented by the unscreened term in equation (4.57).

Shirahata *et. al.* [82] have also proposed a model for inversion layer electrons that includes Coulombic scattering. However, this approach is purely empirical with little physical basis. Moreover, the scattering mechanisms have not been partitioned in a physical fashion as presented in equation (4.2). In the next chapter, equation (4.2) provides an essential starting point for extending the inversion layer mobility model to accumulation layers. A significant drawback with Shirahata's model is that it provides no means to enforce mutual exclusivity (discussed in Section 4.2). Hence, it cannot be extended to model accumulation layers. Equally important, Shirahata's model also omits the term for unscreened Coulombic scattering, which results in a numerical singularity when the electron concentration goes to zero.

The model presented for 2D Coulombic scattering in equation (4.57) derives its physical basis from the theoretical analysis presented in the previous chapter. It is fully local in nature and remains bounded in the asymptotic limit of electron concentration going to zero.

Defining the total model as μ_{gmc}, it is given by the equation appearing in (4.2):

$$\frac{1}{\mu_{gmc}} = \frac{1}{\mu_{umc}} + \frac{1}{\mu_{Coul}} \tag{4.84}$$

where μ_{umc} is given by equation (4.80) and μ_{Coul} is given by equation (4.83). Figure 4.12

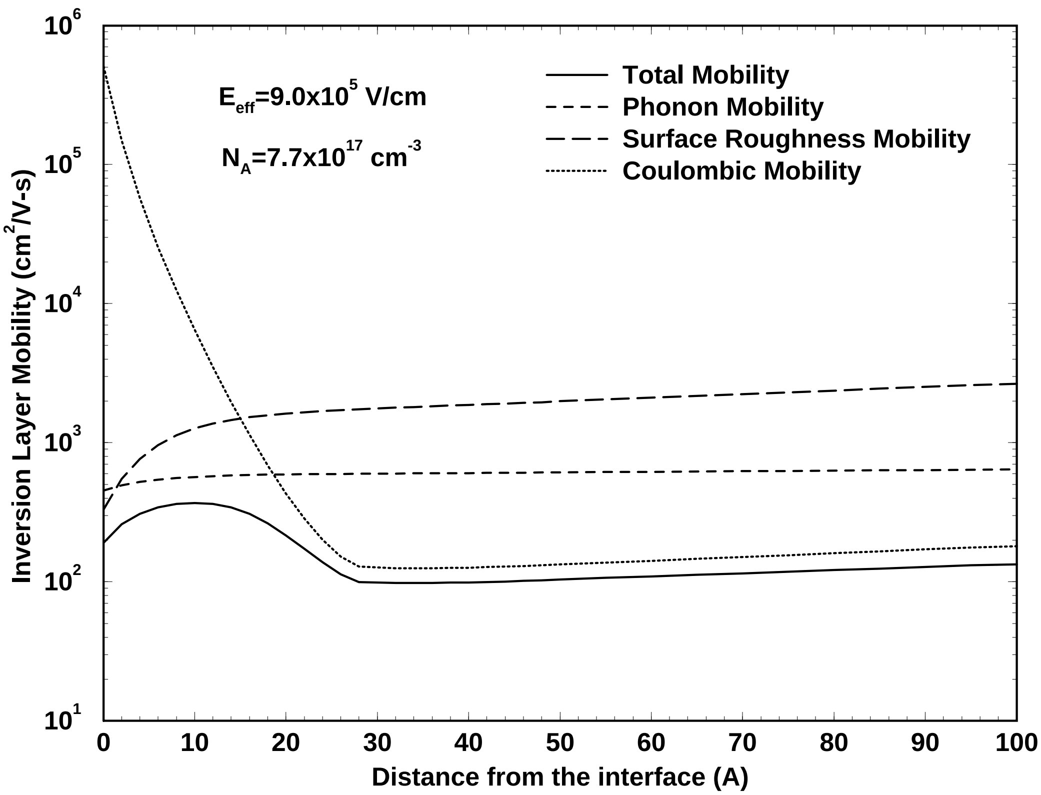

Figure 4.12 Variation of total mobility with distance from the interface for a MOSFET biased in strong inversion. The cross section is taken at the center of the channel.

---

shows how μ_{gmc} varies with distance from the interface for a particular device (N_A = 7.7x10^{17} cm^{-3}) biased in strong inversion (E_{eff} = 9.0x10^5 V/cm). Away from the interface, the mobility initially increases because phonon and surface roughness mobilities are increasing. The mobility then peaks and starts decreasing as Coulombic mobility takes over. Coulombic mobility decreases away from the interface because of a decrease in carrier concentration. As shown in Fig. 4.13, Coulombic mobility near the interface is dominated by the 2D term, whereas further away from the interface, the 3D term dominates.

Calibration of equation (4.84) essentially requires the calibration of μ_{Coul} since calibration of μ_{umc} was performed in the previous section. For μ_{Coul}, it is really 2D Coulombic scattering that needs to be calibrated as given in equation (4.57); the 3D

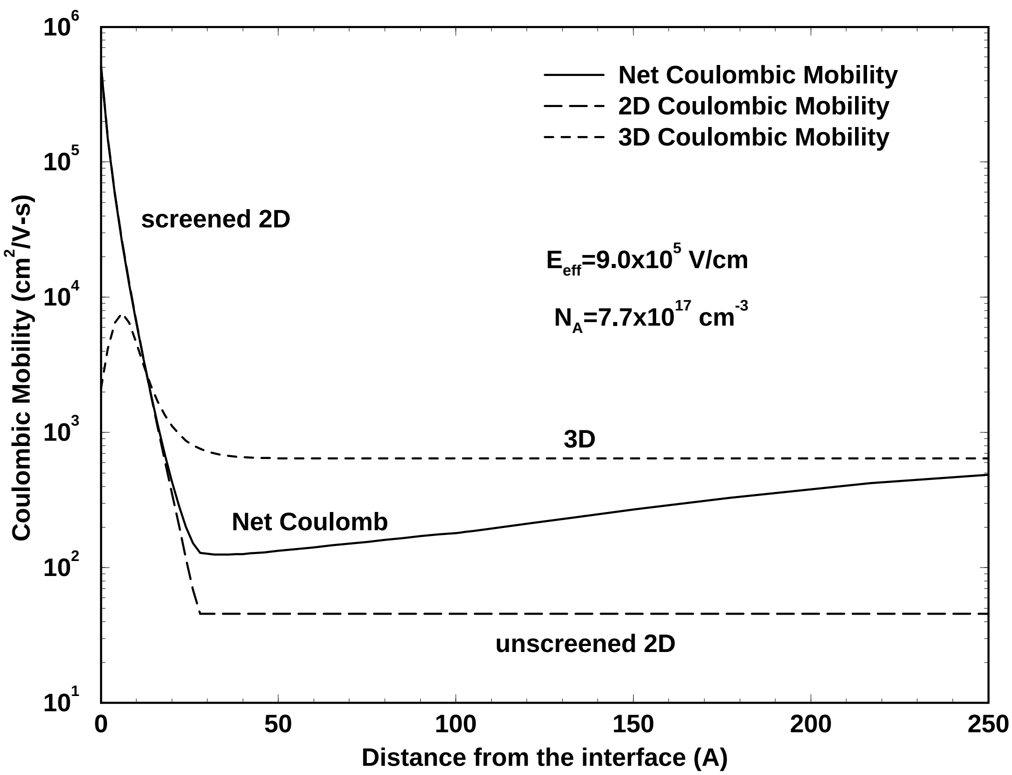

Figure 4.13 Variation of Coulombic mobility with distance from the interface for a MOSFET biased in strong inversion. The cross section is taken at the center of the channel.

Coulombic scattering model has already been calibrated to bulk data [34]. Since the model appearing in equation (4.84) is local, the non-local effective mobility is obtained in a similar fashion as the non-local μ_{umc} was obtained in equation (4.81):

$$\mu_{eff}\left(\frac{L}{2}, V_{gs}, V_{bs}\right) = \frac{\int \mu_{gmc}\left(\frac{L}{2}, z, V_{gs}, V_{bs}\right) \cdot n\left(\frac{L}{2}, z, V_{gs}, V_{bs}\right) dz}{\int n\left(\frac{L}{2}, z, V_{gs}, V_{bs}\right) dz} \tag{4.85}$$

Effective transverse electric field, E_{eff}, is determined in the middle of the channel using equation (4.82).

The calibration of μ_{gmc} is a two step process: first, parameters appearing in equation

(4.57) for μ_{Coul}^{2D} are perturbed, and then μ_{eff} is calculated using equation (4.85). This process is repeated until a good match with experimental data (shown in Fig. 4.11) is obtained. The results of this calibration procedure are presented in Table 4.3. It should be

Table 4.3: Parameter set for the 2D Coulombic Scattering Model

D_1	1.35×10^{11}
α	1.5
β_1	2.0
D_2	4.0×10^{10}
β_2	0.5

mentioned that the procedure described above calibrates the screened part of μ_{Coul}^{2D}; the unscreened part is calibrated against the data whose extraction was presented in Section 3.5.

With this parameter set, the comparison between the new model and the experimental generalized mobility curve is shown in Figure 4.14. Excellent agreement is obtained between the new model and experimental data over a wide range of channel doping levels.

The effect of back-gate bias on the GMC is to primarily shift the mobility roll-off point which directly corresponds to the threshold voltage. As shown in Fig. 4.15, the new model exhibits excellent agreement with experimental data over a wide range of back-gate bias.

It was discussed in Section 3.3 that screening due to free carriers is stronger in 3D compared to 2D, because of which Coulombic mobility in 3D is higher than that in 2D. This result was observed both experimentally and theoretically in Figure 3.2 in which μ_{eff} is plotted as a function of N_{inv}. Similar results are also observed in Figure. 4.16 which is a plot of μ_{eff} versus E_{eff}. As can be seen from Figure 4.16, the Brooks-Herring model needs to be “calibrated” for both magnitude and screening dependence in order to fit experimental data [80].

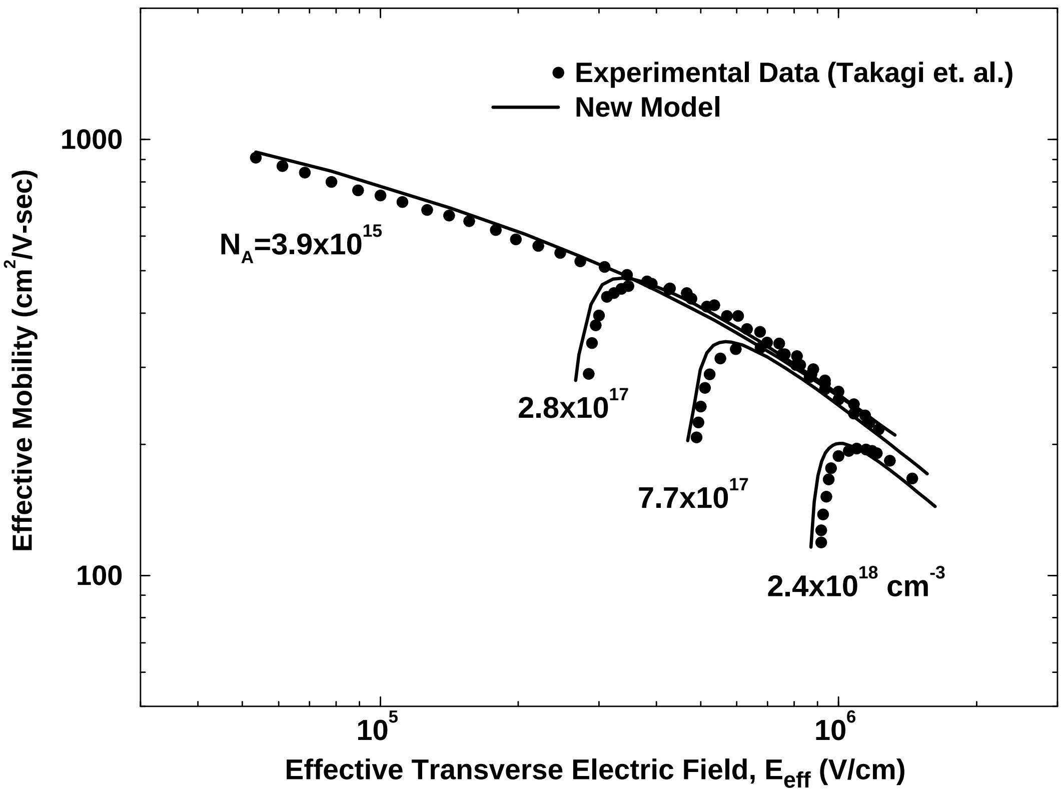

Figure 4.14 Comparison between the simulated generalized mobility curve obtained from the new local model (see equation (4.84)) and the experimental generalized mobility curve obtained by Takagi *et. al.* [9].

4.8 Summary

In this chapter, a physically-based semi-empirical local mobility model for inversion-layer electrons is presented that includes terms due to phonon, surface roughness, and Coulombic scattering. It is demonstrated that the new model reproduces all the properties of the universal and the generalized mobility curve over a wide range of technology and bias conditions. The new model has been formulated in local terms since that is the preferred form of implementation in drift-diffusion devices simulators such as PISCES. A summary of the numerical formulation of the model is presented below.

In the new model, the three scattering mechanisms are combined together in a physically correct fashion that ensures mutual-exclusivity:

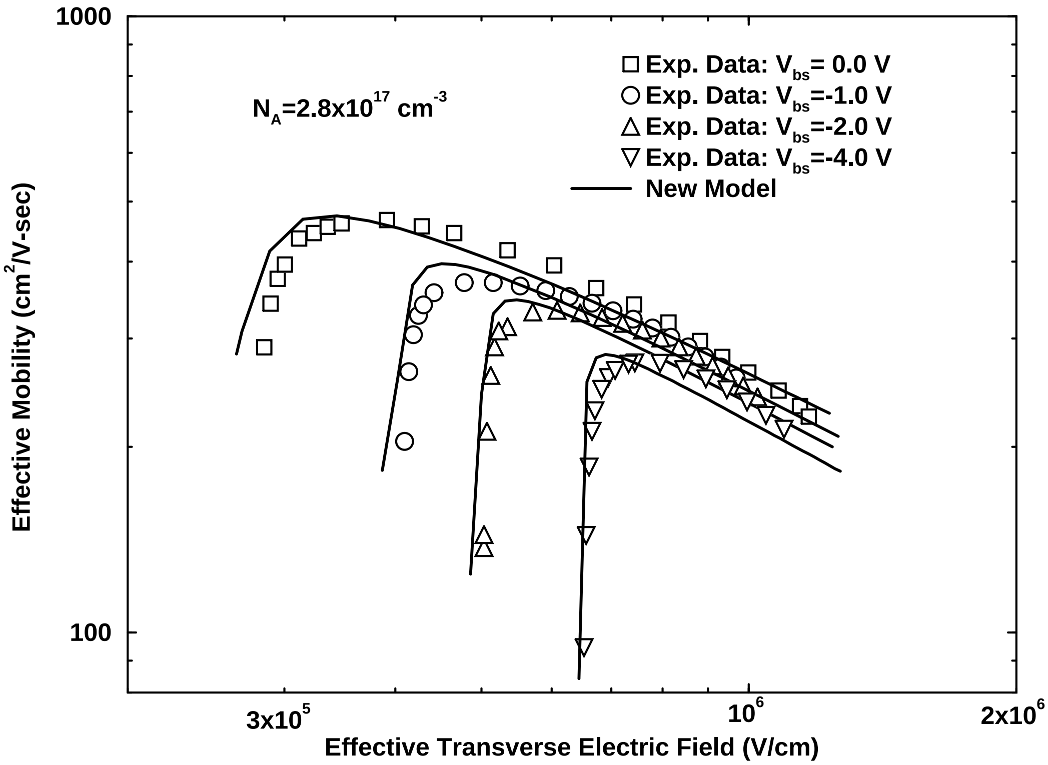

Figure 4.15 Comparison between simulated and experimental [96] generalized mobility curves over back gate bias.

$$\frac{1}{\mu_{total}} = \frac{1}{\mu_{phonon}} + \frac{1}{\mu_{surface\ roughness}} + \frac{1}{\mu_{Coulomb}} \tag{4.2}$$

The model for phonon scattering consists of a 2D and a 3D term. The semi-empirical model for 2D phonon scattering is obtained from a first-principles analysis, whereas an empirical model is used for 3D phonon scattering. Phonon mobility is given by:

$$\mu_{ph} = \boldsymbol{min}\left[\frac{A}{E_{\perp}(\boldsymbol{r})} + \frac{B \cdot N^{\gamma}{}_A}{T \cdot E_{\perp}^{1/3}(\boldsymbol{r})}, \mu_{max}\left(\frac{300}{T}\right)^{\theta}\right] \tag{4.30}$$

where $\theta = 2.285$, N_A is the acceptor density and $E_{\perp}$ is the local transverse electric field. Other parameters appearing in equation (4.30) are given in Tables 4.1 and 4.2. Surface roughness scattering is a 2D effect and its semi-empirical model is obtained from a

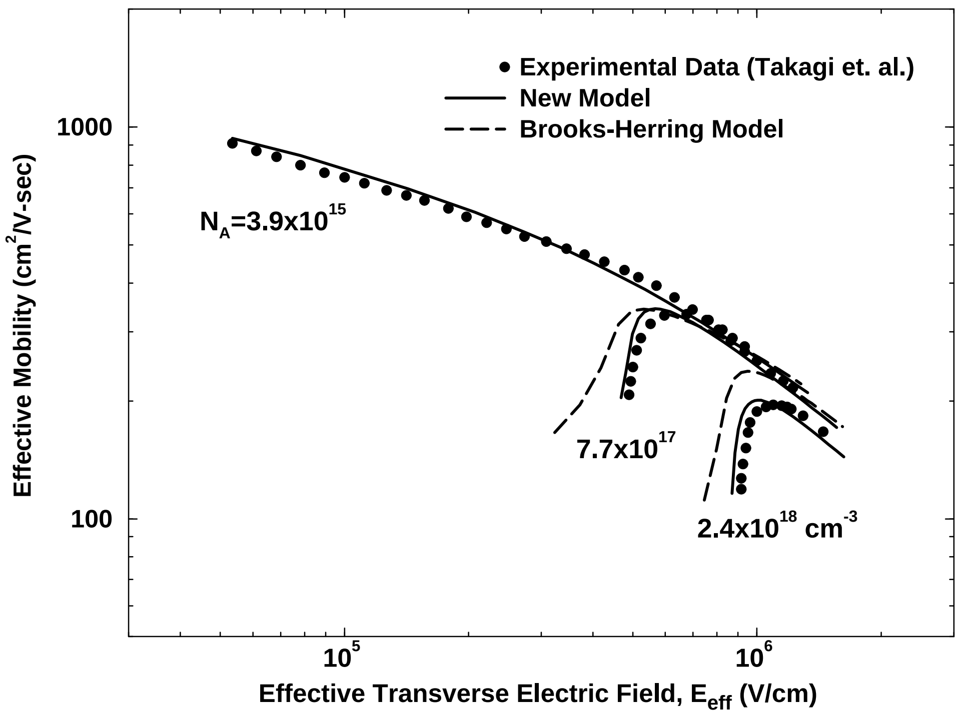

Figure 4.16 Comparison between the new 2D model for Coulombic scattering (see equation (4.57)) and the 3D Brooks-Herring model [13]. B-H model is seen to over-predict mobility since screening is stronger in 3D compared to 2D.

first-principles calculation as:

$$\mu_{sr} = \frac{C \cdot N_A^{\gamma}}{E_{\perp}^2(\boldsymbol{r})} \tag{4.48}$$

The parameter appearing in equation (4.47) is given in Table 4.2. In the case of Coulombic scattering, the 2D and the 3D terms are combined together via a transition function *f*(α*)* as:

$$\mu_{coulomb} = f(\alpha) \cdot \mu_{3D}^{coulomb} + [1 - f(\alpha)] \cdot \mu_{2D}^{coulomb} \tag{4.55}$$

where,

$$f(\alpha) = \frac{1}{1 + e^{(\alpha - \lambda)/\eta}} \tag{4.54}$$

and $\lambda = 2$ and $\eta = 1/2$. The parameter α is calculated from the local transverse electric field as:

$$\alpha = \frac{2.1\times 10^{-24} \cdot E_{\perp}^{2/3}}{kT} \tag{4.53}$$

The semi-empirical formulation for 2D Coulombic mobility considers both screened and unscreened scattering, and is obtained from a first-principles calculation as:

$$\mu_{coul}^{2D} = max\left[\left(D_1 \frac{n^{\kappa}}{N_A^{\beta_1}}\right), \left(\frac{D_2}{N_A^{\beta_2}}\right)\right] \tag{4.57}$$

The empirical model for 3D Coulombic scattering consists of both majority and minority impurity scattering, and is given as:

$$\mu_{coul}^{3D} = \mu_1\left[\frac{N_A + N_D}{N_D + G(P)N_A}\right]\left(\frac{N_{ref1}}{N_A + N_D}\right)^{\alpha_1} + \mu_2\left[\frac{n}{N_D + G(P)N_A}\right] \tag{4.66}$$

where,

$$\begin{aligned} \mu_1 &= \frac{\mu_{max}^2}{\mu_{max} - \mu_{min}}\left(\frac{T}{300}\right)^{3\alpha_1 - \frac{3}{2}} \\ \mu_2 &= \frac{\mu_{min}\mu_{max}}{\mu_{max} - \mu_{min}}\left(\frac{300}{T}\right)^{\frac{1}{2}} \end{aligned} \tag{4.67}$$

The *G(P)* term accounts for the fact that electrons scatter differently from attractive and repulsive potentials, and it is modeled as a seventh-order spline function:

$$G(P) = 1 - \frac{s_1}{\left[s_2 + \left(\frac{m_o}{m}\frac{T}{300}\right)^{s_4} P\right]^{s_3}} + \frac{s_5}{\left[\left(\frac{m}{m_o}\frac{300}{T}\right)^{s_7} P\right]^{s_6}} \tag{4.60}$$

where *P* is a screening parameter that is obtained as:

$$\frac{1}{P} = \frac{2.459}{P_{CW}} + \frac{3.828}{P_{BH}} \tag{4.63}$$

and,

$$\begin{aligned} P_{BH} &= \frac{1.36\times10^{20}}{n}\frac{m}{m_o}\left(\frac{T}{300}\right)^2 \\ P_{CW} &= 3.97\times10^{13}\left[\frac{1}{N_A+N_D}\left(\frac{T}{300}\right)^3\right]^{\frac{2}{3}} \end{aligned} \tag{4.64}$$

For ultra high dopant concentration, clustering becomes an important consideration. This is accounted for by replacing N_A with N_A^{clus} and N_D with N_D^{clus} everywhere in the 3D model for Coulombic scattering. The clustering transformations are given by:

$$\begin{aligned} N_A^{clus} &= \left[1 + \frac{1}{0.5 + \left(\frac{7.2\times10^{20}}{N_A}\right)^2}\right]N_A \\ N_D^{clus} &= \left[1 + \frac{1}{0.21 + \left(\frac{4\times10^{20}}{N_D}\right)^2}\right]N_D \end{aligned} \tag{4.65}$$

The parameters for Coulombic scattering appear in Tables 4.1 and 4.3.

Chapter 5

A Unified Model for Inversion and Accumulation Layer Electrons

5.1 Introduction

An important metric characterizing the performance of MOSFETs for digital applications is I_{on} which is defined as I_{ds} under conditions of maximum bias at both the gate and drain electrodes (i.e. $V_{gs} = V_{ds} = V_{dd}$). If we define the total MOSFET resistance as V_{ds}/I_{on} , then it can be viewed as the sum of an intrinsic and an extrinsic part:

$$R_{tot} = R_{int} + R_{ext} \tag{5.1}$$

where R_{int} corresponds to the channel (i.e. inversion-layer) resistance and R_{ext} corresponds to all parasitic resistances appearing in the device. For velocity saturated MOSFETs [5], the expression for channel resistance can be written as:

$$R_{int} = \frac{\left[(V_{dd} - V_T) + \frac{\upsilon_{sat} L_{met}}{\mu_{eff}} \right] T_{ox}}{W_{eff} \upsilon_{sat} \varepsilon_{ox} V_{dd} (V_{dd} - V_T)^2} \tag{5.2}$$

where υ_{sat} is the saturation velocity of carriers in the inversion layer, L_{met} is the length of the channel measured from the source-channel metallurgical junction to the drain-channel metallurgical junction, T_{ox} is the oxide thickness, and other symbols take on their usual meaning. It can be seen from equation (5.2) that reduction in oxide thickness has a bigger impact on channel resistance than reduction in channel length. Since, both parameters are reduced in MOSFET scaling, the result is a significant reduction in channel resistance despite the onset of velocity saturation.

At the same time, limitations imposed by hot-carrier reliability severely restrict the degree to which the parasitic resistance appearing in the LDD region of a MOSFET can be reduced [19]. As a result, channel resistance in scaled MOSFETs has been decreasing at a faster rate than parasitic resistance. While in long channel MOSFETs, the total resistance between the source and drain contacts is dominated by the inversion-layer component, in submicron MOSFETs, parasitic resistance has become a significant fraction of the total resistance. Therefore, to accurately predict the I-V characteristics of such devices, it has become imperative to take into account the degradation caused by the LDD parasitic resistance [3]. Realizing its importance, much work has been reported on the analytical modeling of the parasitic source-drain series resistance for both LDD [24]-[26] and non-LDD MOSFETs [20]-[23].

In the previous chapter, a semi-empirical mobility model was presented that incorporated the important scattering mechanisms operating in the inversion layer. While the accumulation layer in the LDD region of a MOSFET is similar in many respects to the inversion layer in the channel, certain fundamental differences exist because of which the nature of some of the scattering mechanisms is different in the accumulation layer. Hence, it cannot be expected of a mobility model calibrated for the inversion layer to be able to correctly calculate mobility in the accumulation layer.

In this chapter, a unified model for inversion and accumulation layer electrons is presented that builds on the model presented in the previous chapter. The new model is semi-empirical and local in nature. A systematic simulation methodology for deep submicron LDD MOSFETs based on the new mobility model is presented, and it is shown to produce excellent agreement with experimental data over a wide range of bias conditions (subthreshold, linear, and saturation) and channel lengths down to 0.25μm.

The organization of this chapter is as follows. In Section 5.2, the impact of LDD resistance in various deep submicron technologies is evaluated through coupled 2D process and device simulations. In Section 5.3, problems with existing simulation methodologies are discussed, and in Section 5.4 a systematic simulation methodology requiring the use of accumulation-layer mobility models is proposed. In Section 5.5, a unified model for accumulation and inversion layer electrons in presented. This model builds on the work presented in the previous chapter which was concerned with the modeling of the generalized mobility curve. In Section 5.6, comparison between simulation and measurement results is presented for a 0.25µm technology. Excellent fits are obtained over a wide range of channel lengths and terminal biases. Conclusions are presented in Section 5.7.

5.2 Parasitic resistance in submicron LDD MOSFETs

Figure 5.1 is a schematic illustration of the various components contributing to parasitic series resistance in an LDD MOSFET, namely: (i) the resistance beneath the contact window, (ii) the sheet (diffusion) resistance of the source/drain and LDD regions where the current flow is laminar, (iii) the spreading resistance in the vicinity of the gate edge where current crowding/spreading takes place, and (iv) the accumulation-layer resistance occurring in the overlap region between the gate and the LDD region [24].

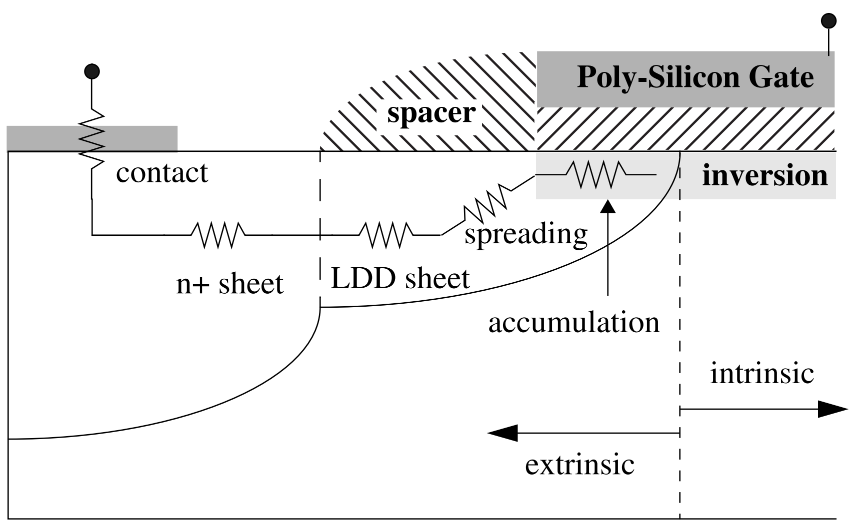

Figure 5.1 Schematic cross-section of one half on an LDD MOSFET. The various components of the extrinsic resistance are shown.

To asses the magnitude of the voltage drop in the extrinsic region of the device, coupled 2-D process and device simulations of a realistic 0.25µm technology [37] were performed using the process simulator PROPHET [27] and the device simulator PADRE

[28]. In Figure 5.2, the doping profile obtained from PROPHET simulations and the corresponding electron density in strong inversion obtained from PADRE simulations is shown along the Si/SiO_2 interface of a 0.25μm MOSFET. In the example shown, arsenic is used as the dopant for the LDD region. For this case, note that 75% of the coded gate length falls within the intrinsic region of the device, which is defined as the region from source-channel metallurgical junction to drain-channel metallurgical junction.

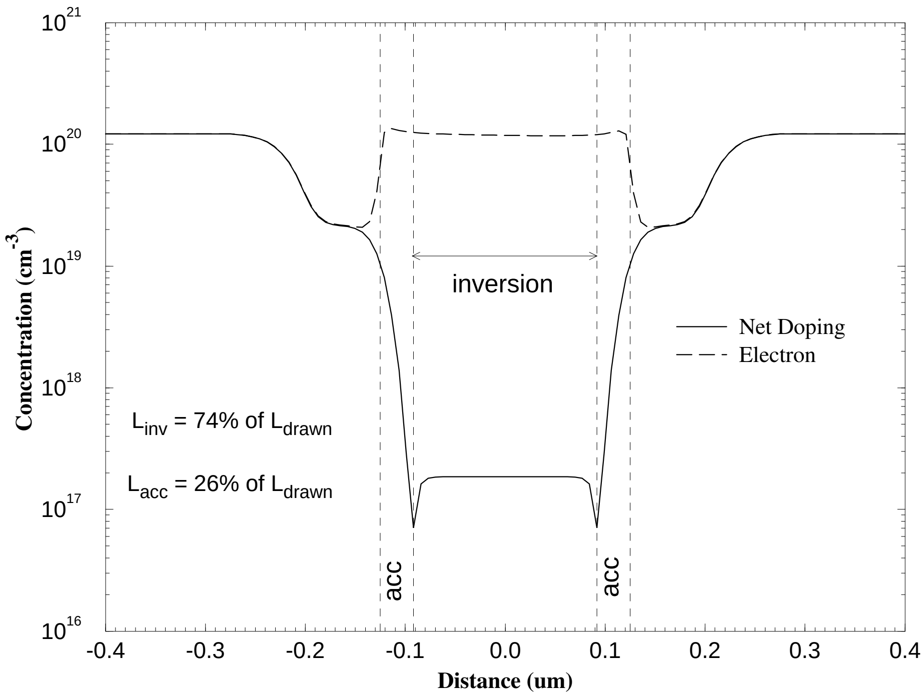

Figure 5.2 Doping and electron concentration profile in strong inversion for a 0.25μm As-LDD MOSFET.

To get an indication of the resistance in various regions of the device, the quasi-fermi level is plotted along the Si/SiO_2 interface. From conventional drift-diffusion theory of electron transport in semiconductors [7], the current per unit width in the device is given by:

$$I_{DS} = \int_{o}^{\infty} J(y)\,dy = \frac{d}{dx}\varphi_n(x) \cdot \int_{o}^{\infty} qn(x,y)\,\mu(x,y)\,dy = \frac{\frac{d}{dx}\varphi_n(x)}{R_{sheet}(x)} \tag{5.3}$$

where x is the direction parallel to the interface, y is the direction perpendicular to the interface, and φ_n is the electron quasi-fermi level. Due to current continuity, I_{DS} is independent of x, and hence the sheet resistance is simply proportional to the lateral gradient of $\varphi_n(x)$.

Figure 5.3 is a plot of $\varphi_n(x)$ and $d\varphi_n/dx$ along the Si/SiO_2 interface of the device whose doping profile is shown in Figure 5.2. 40% of the voltage drop is in the extrinsic

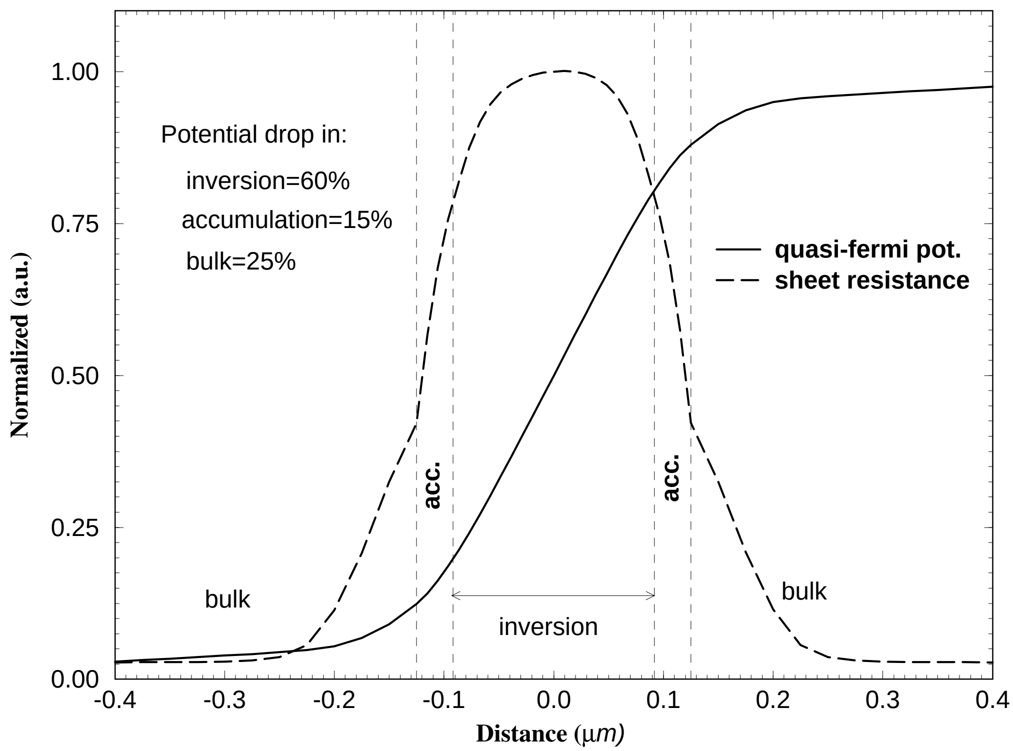

Figure 5.3 Quasi-Fermi potential drop along the Si/SiO_2 interface of a 0.25μm As-LDD MOSFET in strong inversion. The drain bias is 100mV and the gate bias is 2.5V; hence the device is operating in the linear region. Although 60% of the total resistance is due to the channel, a significant portion (40%) comes from the extrinsic region. The extrinsic resistance is primarily due to accumulation layer resistance and spreading resistance.

region, of which 15% corresponds to the accumulation layer. This significant voltage drop in the extrinsic region is due to the fact that the sheet resistance in the accumulation layer and in the current-crowding/spreading region is comparable to the sheet resistance in the inversion layer (see Fig. 5.3).

As another example, consider a 0.25μm MOSFET in which the LDD is doped with phosphorus instead of arsenic. As shown in Fig. 5.4, due to the higher diffusivity of

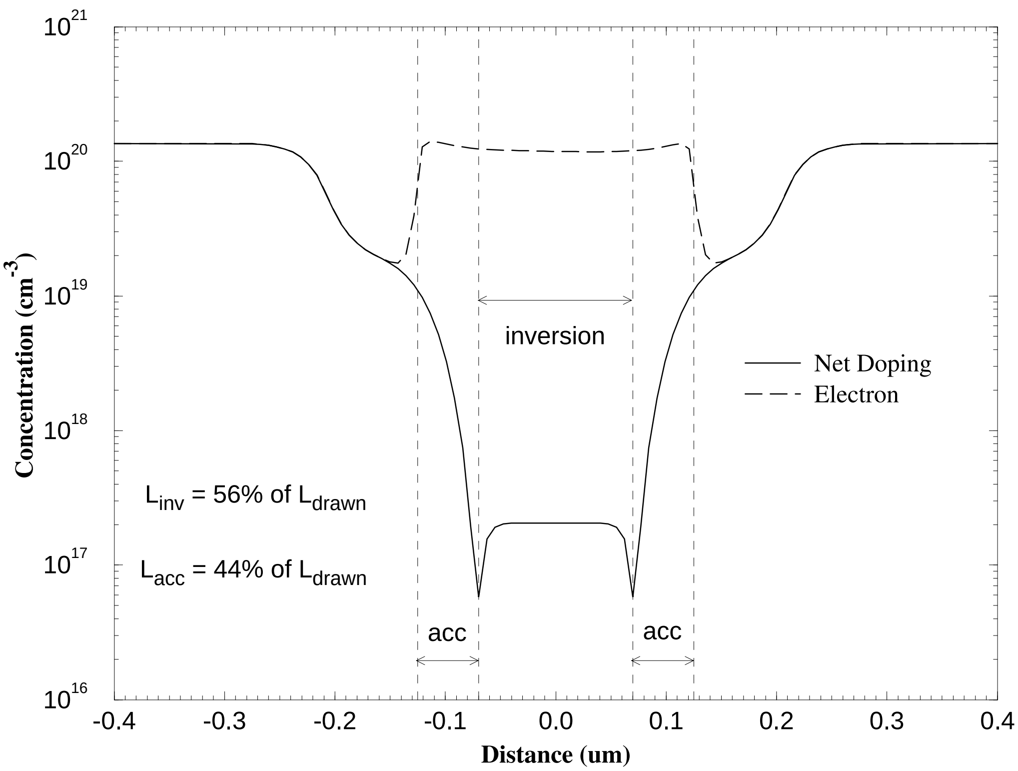

Figure 5.4 Doping profile and electron concentration profile in strong inversion for a 0.25μm As-LDD MOSFET. Compared to the doping profile shown in Figure 5.2, the length of the accumulation layer is longer because of the higher diffusivity of phosphorus.

phosphorus compared to arsenic and also due to its transient enhanced diffusion [38], the overlap region between the LDD and the gate is larger, resulting in shorter metallurgical channel length. Thus, as can be seen from Fig. 5.5, due to the longer accumulation region, more than half of the applied voltage drops outside the intrinsic region.

It might be expected that for longer channel lengths the impact of parasitic series resistance on device performance would be less due to the higher channel resistance. However, this is not necessarily the case since longer channel-length technologies are designed to operate at a higher V_{dd} and hence require LDDs with less peak doping and a more gradual doping profile to alleviate hot carrier effects. For instance, the LDD dose

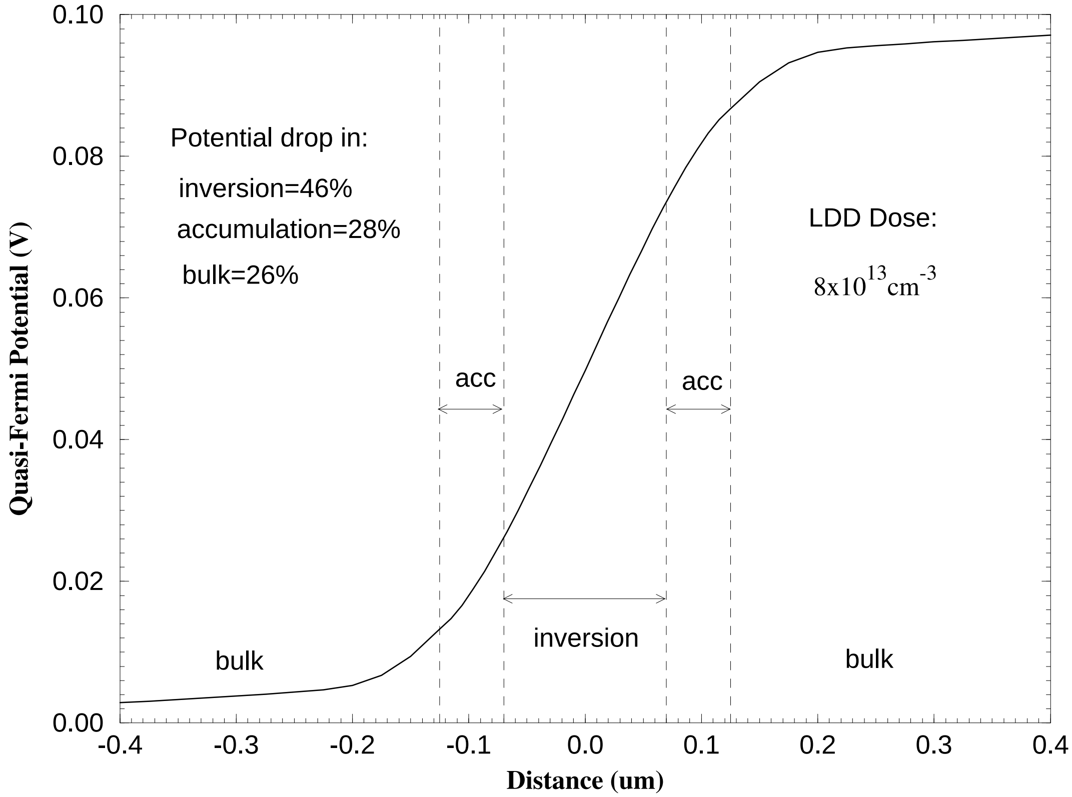

Figure 5.5 Quasi-Fermi potential drop along the Si/SiO_2 interface of a 0.25μm As-LDD MOSFET in strong inversion. The drain bias is 100mV and the gate bias is 2.5V; hence the device is operating in the linear region. Compared to the potential drops shown in Figure 5.3, Ph-LDD devices exhibit considerably more accumulation layer resistance. Interestingly enough though, the spreading resistance is about the same in both cases.

would be lower and the thermal budget higher for a 0.35μm technology designed to operate at 3.3V V_{dd} compared to a 0.25μm technology designed to operate at 2.5V V_{dd}.

A comparison among the three technologies is presented in Table 5.1. As can be seen from Table 5.1, a significant portion of the voltage drops in the extrinsic region of the device, thus requires accurate modeling of the LDD region in order to predict its impact on the terminal characteristics of deep submitting MOSFETs.

Table 5.1: LDD resistance in various technologies

Technology	Inversion $\Delta\varphi$	Acc. $\Delta\varphi$	Bulk $\Delta\varphi$	$L_{metallurgical}$
0.25µm As-LDD	60 %	15 %	25 %	0.74 L_{drawn}
0.25µm Ph-LDD	46 %	28 %	26 %	0.56 L_{drawn}
0.35µm Ph-LDD	55 %	19 %	26 %	0.67 L_{drawn}

5.3 Problems with existing simulation methodology

To date, most of the mobility models for 2-D device simulation [29]-[32] that have appeared in the literature have focused on modeling the inversion layer, since channel resistance was considered to be the limiting factor in carrier transport. Consequently, little attention was paid to the extrinsic region of the device. It was clearly established in the previous section that series resistance effects can no longer be neglected in deep submicron MOSFETs. To this end, we point out the problems associated with existing simulation methodologies and in the next section present an improved methodology.

Due to the lack of a model for accumulation layer mobility and the lack of well-calibrated two-dimensional (2D) process simulation tools, the methodology most commonly used involves the simulation of an "electrically" equivalent MOSFET (see Fig. 5.6) instead of the actual device structure. In this methodology, the gate length is taken to be the effective channel length (L_{eff}) instead of the coded or patterned gate length, and a series resistance (R_{series}) is specified instead of the contact resistance (R_{co}) at the source and drain contacts. Implicit in this methodology is the assumption that only the vertical doping profile in the channel is important for an accurate simulation of the device, which for instance can be obtained through one-dimensional (1D) process simulations.

The L_{eff} is most often defined as the spacing between the source-channel and the drain-channel junction. Ideally, current would be confined to the surface within L_{eff} and then spread into the heavily doped source/drain regions. In reality, the current is confined to the surface even beyond the metallurgical junctions because of the overlap between the

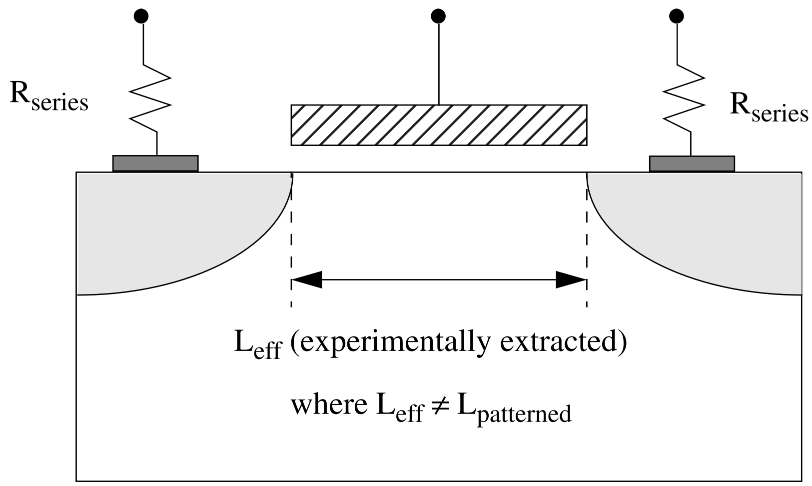

Figure 5.6 Existing technique for simulating an LDD MOSFET. Values for R_{series} and L_{eff} are typically obtained from experimental data, but invariably R_{series} is treated as a calibrating parameter.

gate and the source/drain diffusion regions. This phenomena is more pronounced in LDD MOSFETs which tend to exhibit significant overlap (see Fig. 5.1). The extra distance of surface conduction (i.e. the accumulation layer in Fig. 5.1) can either be considered as part of L_{eff} or as part of R_{series}. It is physically incorrect to consider the accumulation layer as part of L_{eff} since its threshold voltage and mobility are different from that of the inversion layer. However, when considered part of R_{series}, the accumulation layer resistance (R_{acc}) makes R_{series} strongly dependent on gate voltage, since

$$R_{series} = R_{acc}(V_{gs}, L_{overlap}) + R_{sp}(V_{gs}) + R_{ldd} + R_{sd} + R_{co} \tag{5.4}$$

where R_{sp} is the spreading resistance, and R_{ldd} and R_{sd} are the LDD and source/drain sheet resistances respectively.

For non-LDD MOSFETs, the overlap between the gate and the source/drain region in self-aligned technologies is a relatively small fraction of the gate length. Thus, R_{acc} in Eq. (5.4) can be neglected, and since R_{sp} is not a very strong function of gate bias [23], R_{series} can be essentially considered as a constant. For constant L_{eff} and constant R_{series}, several techniques exist for accurately extracting these parameters [113]. Therefore, the simulation methodology shown in Fig. 5.6 can be successfully applied to non-LDD MOSFETs.

However, in the case of LDD MOSFETs, both L_{eff} and R_{series} are functions of gate bias [39] because of which the methodology shown in Fig. 5.6 will be met with little success. In order to improve the comparison between simulations and measurements, R_{series} is often used as a fitting parameter. While such a practise may lead to a few good fits, the predictive nature of TCAD can not be borne out of such a scheme. Instead, the scheme that we propose in the next section considers every aspect of the device in a physically correct sense. It is shown that with the improved calibration methodology, no artificial fitting parameters need to be introduced, thus establishing the viability and predictivity of the new simulation methodology.

5.4 Proposed Simulation Methodology

In order to accurately simulate an LDD MOSFET, the variation of R_{series} with gate bias, in particular each term appearing in Eq. (5.4), will need to be modeled properly. To this end, the actual device structure shown in Fig. 5.7 would need to be simulated instead of the one shown in Fig. 5.6. The patterned gate length, $L_{patterned}$, is specified in the simulation instead of L_{eff} and the actual contact resistance R_{co} is used instead of R_{series}. Since, spreading resistance is a sensitive function of the gradient of the doping profile [23], the doping profile would need to be specified accurately in both the lateral and the transverse directions. Accurate calculation of accumulation layer resistance would require a model for accumulation-layer mobility and a specification of L_{ov} (see Fig. 5.7). Thus, a well-calibrated two-dimensional (2D) process simulator would form an integral part of the proposed simulation methodology.

Figure 5.8 shows the proposed simulation methodology. The doping profiles would be provided by the process simulator PROPHET. In addition, values for contact resistance, effective oxide thickness, and contact-to-poly spacing would need to be supplied to the device simulator PADRE. The following issues need to be considered for an accurate simulation of the LDD device shown in Fig. 5.7:

- Validity of 2D process simulation results.
- Extraction of contact resistance.

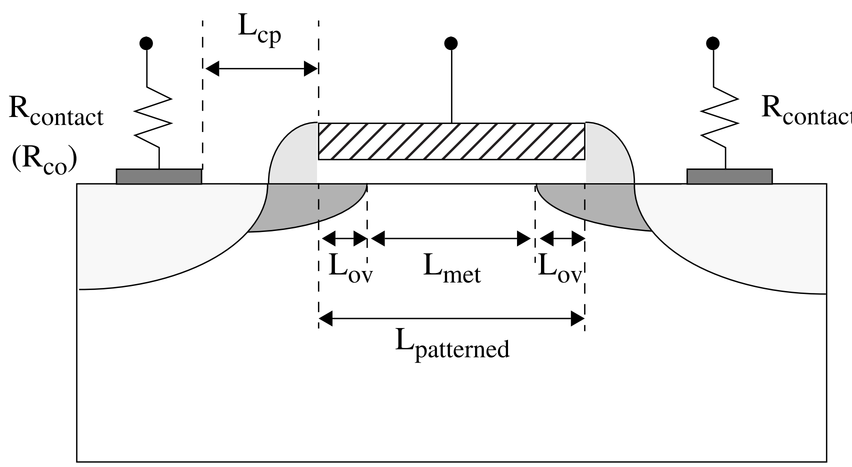

Figure 5.7 Device schematic for simulating an LDD MOSFET. $R_{contact}$ information should be supplied from measurements such as from four-probe Kelvin test structures. Patterned gate length should also obtained from experimental data such as from transmission electron microscopy of the gate stack. Neither $R_{contact}$ nor $L_{patterned}$ are used as fitting parameters in this simulation scheme.

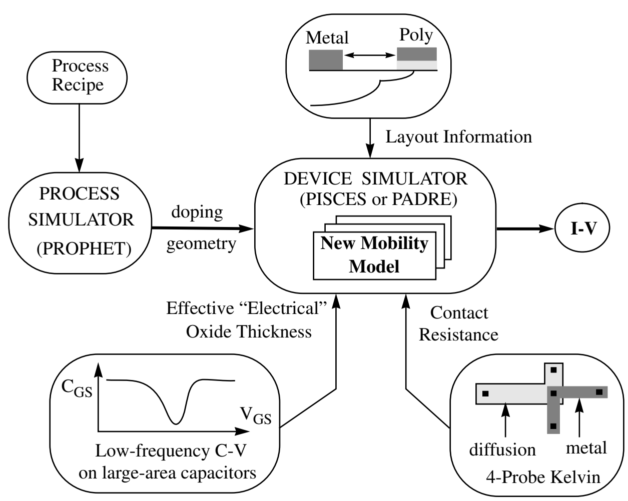

Figure 5.8 Proposed simulation methodology involves coupled 2D process and device simulations. The process recipe is fed to the process simulator to get the 2D doping profiles. Effective oxide thickness and contact resistance values are supplied to the device simulator from independent measurements. Contact-to-poly spacing, L_{cp}, is obtained from layout information.

- Specification of contact-to-poly spacing.
- Extraction of effective electrical gate oxide thickness.
- Extraction of patterned channel length for deep submicron structures.
- Model for accumulation layer mobility.

The simulation methodology will be applied to a realistic 0.25µm technology [37], and it will be shown in the Section 5.6 that a consideration of the above mentioned issues leads to an excellent agreement between simulation and measurement results over wide range of channel length and terminal biases.

5.4.1 Validity of 2D Process Simulation Results

A key issue is the accuracy of process simulation results, in particular that of predicting the doping profiles in the lateral direction. It was shown by Rafferty *et. al.* [38] that the transient enhanced diffusion (TED) effect can have a significant impact on the lateral dopant diffusion in the LDD region, which leads to the reduction of the metallurgical channel length L_{met}. Characterization of the TED effect is essential for an accurate modeling of the lateral doping profile.

From Fig. 5.7, $L_{met} = L_{patterned} - 2L_{ov}$, where $L_{patterned}$ is the actual patterned gate length, and L_{ov} is the overlap length between the gate and the LDD region. Calibration of the TED parameter set proceeds by examining phenomena that are sensitive functions of L_{met}, such as drain-induced barrier lowering (DIBL) and reverse short channel effect in n-channel MOSFETs. If $L_{patterned}$ is determined through a physical measurement of the gate stack such as transmission electron microscopy (TEM), then by varying the TED parameter set, L_{ov} is made to vary, which consequently affects L_{met}. Since $L_{patterned}$ is known with certainty, if the TED parameter set is able to model phenomena that are sensitive to L_{met} , then that establishes that L_{ov} is being correctly predicted by the process simulator.

Calibration of the parameter set associated with TED has been performed by Rafferty *et. al.* [38] for a 0.35µm technology. They show that this parameter set is able to explain the reverse short channel effect and the body effect on the threshold voltage of NMOS devices. Recently, it was shown by Vuong *et. al.* [114] that the same parameter set is also able to model the DIBL effect in 0.35µm technology. Thus, the accuracy of process simulation results using PROPHET is fairly well established.

5.4.2 Extraction of Contact Resistance

The contact resistance, R_{co}, is extracted from four-probe Kelvin test structures [115]. It is important to ensure that the contacts behave linearly over the range of currents forced through them. As the contact window shrinks in size and the current density increases, smaller contacts start exhibiting departure from the linear Ohm's law relationship. However, for the present study shown in Fig. 5.9, the contacts show linear I-V characteristics over the range of currents considered in this work.

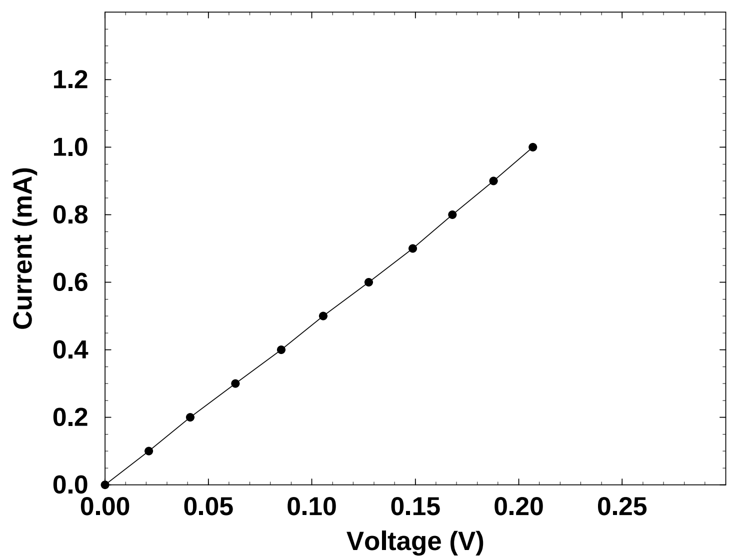

Figure 5.9 I-V characteristics for a 0.5µm x 0.5µm contact window.

5.4.3 Specification of Contact-to-Poly spacing

The purpose of correctly specifying the contact-to-poly spacing, L_{cp}, as shown in Fig. 5.7 is to be able to correctly calculate the LDD and source/drain sheet resistances. The value for L_{cp} is obtained from layout information. This is really a second order correction, since sheet resistance is much smaller than spreading and accumulation layer resistance (see Figs. 5.3 and 5.5). Hence, the exact value of L_{cp} is not very critical. Note that if L_{mask} is not equal to $L_{patterned}$, then L_{cp} obtained from layout information would differ from the actual L_{cp} in the device. This information is more critical for hot carrier studies than for the calculation of sheet resistances.

5.4.4 Extraction of Effective Electrical Gate Oxide thickness

In deep submicron technologies with aggressively scaled dielectrics, the physical thickness of the oxide deviates from its “electrical” thickness primarily due to the quantum capacitance effect [119] and the poly-depletion effect [116]. With a thin dielectric, the transverse electric field near the Si/SiO_2 interface is sufficiently high to cause significant quantization of the electron gas in the inversion layer. According to the quantum mechanical distribution, the electron concentration peaks at a distance z_m below the interface as dictated by the nature of the wavefunction in the inversion layer [45], [48]. On the other hand, a classical calculation predicts that the electron concentration is a maximum at the Si/SiO_2 interface. 2D device simulators such as PADRE and PISCES do not solve for Schrodinger’s equation, and hence they calculate the classical electron distribution in the inversion layer. The principal difference that is observed between a classical calculation (such as from PISCES or PADRE) and a quantum-mechanical calculation (such as from a coupled 1-D Schrodinger-Poisson solver) is a rigid shift in the Q_{inv}-V_{gs} curves in the linear region [117] (i.e. incorporation of the quantum mechanical effects causes an increase in the threshold voltage [118]). Since the classical device simulators calculate the concentration peak to be at the surface, which in reality is z_m below the surface, the effective oxide thickness $T_{ox,eff}$ that should be supplied to the device simulators is $T_{ox}+z_m$, where T_{ox} is the physical oxide thickness that can, for instance, be obtained from ellipsometric measurements [109].

$T_{ox,eff}$ can either be determined from a 1-D Schrodinger-Poisson solver which calculates z_m or it can be obtained directly from the gate-to-channel capacitance (C_{gc}) measurements. Since z_m decreases with gate bias [45] and is not really a constant, it becomes ambiguous to specify $T_{ox,eff}$ by $T_{ox}+z_m$. However, it is known that the integrated channel charge, Q_{inv}, is reduced by a constant factor due to the quantum mechanical effect [117]. Since $Q_{inv}(V_{gs}) = \int_{-\infty}^{V_{gs}} C_{gc}(\tilde{V}_{gs})\, d\tilde{V}_{gs}$, if the measured C_{gc} can be represented by $\varepsilon_{ox}/T_{ox,eff}$, then PISCES and PADRE would be able to correctly calculate Q_{inv} based on the specification of $T_{ox,eff}$.

The other factor that degrades the inversion-layer capacitance (C_{inv}) is the poly-depletion effect (PDE) [116]. While the quantum correction is applicable to both accumulation (C_{acc}) and inversion-layer capacitance, PDE degrades only C_{inv}. For an n^+ doped poly on a p-type substrate, if the dopants in the poly are not completely activated, then when the substrate is in inversion, a depletion layer will form at the poly/SiO_2 interface, resulting in a lower C_{inv}. On the other hand, when the p-type substrate is in accumulation, the poly/SiO_2 interface is also accumulated. Hence, no degradation of C_{acc} occurs. Figure 5.10 illustrates this effect, which is a plot of measured-C_{gc} as a function of gate bias.

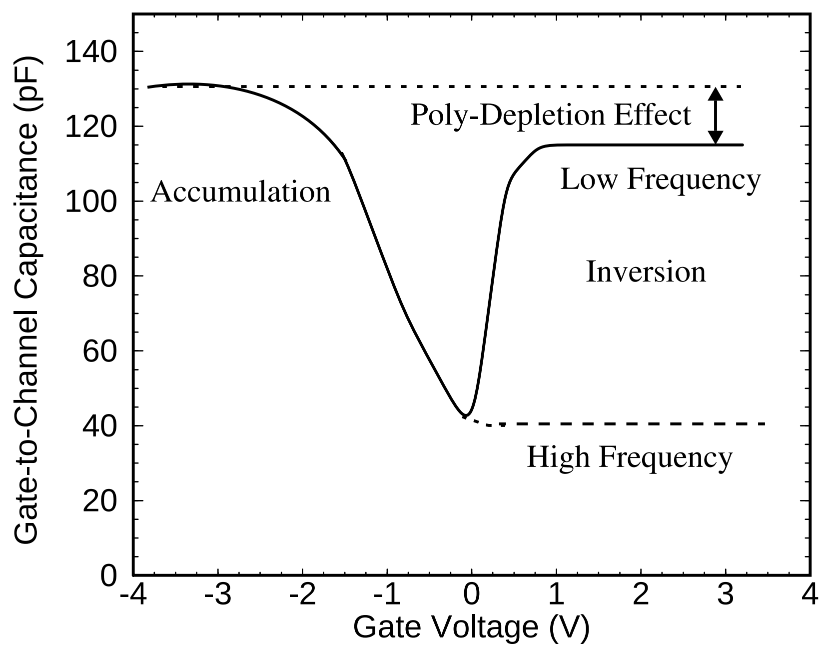

Figure 5.10 Measured gate-to-channel capacitance for a 55Å gate oxide. Due to poly-depletion effect, the capacitance in accumulation is larger than that in inversion. Inversion-layer capacitance is further degraded due to the quantum-mechanical nature of the electron distribution.

Due to these two effects, $T_{ox,eff}$ extracted from the measured C_{inv} is invariably found to be larger than the physical value for oxide thickness T_{ox} [36].

5.4.5 Extraction of Patterned Channel Length

The masked channel length can differ from the patterned channel length, $L_{patterned}$, due to a lack of process control, which for instance can lead to an over-etch of the gate electrode [111]. If the over-etch is a significant fraction of the masked channel length, then it is essential to determine the actual patterned channel length for an accurate simulation of the device. In the absence of TEM measurements, $L_{patterned}$ can also be extracted from electrical measurements [108]. The two parameters most sensitive to $L_{patterned}$ are the off-state leakage current (I_{off}) and the output conductance (g_d) in saturation. Since the TED parameter set in PROPHET is well calibrated to the 0.35µm technology, it is assumed that the same parameter set would be able to accurately predict L_{ov} (see Fig. 5.7) in the next-generation 0.25µm technology.

In deep submicron MOSFETs, I_{off} continues to increase with drain bias unlike long channel MOSFETs in which it saturates for V_{ds} much greater than kT/q [93]. This effect in short-channel MOSFETs is due to drain-induced barrier lowering (DIBL). While in long channel MOSFETs, DIBL is proportional $1/L$ [93], it has been analytically shown by Biesemans and Meyer [112] that for short channel devices, DIBL ~ $e^{-L_{met}/\lambda}$, where L_{met} is the metallurgical channel length and λ is a scaling parameter. The objective then is to use the DIBL information (or equivalently, the I-V curves in subthreshold as a function of drain bias) to extract the "actual" channel length.

For the 0.25µm technology considered in this study, $L_{patterned}$ for 0.25µm and 0.3µm devices was obtained by trying to match the experimentally-observed DIBL with that predicted by simulation results. Since DIBL is a sensitive function of L_{met}, and assuming that L_{ov} is being correctly predicted by PROPHET, simulation results can be matched with experimental results by varying $L_{patterned}$ in the simulations. Since both devices resided on the same die, it was found that the same amount of length reduction for each yielded fairly good fits with experimental data. The results after reduction of the masked length are shown in Fig. 5.11. It was found that devices with channel lengths greater than 0.4µm did not exhibit any measurable DIBL effect, and hence no reduction to the masked channel length was required.

(a)

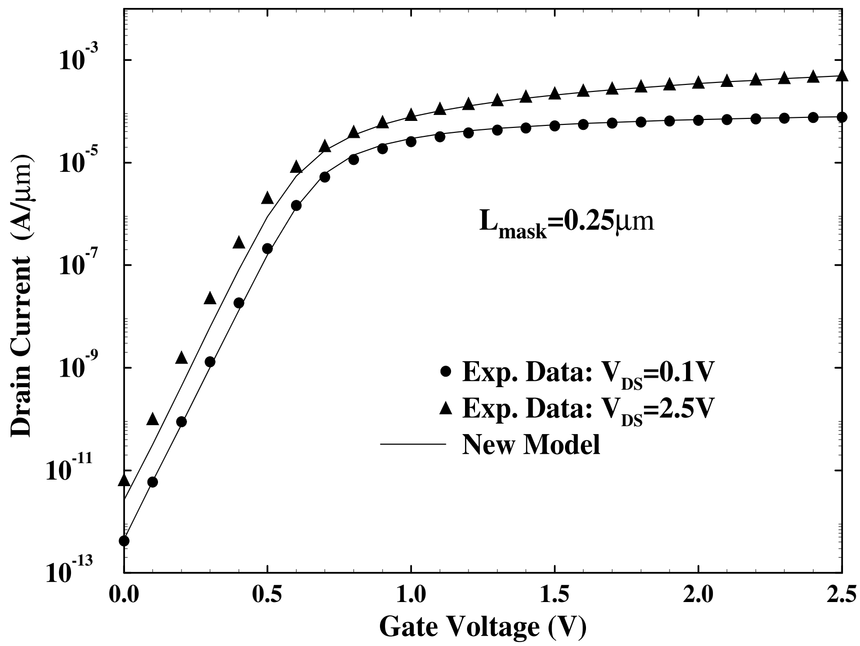

(b)

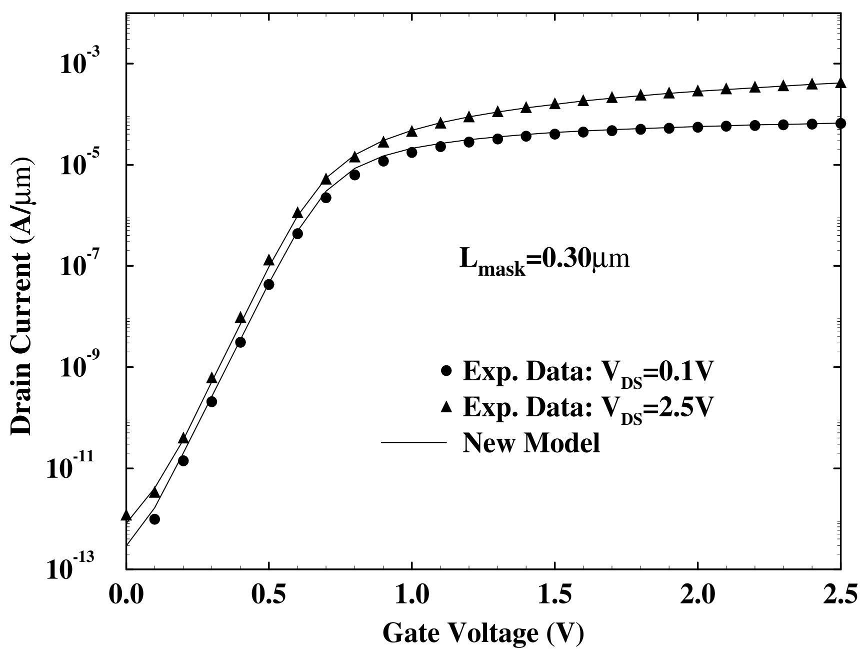

Figure 5.11 Comparison between simulated and measured results in subthreshold for (a) 0.25µm gate length, and (b) 0.3µm gate length, after gate lengths have been reduced to achieve best fits.

5.4.6 Model for Accumulation Layer Mobility

Due to the two-dimensional nature of the electron gas in the accumulation layer, a mobility model similar in form to the one for an inversion layer is required to accurately calculate the resistance in an accumulation layer. Mobility degradation in the accumulation layer occurs in much the same way as it does in the inversion layer due to the transverse electric field. The primary difference arises in Coulombic scattering, which is stronger in the accumulation layer compared to the inversion layer [1], [3].

To establish the importance of a model for accumulation layer mobility in trying to predict the I-V characteristics of LDD MOSFETs, simulations were performed using a mobility model applicable only in the inversion layer [1]. The mobility in the accumulation layer was simply set to the bulk value. Based on the methodology shown in Fig. 5.8, linear region simulations for a 0.25μm device were performed with the inversion-layer mobility model. Results are shown in Fig. 5.12, from which it can be seen that due to the over-prediction of mobility in the accumulation layer, a higher drain current is observed.

5.5 Formulation of the Unified Model

Having discussed the need to model accumulation layer mobility, the starting point for the unified model is the formulation presented in Section 4.2 for inversion layer electrons:

$$\frac{1}{\mu_{unified}} = \frac{1}{\mu_{phonon}} + \frac{1}{\mu_{surface\ roughness}} + \frac{1}{\mu_{Coulomb}} \tag{5.5}$$

For each of the scattering mechanisms appearing in equation (5.5), there is a 2D term and a 3D term. Previously, the 2D term only modeled the inversion layer electrons, which is now extended to model the accumulation layer mobility as well. The hierarchical taxonomy of the resulting unified model is shown in Fig. 5.13. The following three sections present a unified treatment of inversion and accumulation layer electrons for phonon, surface roughness, and Coulombic scattering respectively.

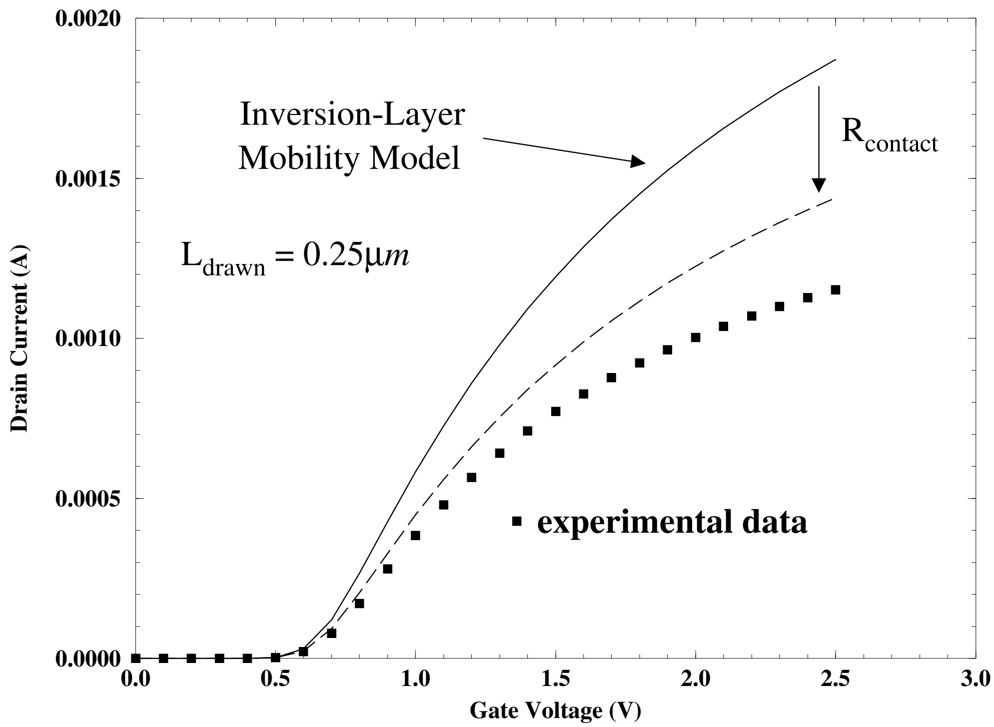

Figure 5.12 Simulation of a 0.25μm LDD MOSFET with a mobility model formulated for the inversion layer only.

5.5.1 Phonon Scattering

In Section 4.3, phonon scattering in MOS inversion layers was considered. In this section, the formulation will be extended to treat accumulation layers as well.

The potential well that creates inversion layer electrons is the same one that creates accumulation layer electrons. The fundamental difference between the two is that an inversion layer is a strictly 2D electron gas (2DEG) whereas an accumulation layer is the union of a 2DEG residing in the sub-bands near the interface and a 3DEG which forms a continuum in the silicon bulk [107]. From Fig. 5.13, it can be seen that the model for phonon scattering has a 2D term and a 3D term. Therefore, description of the accumulation fits in very naturally in the formulation of the model: the 2D aspect of the accumulation layer is combined with the inversion layer model, whereas the 3D aspect is simply 3D phonon scattering, for which a model already exists. The task of modeling

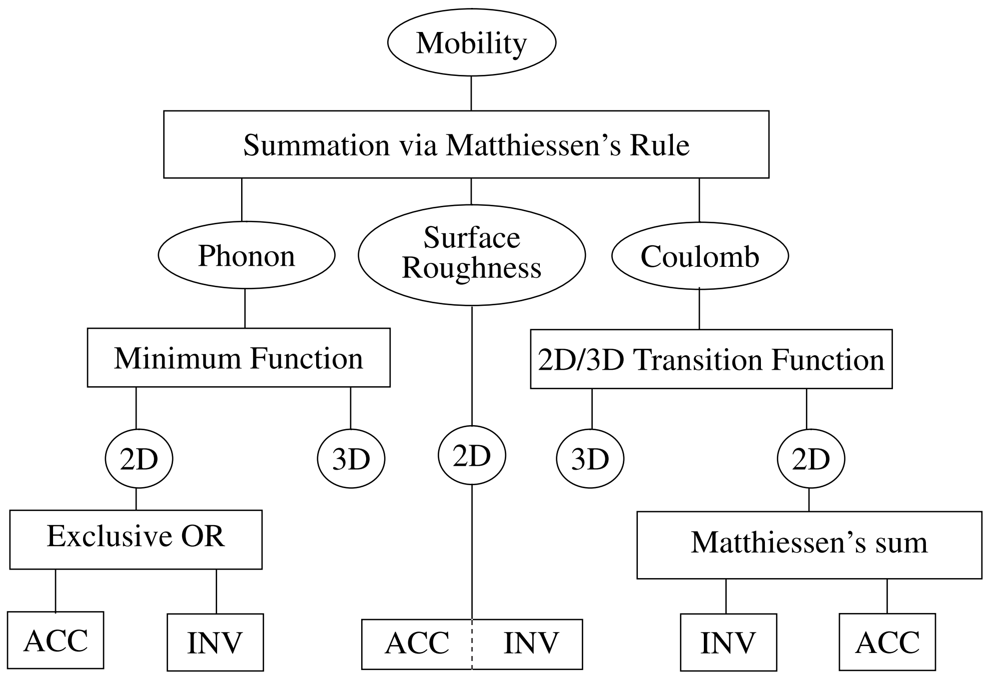

Figure 5.13 Hierarchical taxonomy of the unified model for inversion and accumulation layer electrons.

---

phonon scattering in accumulation layers then reduces to only considering its 2D aspect.

The 2DEG in an accumulation layer is identical to the 2DEG in an inversion layer [107]. Therefore, the same deformation potential for 2D phonon scattering (see Section 4.3.2) would hold for both layers. However, the dielectric screening function (see Section 3.2.2 for definition) in an accumulation layer would be different from that in an inversion layer due to the presence of the continuum of electrons beneath the 2DEG. However, an electron gas is not very effective in screening a phonon deformation potential [106]; hence, the same effective scattering potential would hold for both layers. Therefore, phonon mobility in accumulation layers would be described by the *same* formulation as for inversion layers. A semi-empirical model for inversion layer electrons is given in Section 4.3.3:

$$\mu_{inv}^{ph}(\boldsymbol{r}) = \frac{A}{E_{\perp}(\boldsymbol{r})} + \frac{B \cdot N^{\gamma}_{A}}{T \cdot E_{\perp}^{1/3}(\boldsymbol{r})} \tag{4.25}$$

where N_A is the background acceptor dopant density. In accumulation layers, electrons interact with donor atoms; hence, replacing N_A by N_D, the model for phonon scattering in accumulation layers becomes:

$$\mu_{acc}^{ph}(\boldsymbol{r}) = \frac{A}{E_{\perp}(\boldsymbol{r})} + \frac{B \cdot N^{\gamma}_{D}}{T \cdot E_{\perp}^{1/3}(\boldsymbol{r})} \tag{5.6}$$

The theoretical results derived above are in complete agreement with the experimental findings of Sun and Plummer [33] who showed that accumulation and inversion layer electrons follow the same universal mobility curve.

By noticing that for all cases of interest, either N_A or N_D dominates, accumulation and inversion layer mobilities can be combined into one single equation as:

$$\mu_{2D}^{ph} = \frac{A}{E_{\perp}} + \frac{B \cdot (N_A + N_D)^{\gamma}}{T \cdot E^{1/3}{}_{\perp}} \tag{5.7}$$

In the channel $N_A \gg N_D$, and equation (4.25) is recovered, whereas in the LDD region $N_D \gg N_A$, and equation (5.6) is recovered.

The expression for total phonon mobility given in equation (4.30) for inversion layer electrons now transforms to:

$$\mu_{ph} = \boldsymbol{min}\left[\frac{A}{E_{\perp}(\boldsymbol{r})} + \frac{B \cdot (N_A + N_D)^{\gamma}}{T \cdot E_{\perp}^{1/3}(\boldsymbol{r})}, \mu_{max}\left(\frac{300}{T}\right)^{\theta}\right] \tag{5.8}$$

Refer to Section 4.3.4 and Table 4.2 for parameter values appearing in the above model.

5.5.2 Surface Roughness Scattering

As in the case for phonon scattering, if screening is neglected, the same scattering potential due to surface roughness would be seen by the accumulation and inversion layer electrons. The semi-empirical model for inversion layer electrons is given in Section 4.4.2:

$$\mu_{sr}^{inv} = \frac{C_{inv} \cdot N_A^{\gamma}}{E_{\perp}^2(\boldsymbol{r})} \tag{4.47}$$

Since the model for accumulation layer electrons is similar, we get:

$$\mu_{sr}^{acc} = \frac{C_{acc} \cdot N_D^{\gamma}}{E_{\perp}^2(\boldsymbol{r})} \tag{5.9}$$

If we assume that the “degree” of surface roughness along the Si/SiO_2 interface in the gate-LDD overlap region is the same as in the channel region, then $C_{acc} = C_{inv}$, and the resulting model for surface roughness becomes

$$\mu_{sr} = \frac{C \cdot (N_A + N_D)^{\gamma}}{E_{\perp}^2(\boldsymbol{r})} \tag{5.10}$$

5.5.3 Coulombic Scattering

The principal difference between Coulombic scattering in accumulation and inversion layers is that in an accumulation layer, electrons scatter off positively charged donor atoms, whereas in an inversion layer, electrons scatter off negatively charged acceptor atoms. Coulombic scattering potentials were calculated in Section 3.2 under the Born approximation [70] which assumes that the kinetic energy of the electrons is much larger than the interaction potential due to the impurity atom. Being a first order approximation to time-dependent perturbation theory [70], the Born approximation does not differentiate between repulsive and attractive Coulomb potentials [40]. However, more accurate phase-shift analysis reveals that electrons are scattered more strongly from attractive than from repulsive potentials [40]. Intuitively, one can imagine that a repulsive scattering center never lets the carriers get close enough for them to experience a strong potential that would eventually scatter them off more strongly.

The ratio between attractive and repulsive carrier mobility has been modeled by Klaassen [34] using a seventh-order spline function (also see equation (4.60) in Section 4.5.2):

$$\frac{\mu_{att}}{\mu_{rep}} = \frac{\mu_{acc}}{\mu_{inv}} = G(P) \tag{5.11}$$

where *P* is a parameter that depends on electron concentration and temperature [34] (also see Section 4.5.2). A semi-empirical model for 2D Coulombic scattering in the inversion layer was presented in Section 4.5.1 :

$$\mu_{coul}^{inv} = max\left[\left(D_1 \frac{n^{\kappa}}{N_A^{\beta_1}}\right), \left(\frac{D_2}{N_A^{\beta_2}}\right)\right] \tag{4.54}$$

The function *G(P)* is formulated for a 3D electron gas. Nevertheless, we apply this function to the 2D electron gas. The accumulation layer mobility is obtained by replacing N_A with N_D in equation (4.57) :

$$\mu_{acc} = max\left[\left(D_1 \frac{n^{\kappa}}{N_D^{\beta_1}}\right), \left(\frac{D_2}{N_D^{\beta_2}}\right)\right] \cdot G(P) \tag{5.12}$$

The 2D Coulombic mobility is obtained from inversion and accumulation layer mobilities via the Matthiessen's rule's summation:

$$\frac{1}{\mu_{2D}^{Coul}} = \frac{1}{\mu_{inv}} + \frac{1}{\mu_{acc}} \tag{5.13}$$

The expression for total Coulombic mobility is given by equation (4.55):

$$\mu_{coulomb} = f(\alpha) \cdot \mu_{3D}^{Coul} + [1 - f(\alpha)] \cdot \mu_{2D}^{Coul} \tag{4.52}$$

where expressions for $f(\alpha)$ and μ_{3D}^{Coul} are given in Section 4.5.

5.5.4 Total Mobility including Longitudinal Field degradation

The unified mobility model given by equation (5.5) considers the variation of mobility with transverse electric field, electron concentration, and ionized impurity concentration. The scattering mechanisms that lead to this mobility — acoustic phonon, surface roughness, and Coulombic scattering — are all elastic in nature (i.e. they do not change the kinetic energy of the carriers). When carriers heat up under the action of an applied electric field, another scattering mechanism — optical phonon scattering — becomes important which is inelastic in nature. Since, carrier heating is caused by the component of electric field parallel to the velocity of electrons, the degradation in mobility due to optical phonon scattering is modeled semi-empirically via the longitudinal electric field $E_{\|}$. In the inversion layer, $E_{\|}$ is created by drain bias whereas $E_{\perp}$ (transverse electric field) is caused by gate bias. When all four scattering mechanisms are considered together, the resulting semi-empirical expression for total mobility is given by

$$\mu_{total} = \frac{2\mu_{unified}}{1 + \left[1 + 4\left(\frac{\mu_{unified}E_{\|}}{v_{sat}}\right)^2\right]^{1/2}} \tag{5.14}$$

where the model for longitudinal field degradation is due to Hansch *et. al.* [35], and v_{sat} is the saturation velocity in the inversion layer.

5.6 Results

As an illustration of the methodology presented in the Section 5.4, simulations were performed for a 0.25μm technology using the unified mobility model developed in the previous section. Simulations have been performed over a wide range of channel lengths for the linear and saturation regimes. For each channel length, the doping profile of the device was obtained from PROPHET. Since, the experimental data across channel lengths came from devices residing on the same die (reticle), inter-die variation was not an issue. Contact resistance measurements were performed on Kelvin test structures present on the same die as the MOSFETs. Similarly, the capacitance measurements were performed on large area capacitors present on the same die. Thus, the values extracted for contact resistance and the effective electrical gate oxide thickness can be related directly to the devices since inter-die variation is not a concern.

The first simulation that was performed was for a 20μm MOSFET operating in the linear region. The purpose of this simulation is to test the inversion part of the unified model and the validity of the extraction of the effective gate oxide thickness. For such a long channel device, series resistance does not degrade the I-V characteristics since channel resistance is dominant. Thus, the accuracy of accumulation layer mobility and lateral doping profile is not an issue. If the threshold voltage for this device is predicted correctly, that establishes that the value for oxide thickness and the doping profile in the vertical direction has been correctly specified. Next, the measured and simulated results are compared in the high gate bias regime (i.e. $V_{gs} = V_{dd}$). In this regime, due to high transverse electric fields, mobility is primarily limited by surface roughness scattering [53]. The parameter appearing in the model for surface roughness scattering cannot be considered as a "universal" parameter unlike those appearing in the model for phonon and Coulombic scattering since it is directly dependent on the quality of the Si/SiO_2 interface. Based on the discrepancy observed in the high gate bias regime, the parameter for surface roughness scattering is adjusted to achieve the best possible fit. Results after this fitting are shown in Fig. 5.14, which also show that the threshold voltage is being calculated correctly.

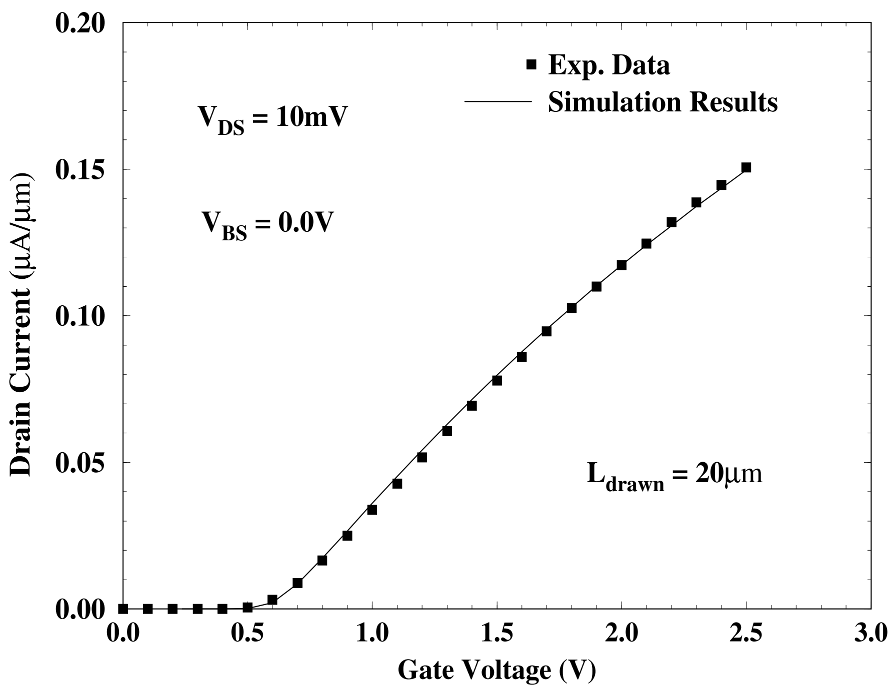

Figure 5.14 Comparison between simulated and measured results for a 20.0µm MOSFET after adjustment of the surface roughness parameter.

Next, linear region simulations for short channel devices are performed. Since, the inversion part of the model, the value for effective oxide thickness, and the vertical doping profile information was validated through simulations of a long channel device, simulations of short-channel devices would test the validity of the model for accumultion layer mobility, extraction of the contact resistance, and lateral doping profile information. While each of these parameters have been separately calibrated, these simulations would serve to establish the validity of the overall framework of the simulation methodology. Figure 5.15 presents the linear-region comparison between simulation and measured results for gate lengths varying from 0.5µm to 0.25µm. Considering Fig. 5.14 as well, excellent fits are obtained over a wide range of channel lengths. It should be emphasized that the same parameter set in the mobility model is able to produce these results across channel lengths.

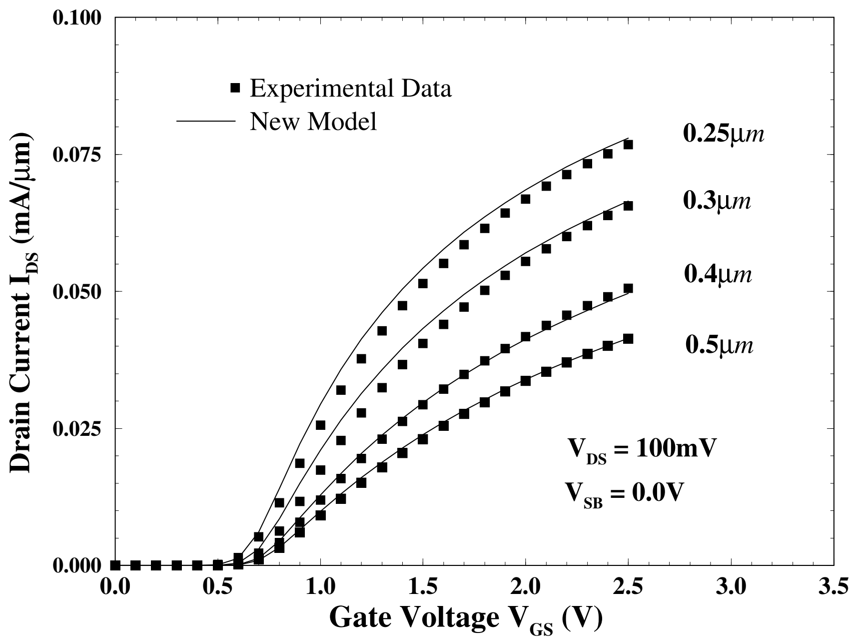

Figure 5.15 Comparison between simulation results and measured data in the linear region for gate lengths ranging from 0.5µm to 0.25µm. It should be noted that the fits for all the shown gate lengths are produced by one mobility parameter set.

The final step is to simulate the saturation region characteristics. Figure 5.16 presents the comparison between simulation and measurement results in the saturation region for MOSFETs with gate lengths ranging from 0.25µm to 20µm. Good agreement is obtained across these gate lengths, establishing the applicability of the new model over a

(a)

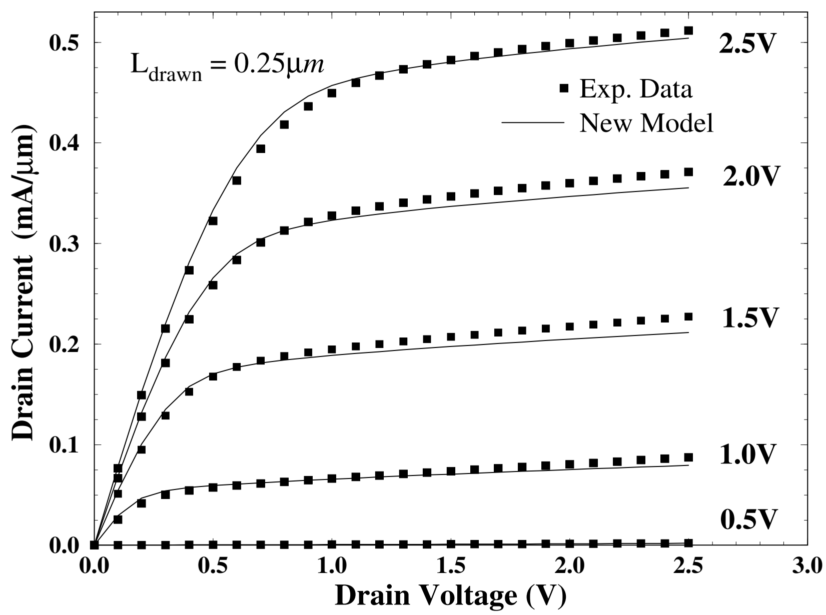

(b)

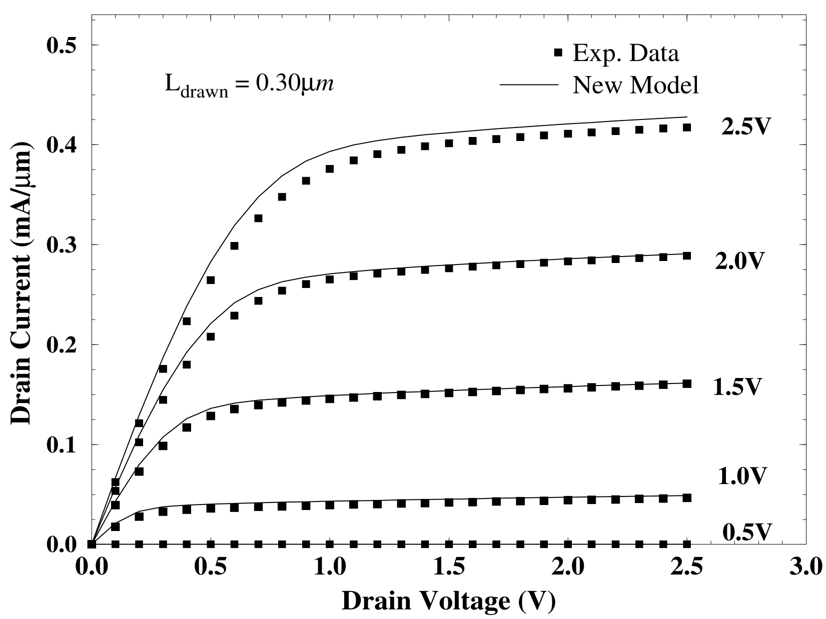

Figure 5.16 Comparison between simulated and measured results in saturation for MOSFETs with gate length: (a) 0.25µm, (b) 0.3µm, (c) 0.4µm, (d) 0.5µm, and (e) 20.0µm.

(c)

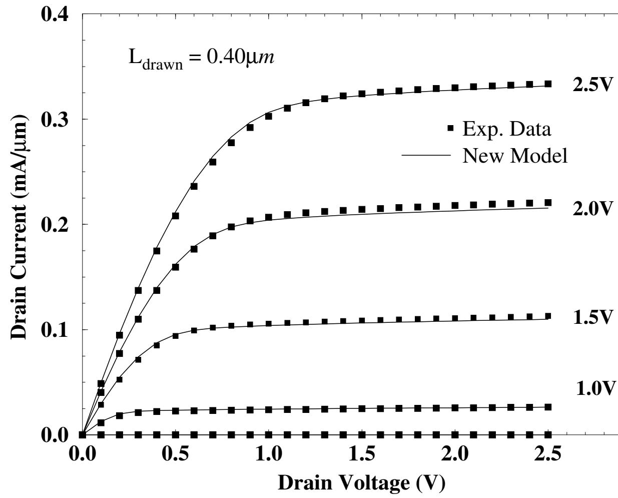

(d)

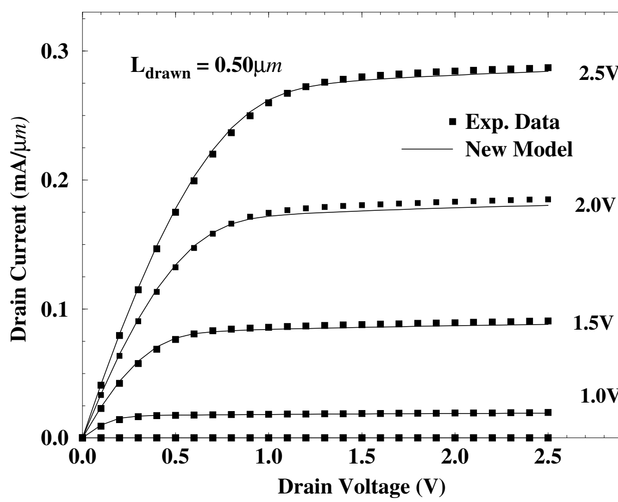

(e)

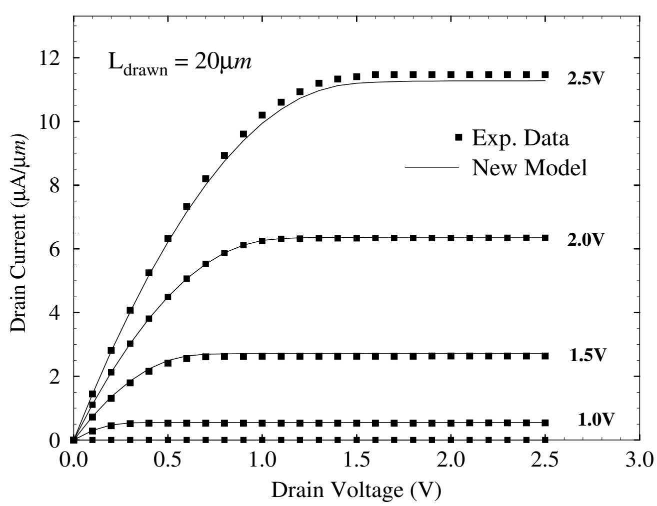

Figure 5.16

wide range of device geometries and terminal biases.

5.7 Summary

Using 2D process and device simulations, it was shown in this chapter that the parasitic series resistance in deep submicron LDD MOSFETs has become comparable to the intrinsic channel resistance. It was demonstrated that conventional mobility models formulated for the inversion layer fail to accurately reproduce the I-V characteristics of LDD MOSFETs. In an effort to model the extrinsic resistance of the device, a model for accumulation layer mobility was developed that considered phonon, surface roughness, and Coulombic scattering in the accumulation layer.

A systematic simulation methodology was presented which emphasized the consideration of the following issues for an accurate simulation of LDD MOSFETs:

- validity of 2D process simulation results
- extraction of contact resistance
- specification of contact-to-poly spacing
- extraction of effective electrical gate oxide thickness
- extraction of patterned channel length for deep submicron structures
- a unified model for inversion and accumulation layers

Excellent fits with measured I-V characteristics of a realistic 0.25μm technology over a wide range of channel lengths and terminal biases were demonstrated with the help of the proposed simulation methodology.

Chapter 6

Conclusion

6.1 Summary

In summary, we have examined the theoretical issues related to the modeling of mobility and suggested new measurements to enhance existing calibration techniques. The study of mobility was motivated by the fact that it is one of the most important parameter affecting the I-V characteristics of MOSFETs. In that regard, two particular issues — Coulomb scattering and LDD resistance — were studied that have emerged in recent years due to the continued scaling of MOSFETs to deep submicron dimensions. The objective of this research was to develop physically-based mobility models, and the approach taken to achieve this was to start with a first-principles calculation of mobility, and then proceed to semi-empirical and empirical forms by means of calibration techniques. The major findings and results of this research are summarized below.

6.1.1 2D Coulombic Scattering in MOS inversion layers

1. A first-principles calculation of two dimensional Coulombic scattering was performed for inversion layer electrons. It was demonstrated that for both screened and unscreened scattering, the new 2D model exhibited better agreement than classical 3D models.
2. A new systematic technique was presented for extraction of unscreened Coulombic scattering that involved classical and quantum simulations and required the use of I-V and C-V data.

3. It was demonstrated that accurate prediction of threshold voltage and off-state leakage current in heavily doped MOSFETs requires the use of well-calibrated models for Coulombic scattering in device simulators.

6.1.2 A Semi-Empirical Model for the Generalized Mobility Curve

1. Semi-empirical models for phonon, surface roughness, and Coulombic scattering were obtained from a first-principles calculation of the respective terms. The total model was obtained via a Matthiessen's rule summation of the three terms.
2. It was demonstrated that the new model reproduced all the properties of the universal and the generalized mobility curve.
3. The model was formulated in local form to exploit numerical properties of moment-based device simulators.

6.1.3 A Unified Model for LDD MOSFETs

1. It was demonstrated through coupled 2D process and device simulations that in deep submicron LDD MOSFETs, extrinsic resistance has become comparable to channel resistance. Hence, accurate simulations require mobility models valid in both regions.
2. A physically-based semi-empirical local mobility model for inversion and accumulation layer electrons was presented that accurately reproduced the I-V characteristics of MOSFETs down to 0.25µm gate lengths.
3. A systematic technique was presented for the calibration and validation of mobility models that requires the independent extraction of contact resistance from Kelvin test structures and effective oxide thickness from quasi-static C-V measurements.
4. Finally, it was demonstrated that drift-diffusion device simulators can accurately model the saturation region characteristics of MOSFETs down to 0.25µm gate lengths provided well-calibrated and physically-based low-field mobility models are used.

6.2 Future Work

Based on the findings of this research, future work is suggested in the following areas:

1. The unified mobility model presented in Chapter 5 was implemented in the drift-diffusion (DD) transport equation. It was recognized in the course of this research that for gate lengths shorter than 0.25µm, the DD formulation failed to give accurate results due to hot-carrier effects occurring in the channel. To extend the model to shorter channel lengths, it is suggested that the low-field mobility model be implemented in either an energy-transport or a hydrodynamic formulation of carrier transport.

2. One consequence of MOSFET scaling — the emergence of Coulombic scattering due to channel impurities — was considered in this research. The other consequence is the emergence of quantum mechanical effects in the channel due to thinner dielectrics. Significant error is introduced in charge calculations if only classical equations are solved. The ad hoc approach used in this thesis was to correct for this effect by extracting an effective oxide thickness (see Section 5.6). Hence, a partial if not a full quantum treatment of the inversion layer is required. The challenge would be to implement the quantum mechanical effects in 2D device simulators such as PISCES without adversely affecting the computation time.

3. In this thesis, existing mobility models were enhanced in two aspects: inclusion of a physically-based model for Coulombic scattering, and incorporation of a model for accumulation layer electrons. Since these two effects have emerged in deep submicron MOSFETs, they need to be incorporated in compact models for circuit simulation as well in order to extend their range of applicability.

Bibliography

[1] S. A. Mujtaba, R. W. Dutton, and D. L. Scharfetter, "Semi-empirical local NMOS mobility model for 2-D device simulation incorporating screened minority impurity scattering," in *Proc. 5th Intl. Workshop on Numerical Modeling of Processes and Devices for Integrated Circuits (NUPAD)*, pp. 3-6, 1994.

[2] S. A. Mujtaba, S. Takagi, R.W. Dutton, "Accurate modeling of Coulombic scattering, and its impact on scaled MOSFETs," in *Symp. VLSI Technology Dig. Tech. Papers*, pp. 99-100, 1995.

[3] S. A. Mujtaba, M. R. Pinto, D. M. Boulin, C. S. Rafferty, R. W. Dutton, "An accurate NMOS mobility model for 0.25µm MOSFETs," in *Proc. 6th Intl. Conf. Simulation of Semiconductor Devices and Processes (SISDEP)*, pp. 424-427, 1995. *Simulation of Semiconductor Devices and Processes*, vol. 6, Edited H. Ryssel and P. Pichler, Springer-Verlag, Wein, Germany, 1995.

[4] S. A. Mujtaba and R. W. Dutton, "Design methodology for low power CMOS technologies," in *Proc. Hierarchical Technology CAD — Process, Device, and Circuits*, August 1995, Stanford University, Stanford, CA.

[5] C. Hu, "Future CMOS scaling and reliability," *Proc. IEEE*, vol. 81, pp. 682-689, 1993.

[6] Y. Taur, Y.-J. Mii, D. J. Frank, H.-S. Wong, D. A. Buchanan, S. J. Wind, S. A. Rishton, G. A. Sai-Halasz, and E. J. Nowak, "CMOS scaling into the 21st century: 0.1µm and beyond," *IBM J. Res. & Dev.*, vol. 39, no. 1-2, pp. 245-60, 1995.

[7] S. M. Sze, *Physics of Semiconductor Devices*, 2nd Edition, New York: Wiley 1981.

[8] T. Ando, A. B. Fowler, and F. Stern, “Electronic properties of two-dimensional systems,” *Rev. Mod. Phys.*, vol. 54, no. 2, pp. 437-672, 1982.

[9] S. Takagi, M. Iwase, and A. Toriumi, “On the universality of inversion-layer mobility in n- and p-channel MOSFETs,” in *IEDM Tech. Dig.*, pp. 398-401, 1988.

[10] S. Takagi, A. Toriumi, M. Iwase, and H. Tango, “On the universality of inversion-layer mobility in Si MOSFETs: Part I — effects of substrate impurity concentration,” *IEEE Trans. Elec. Dev.*, vol. 41, no. 12, pp. 2357-62, 1994.

[11] S. Takagi, A. Toriumi, M. Iwase, and H. Tango, “On the universality of inversion-layer mobility in Si MOSFETs: Part II — effects of surface orientation,” *IEEE Trans. Elec. Dev.*, vol. 41, no. 12, pp.2363-8, 1994.

[12] E. Conwell and V. Weisskopf, “Theory of impurity scattering in semiconductors,” *Phys. Rev.*, vol. 77, no. 3, pp. 388-390, 1950.

[13] H. Brooks, “Scattering by ionized impurities in semiconductors,” *Phy. Rev.*, vol. 83, p. 879, 1951.

[14] N. W. Ashcroft and N. D. Mermin, *Solid State Physics*, Saunders College, Philadelphia, 1976.

[15] M. Lundstrom, *Fundamentals of Carrier Transport*, Addison-Wesley, Reading, MA, 1990.

[16] L. Boltzmann, *Lectures on gas theory*, University of California Press, Berkeley, 1964, translated by S. G. Brush.

[17] J. J. Duderstadt and W. R. Martin, *Transport Theory*, Wiley, New York, 1979.

[18] P. W. Bridgman, “Note on the principle of detailed balancing,” *Phys. Rev.*, vol. 31, pp. 101-102, 1928.

[19] J. E. Chung, M. C. Jeng, J. E. Moon, P. K. Ko, C. Hu, “Performance and reliability design issues for deep-submicrometer MOSFETs,” *IEEE Trans. Elec. Dev.*, vol. 38, no. 3, pp. 545-553, 1991.

[20] G. Baccarani and G. A. Sai-Halasz, “Spreading resistance in submicron MOSFETs”, *IEEE Elec. Dev. Letters*, vol. 4, no. 2, pp. 227-29, 1983.

[21] M. H. Seavey, "Source and drain resistance determination for MOSFETs," *IEEE Elec. Dev. Letters*, vol. 5, no. 11, pp. 479-481, 1984.

[22] K. K. Ng, R. J. Bayruns, and S. C. Fang, "The spreading resistance of MOSFETs", *IEEE Elec. Dev. Letters*, vol. 6, no. 4, pp. 195-198, 1985.

[23] K. K. Ng and W. T. Lynch, "Analysis of the gate-voltage-dependent series resistance of MOSFETs," *IEEE Tran. Elec. Dev.*, vol. 33, no. 7, pp. 965-972, 1986.

[24] F. M. Klaasseen, P. T. F. Biermans, and R. M. D. Velghe, "The series resistance of submicron MOSFETs and its effect on their characteristics," *J. De Physique*, Colloque C4, suppl. 9, pp. 257-260, Sep. 1988.

[25] J. Lee, M. B. Lee, S. Y. Lee, K. N. Kang, K. S. Yoon, "Simple model for gate-voltage dependent parasitic resistance in short channel lightly doped drain metal oxide semiconductor field effect transistor," *Jap. J. Appl. Phys.*, vol. 30, no. 4A, pp. L 535-L 537, 1991.

[26] B. Lemaitre, "An improved analytical LDD-MOSFET model for digital and analog circuit simulation for all channel lengths down to deep-submicron," in *IEDM Tech. Dig.*, pp. 333-336, 1991.

[27] M. R. Pinto, D. M. Boulin, C. S. Rafferty, R. K. Smith, W. M. Coughran Jr., I. C. Kizilyalli, M. J. Thoma, "Three-dimensional characterization of bipolar transistors in a submicron BiCMOS technology using integrated process and device simulation," in *IEDM Tech. Dig.*, pp. 923-926, 1992.

[28] M. R. Pinto, "Simulation of ULSI device effects," *Electrochem. Soc. Proc.*, vol. 91-11, pp. 43-51, 1991.

[29] S. A. Schwarz and S. E. Russek, "Semi-Empirical equations for electron velocity in Silicon: Part II — MOS Inversion layer," *IEEE Trans. Elec. Dev.*, vol. 30, no. 12, pp. 1634-1639, 1983.

[30] C. Lombardi, S, Manzini, A. Saporito, and M. Vanzi, "A Physically based mobility model for numerical simulation of nonplanar devices," *IEEE Trans. CAD*, vol. 7, no. 11, pp. 1164-71, 1988.

[31] T. Nishida and C. T. Sah, "A physically based mobility model for MOSFET numerical simulation," *IEEE Trans. Elec. Dev.*, vol. 34, no. 2, pp. 310-320, 1987.

[32] H. Shin, A. F. Tasch, C. M. Maziar, and S. K. Banerjee, "A new approach to verify and derive a transverse-field-dependent mobility model for electrons in MOS

inversion layers," *IEEE Trans. Elec. Dev.*, vol. 36, no. 6, pp. 1117-1123, 1989.

[33] S. C. Sun and J. D. Plummer, "Electron mobility in inversion and accumulation layers on thermally oxidized silicon surfaces," *IEEE Trans. Elec. Dev.*, vol. 27, no. 8, pp. 1497-1508, 1980.

[34] D. M. B. Klaassen, "A Unified mobility model for device simulation — I. Model equations and concentration dependence," *Sol. State Elec.*, vol. 35, no. 7, pp. 953-959, 1992.

[35] W. Hansch and M. Miura-Mattausch, "The hot electron problem in small semiconductor devices," *J. Appl. Phys.*, vol. 60, no. 2, pp. 650-656, 1986.

[36] K. Krisch, AT&T Bell Laboratories, *Private Communication*.

[37] D. M. Boulin, W. M. Mansfield, K. J. O'Connor, J. Bevk, D. Brasen, M. Cheng, R. A. Cerilli, S. A. Eshraghi, M. L. Green, K. V. Guinn, S. J. Hillenius, D. E. Ibboston, D. C. Jacobson, Y. O. Kim, C. A. King, R. C. Kistler, F. P. Klemens, K. S. Krisch, A. Kornblit, J. T. C. Lee, L. Manchanda, S. C. McNevin, S. V. Moccio, D. P. Monroe, K. K. Ng, M. L. O'Malley, C. S. Rafferty, G. P. Schwartz, S. Vaidya, G. R. Weber, L. C. Feldman, M. R. Pinto, T. Itani, T. Tounai, K. Kasama, H. Miyamoto, E. Ikawa, E. Hasagawa, A. Ishitani, H. Ito, T. Horiuchi, S. Saito, M. Nakamae, "A Symmetric 0.25µm CMOS Technology for Low-Power, High-Performance ASIC Applications Using 248nm DUV Lithography," in *Symp. VLSI Technology Dig. Tech. Papers*, pp. 65-66, 1995.

[38] C. S. Rafferty, H.-H. Vuong, S. A. Eshraghi, M. D. Giles, M. R. Pinto, S. J. Hillenius, "Explanation of reverse short channel effect by defect gradient," in *IEDM Tech. Dig.*, pp. 311-314, 1993.

[39] G. Hu, C. Chang, and Y.-T. Chia, "Gate-voltage dependent effective channel length and series resistance of LDD MOSFET's," I*EEE Trans. Elec. Dev.*, vol. ED-34, no. 12, pp. 2469-75, 1987.

[40] F. J. Blatt, "Scattering of carriers by ionized impurities in semiconductors," *J. Phys. Chem. Solids*, vol. 1, pp. 262-269, 1957.

[41] D. K. Ferry, *Semiconductors*, Macmillan, New York, 1991.

[42] B. R. Nag, *Theory of Electrical Transport in Semiconductors*, Pergamon Press, New York, 1972.

[43] A. G. Sabnis and J. T. Clemens, "Characterization of the electron mobility in the

inverted <100> Si Surface," in *IEDM Tech. Dig.*, pp. 18-21, 1979.

[44] M. S. Lin, "A better understanding of the channel mobility of Si MOSFETs based on the physics of quantized subbands," *IEEE Trans. Elec. Dev.*, vol. 35, no. 12, pp. 2406-2411, 1988.

[45] F. Stern, "Self-consistent results for n-Type Si Inversion Layers," *Phys. Rev. B*, vol. 5, no. 12, pp. 4891-4899, 1972.

[46] D. K. Ferry, K. Hess, and P. Vogl, "Physics and Modeling of Submicron Insulated-Gate Field-Effect Transistors. II -- transport in the quantized inversion layer," in *VLSI Electronics*, Microstructure Science, vol. 2, Academic Press, New York, pp. 67-103, 1981.

[47] C. T. Sah, T. H. Ning, and L. L. Tschopp, "The scattering of electrons by surface oxide charges and by lattice vibrations at the silicon-silicon dioxide interface," *Surf. Sci.*, vol. 32, pp. 561-575, 1972.

[48] F. Stern, "Quantum properties of surface space-charge layers," in *CRC Critical Reviews in Solid State Sciences*, vol. 4, pp. 499-514, 1974.

[49] A. P. Gnadinger and H. E. Tally, "Quantum mechanical calculation of the carrier distribution and the thickness of the inversion layer of a MOS field-effect transistor," *Sol. State Elec.*, vol. 13, pp. 1301-1309, 1970.

[50] F. Stern and W. E. Howard, "Properties of Semiconductor Surface Inversion Layers in the Electric Quantum Limit," *Phys. Rev.*, vol. 163, no. 3, pp. 816-835, 1967.

[51] F. F. Fang and W. E. Howard, "Negative field-effect mobility on (100) Si surfaces," *Phys. Rev. Lett.*, vol. 16, pp. 797-799, 1966.

[52] A. Harstein, T. H. Ning, and A. B. Fowler, "Electron scattering in Silicon Inversion Layers by oxide charge and surface roughness," *Surf. Sci.*, vol. 58, pp. 178-181, 1976.

[53] K. Lee, J. S. Choi, S. P. Sim, and C. K. Kim, "Physical understanding of Low-Field Carrier Mobility in Silicon MOSFET Inversion Layer," *IEEE Trans. Elec. Dev.*, vol. 38, no. 8, pp. 1905-1912, 1991.

[54] M. R. Pinto, C. S. Rafferty, H. R. Yeager and R. W. Dutton, "PISCES-IIB Supplementary Report," Stanford University, Stanford, California, 1985.

[55] M. R. Pinto, *Comprehensive Semiconductor Device Simulation for Silicon ULSI*, Ph.D. thesis, Stanford University, 1990.

[56] R. W. Dutton and Z. Yu, *Technology CAD: computer simulation of IC processes and devices*, Kluwer Academic, Boston, 1993.

[57] B. Herndon, *A Methodology for the Parallelization of PDEs: Application to Semiconductor Device Physics*, Ph.D. thesis, Stanford University, 1995.

[58] S. Kawaji, "The Two-Dimensional Lattice Scattering Mobility in a Semiconductor Inversion Layer," *J. Phys. Soc. Japan*, vol. 27, no. 4, pp. 906-908, 1969.

[59] C. M. Wolfe, N. Holonyak, and G. E. Stillman, *Physical Properties of Semiconductors*, Prentice-Hall, New Jersey, 1989.

[60] K. Hess, *Advanced Theory of Semiconductor Devices*, Prentice-Hall, New Jersey, 1988.

[61] F. J. Morin and J. P. Maita, "Electrical properties of silicon containing arsenic and boron," *Phys. Rev.*, vol. 96, pp. 28-35, 1954.

[62] S. S. Li and W. R. Thurber, "The dopant density and temperature dependence of electron mobility and resistivity in n-type silicon," *Solid State Elec.*, vol. 20, p. 609-616, 1977.

[63] B. K. Ridley, "The electron-phonon interaction in quasi-two-dimensional semiconductor quantum-well structures," *J. Phys. C: Solid State Phys.*, vol. 15, pp. 5899-5917, 1982.

[64] B. K. Ridley, "Electron-Phonon interaction in 2D systems," in *Hot Carriers in Semiconductor Nanostructures: Physics and Applications*, Edited by J. Shah, pp. 17-51, 1992.

[65] T. Ando, "Screening effect and quantum transport in a silicon inversion layer in strong magnetic fields," *J. Phys. Soc. Japan*, vol. 43, pp. 1616-1626, 1977.

[66] Y. C. Cheng, "Electron Mobility in an MOS Inversion Layer," in *Proc. 3rd Conf. Solid State Devices*, pp. 173-180, 1971.

[67] K. Masaki, K. Taniguchi, C. Hamaguchi, and M. Iwase, "Temperature Dependence of Electron Mobility in Si Inversion Layers," *Japanese J. Appl. Phys.*, vol. 30, no. 11A, pp. 2734-2739, 1991.

[68] Y. Matsumoto and Y. Uemura, "Scattering Mechanism and Low Temperature Mobility of MOS Inversion Layers," *Japan J. Appl. Phys.*, vol. 13, Supp. 2, Part 2, pp. 367-370, 1974.

[69] Y. C. Cheng and E. A. Sullivan, "On the role of scattering by surface roughness in silicon inversion layers," *Surface Science*, vol. 34, pp. 717-731, 1973.

[70] L. I. Schiff, *Quantum Mechanics*, McGraw-Hill, New York, 1955.

[71] J. R. Meyer and F. J. Bartoli, "Phase-shift calculation of ionized impurity scattering in semiconductors," *Phys. Rev. B*, vol. 23, no. 10, pp. 5413-5427, 1981.

[72] D. K. Ferry, "Effects of Surface Roughness in Inversion layer transport," in *IEDM Tech. Dig*., pp. 605-608, 1984.

[73] A. C. Smith, J. F. Janak, and R. B. Adler, *Electronic conduction in solids*, McGraw-Hill, New York, 1967.

[74] Donald P. Monroe, AT&T Bell Laboratories, *Private Communication*.

[75] C. G. Sodini, T. W. Ekstedt, and J. L. Moll, "Charge accumulation and mobility in thin dielectric MOS transisitors," *Sol.-State Elec.*, vol. 25, pp. 833-841, 1982.

[76] S. Takagi, M. Iwase, and A. Toriumi, in *Extended Abstracts of the 22nd. Conf. Sol. State Dev. Mat.*, pp. 275-278, 1990.

[77] J. T. Watt and J. D. Plummer, "Universal mobility-field curves electrons and holes in MOS inversion layers," in *Symp. VLSI Technology Dig. Tech. Papers*, pp. 81-82, 1987.

[78] C. L. Huang and G. Sh. Gildenblat, "Measurement and Modeling of the n-Channel MOSFET Inversion Layer Mobility and Device Characteristics in the Temperature Range 60-300K," I*EEE Trans. Elec. Dev.*, vol. ED-37, pp. 1289-1300, 1990.

[79] N. D. Arora and G. Sh. Gildenblat, "A semi-empirical model of the MOSFET inversion layer mobility for low-temperature operation," *IEEE Trans. Elec. Dev.*, vol. ED-34, no. 1, pp. 89-93, 1987.

[80] H. Shin, G. M. Yeric, A. F. Tasch, and C. M. Maziar, "Physically-based models for effective mobility and local-field mobility of electrons in MOS Inversion layers," *Solid-State Elec*., vol. 34, no. 6, pp. 545-552, 1991.

[81] K. Masaki, C. Hamaguchi, K. Taniguchi, and M. Iwase, "Electron mobility in Si

inversion layers," *Jap. J. of Appl. Phys.*, vol. 28, no. 10, pp. 1856-1863, 1989.

[82] M. Shirahata, H. Kusano, N. Kotani, S. Kusanoki, and Y. Akasaka, "A mobility model including the screening effect in MOS inversion layer," *IEEE Tran. CAD*, vol. 11, no. 9, pp. 1114-1118, 1992.

[83] C. Kittel and H. Kroemer, *Thermal Physics*, 2nd Edition, Freeman, New York, 1980.

[84] K. Shimohigashi and K. Seki, "Low-voltage ULSI design," *J. Solid-State Circuits*, vol. 28, no. 4, pp. 408-413, 1993.

[85] H. Haug and S. W. Koch, *Quantum Theory of the Optical and Electronic properties of semiconductors*, 2nd Edition, World Scientific, Singapore, 1990.

[86] N. Iwamoto, "Static local-field corrections of two-dimensional electron liquids," *Phys. Rev. B*, vol. 43, no. 3, pp. 2174-2182, 1991.

[87] C. Kittel, *Introduction to Solid State Physics*, 6th Edition, Wiley, New York, 1986.

[88] G. Y. Hu and R. F. O'Connell, "Polarisability of a two-dimensional electron gas including fluctuation effects," *J. Phys. C: Solid State Phys.*, vol. 21, pp. 4325-4331, 1988.

[89] F. F. Fang, A. B. Fowler, and A. Harstein, "Effective mass and collision time of (100) Si surface electrons," *Phys. Rev.*, B 16, pp. 4446-4454, 1977.

[90] F. F. Fang, "2DEG in strained Si/SiGe heterostructures," *Surf. Sci.*, vol. 305, pp. 301-306, 1994.

[91] C. -L. Huang, J. V. Faricelli, and N. D. Arora, "A new technique for measuring MOSFET inversion layer mobility," *IEEE Trans. Elec. Dev.*, vol. 40, no. 6, pp. 1134-1139, 1993.

[92] C. -L. Huang and N. D. Arora, "Characterization and modeling of the n- and p-channel MOSFETs inversion-layer mobility in the range 25-125°C," *Solid-State Electronics*, vol. 37, no. 1, pp. 97-103, 1994.

[93] R. S. Muller and T. I. Kamins, *Device Electronics for Integrated Circuits*, 2nd. Edition, Wiley, New York, 1986.

[94] J. Koomen, "Investigation of the MOST channel conductance in weak inversion" *Solid-State Electronics*, vol. 16, pp. 801-809, 1973.

[95] P. M. D. Chow and K. L. Wang, “A new ac technique for accurate determination of channel charge and mobility in very thin gate MOSFETs,” *IEEE Trans. Elec. Dev.*, vol. 33, pp. 1299-1304, 1986.

[96] S. Takagi, Toshiba Corp., *Private Communication*.

[97] S. Malhi and P. Chatterjee, “1-V microsystems-scaling on schedule for personal communications,” *IEEE Circuits and Devices*, pp. 13-17, 1994.

[98] T. H. Ning and C. T. Sah, “Theory of scattering of electrons in a nondegenerate-semiconductor-surface inversion layer by surface oxide charges,” *Phys. Rev. B*, vol. 6, no. 12, pp. 4605-4613, 1972.

[99] F. Gamiz, J. A. Lopez-Villanueva, J. A. Jimenez-Tejada, I. Melchor, A. Palma, “A comprehensive model for Coulomb scattering in inversion layers,” *J. Appl. Phys.*, vol. 75, no. 2, pp. 924-934, 1994.

[100] A. Gold, “Electronic transport properties of a two-dimensional electron gas in a silicon quantum-well structure at low temperature,” *Phys. Rev. B*, vol. 35, no. 2, pp. 723-733, 1987.

[101] J. Lee, H. N. Spector, and V. K. Arora, “Impurity scattering limited mobility in a quantum well heterojunction,” *J. Appl. Phys.*, vol. 54, no. 2, pp. 6995-7004, 1983.

[102] D. Monroe, Y. H. Xie, E. A. Fitzgerald, P. J. Silverman, G. P. Watson, “Comparison of mobility-limiting mechanisms in high-mobiliy $Si_{1-x}Ge_x$ heterostructures,” *J. Vac. Sci. Technol. B*, vol. 11, no. 4, pp. 1731-1737, 1993.

[103] K. Hess, “Impurity and phonon scattering in layered structures,” *Appl. Phys. Lett.*, vol. 35, no. 7, pp. 484-486, 1979.

[104] A. Gold, “Scattering time and single-particle relaxation time in a disordered two-dimensional electron gas,” *Phys. Rev. B*, vol. 38, no. 15, pp. 10798-10811, 1988.

[105] D. Pines, *Elementary excitations in solids*, Benjamin, New York, 1963.

[106] M. V. Fischetti and S. E. Laux, “Monte Carlo study of electron transport in silicon inversion layers,” *Phys. Rev. B*, vol. 48, no. 4, pp. 2244-2274, 1993.

[107] J. A. Lopez-Villanueva, I. Melchor, F. Gamiz, J. Banqueri, J. A. Jimenez-Tejada, “A model for the quantized accumulation layer in metal-insulator-semiconductor structures,” *Solid-State Electronics*, vol. 38, no. 1, pp. 203-210, 1995.

[108] Conor Rafferty, AT&T Bell Laboratories, *Private Communication*.

[109] E. H. Nicollian and J. R. Brews, *MOS (Metal Oxide Semiconductor) Physics and Technology*, Wiley, New York, 1982.

[110] M. J. van Dort, P. H. Woerlee, A. J. Walker, C. A. H. Juffermans, and H. Lifka, "Influence of high substrate doping levels on the threshold voltage and the mobility of deep-submicrometer MOSFET's," *IEEE Trans. Elec. Dev.*, vol. 39, no. 4, pp. 932-937, 1992.

[111] D. Boulin, AT&T Bell Laboratories, *Private Communication*.

[112] S. Biesemans and K. D. Meyer, "Analytical calculation of the subthreshold slope increase in short channel MOSFET's by taking the drift component into account," in *Proc. Solid State Dev. Mat.*, pp. 892-894, 1994.

[113] K. K. Ng and J. R. Brews, "Measuring the effective channel length of MOSFETs," *IEEE Circuits and Devices Mag.*, vol. 6, no. 6, pp. 33-38, Nov. 1990.

[114] H.-H Vuong, C. S. Rafferty, M. J. McLennan, and J. Lentz, "Industrial perspective based on PROPHET," in *CAD for ICs — Process, Device, and Circuits*, Stanford University, Stanford, Calif., August 1994.

[115] S. J. Proctor, L. W. Linholm, and J. A. Mazer, "Direct measurement of interfacial contact resistance, end contact resistance, and interfacial contact layer uniformity," *IEEE Trans. Elec. Dev.*, vol. 30, pp. 1535-1542, 1983.

[116] C. Y. Lu, J. M. Sung, H. C. Kirsch, S. J. Hillenius, T. E. Smith, and L. Manchanda, "Anamolous C-V characteristics of implanted poly MOS structure in n^+/p^+ dual-gate CMOS technology," *IEEE Elec. Dev. Lett.*, vol. 10, no. 5, pp. 192-194, 1989.

[117] M. R. Pinto, J. Bude, and C. S. Rafferty, "Simulation of ULSI silicon MOSFETs," in *Proc. VPAD*, pp. 22-25, 1993.

[118] Y. Ohkura, "Quantum effects in Si n-MOS inversion layer at high substrate concentration," *Solid-State Elec.*, vol. 33, no. 12, pp. 1581-1585, 1990.

[119] C. -Y. Hu, D. L. Kencke, S. Banerjee, B. Bandyopadhyay, E. Ibok, and S. Garg, "Determining effective dielectric thicknesses of metal-oxide-semiconductor structures in accumulation mode," *Appl. Phys. Lett.*, vol. 66, no. 13, pp. 1638-40, 1995.